COSMIC RAY DETECTION BY ATMOSPHERIC FLUORESCENCE

A Thesis

Presented to the Faculty of the Graduate School

of Cornell University for the Degree of

Doctor of Philosophy

by

Alan Newton Bunner

February, 1967

BIOGRAPHICAL SKETCH

Alan Newton Bunner was born on January 11, 1938 in St. Catherines, Ontario. He majored in Mathematics, Physics and Astronomy at the University of Toronto, graduating with the Bachelor of Arts degree in June, 1960. He entered the graduate school of Cornell University in September, 1960 and was employed as a Teaching Assistant and as a Research Assistant. He married Miss Diane Bishop in June, 1963. He earned the degree of Master of Science at Cornell University in June, 1964 for experimental work on the fluorescent efficiency of air. He is currently on the Cornell University staff as an Instructor of Physics and a Research Associate in the Cosmic Ray Group.

ACKNOWLEDGMENTS

I wish to thank Professor Kenneth Greisen for the encouragement and patient assistance he has offered throughout the experimental project described here, and for his thoughtful criticism of the manuscript of this thesis.

I deeply appreciate the co-operation of Mr. Edward Jenkins, who has contributed significantly to this work. Our many stimulating discussions have been a pleasure. The reader may find many important aspects of this project discussed in Mr. Jenkins' thesis, which constitutes in a sense a companion volume to this report.

I am indebted to Professor Goro Tanahashi of Tokyo University and Professor Seinosuke Ozaki of Osaka University for their invaluable participation in this program.

The U.S. Atomic Energy Commission has fully and generously supported this research from its inception. Research facilities were provided by the Laboratory of Nuclear Studies at Cornell University.

COSMIC RAY DETECTION BY ATMOSPHERIC FLUORESCENCE

Table of Contents

Table of Contents (Continued)

Chapter 1

INTRODUCTION

Cosmic ray particles play an important role in the energetics of the galaxy, involving an energy density of about 1 ev/cm^3 (3), comparable to the energy density of galactic magnetic fields and of galactic turbulent gas motion, and greater than or comparable to the total energy density of electromagnetic radiation, including starlight (10, 11).

There is considerable interest in the study of primary cosmic rays of very high energy, i.e., energies above about 10^{15} electron volts, in order to throw light on a number of basic physical questions, such as:

(a) the origin and acceleration mechanisms of cosmic ray particles,

(b) the propagation of cosmic rays in galaxies,

(c) the elementary interactions of very high energy particles.

The observable properties of the cosmic ray flux that are of interest in solving these problems are the charge spectrum (or composition) of the particles and the energy spectrum of the different components; the distribution of the directions of arrival in galactic co-ordinates; and the maximum particle energy, if any.

It is important to extend these studies to the highest energies possible in order to reveal most clearly the nature of the processes at work. For this reason new techniques must be evolved which are able to detect and extract information

from these extremely rare events. The purpose of this thesis is to discuss the technique of using the atmosphere as a scintillator for the study of these high energy particles, a method suggested several years ago by Greisen and others.

Survey of Cosmic Ray Studies -

Above about 10^{13} ev, because of the rarity of events, cosmic rays are studied almost solely by their interaction in the earth's atmosphere, where a cascade of secondary particles is generated by radiation and pair production processes, following a few major nuclear interactions. (The mean free path for nuclear interaction of a very high energy proton in air is about 80 gms/cm^2 (1) as compared with the vertical thickness of the atmosphere of 1000 gms/cm^2.)

Thus our present knowledge of cosmic rays above 10^{13} ev stems from analysis of these "extensive air showers". Good reviews of the information now available concerning the composition, spectra and directional asymmetry of primary cosmic rays can be found in references 2 through 9. To sum up very briefly, the integral energy spectrum on the next page shows the observed rate of arrival of primaries of energy above E electron volts plotted against log E, as summarized by Greisen at the 1965 Cosmic Ray Conference (24). This spectrum sums over protons, neutrons, heavier nuclei and gamma rays since air shower studies do not in general reveal the nature of the incident particle, the development of the shower being

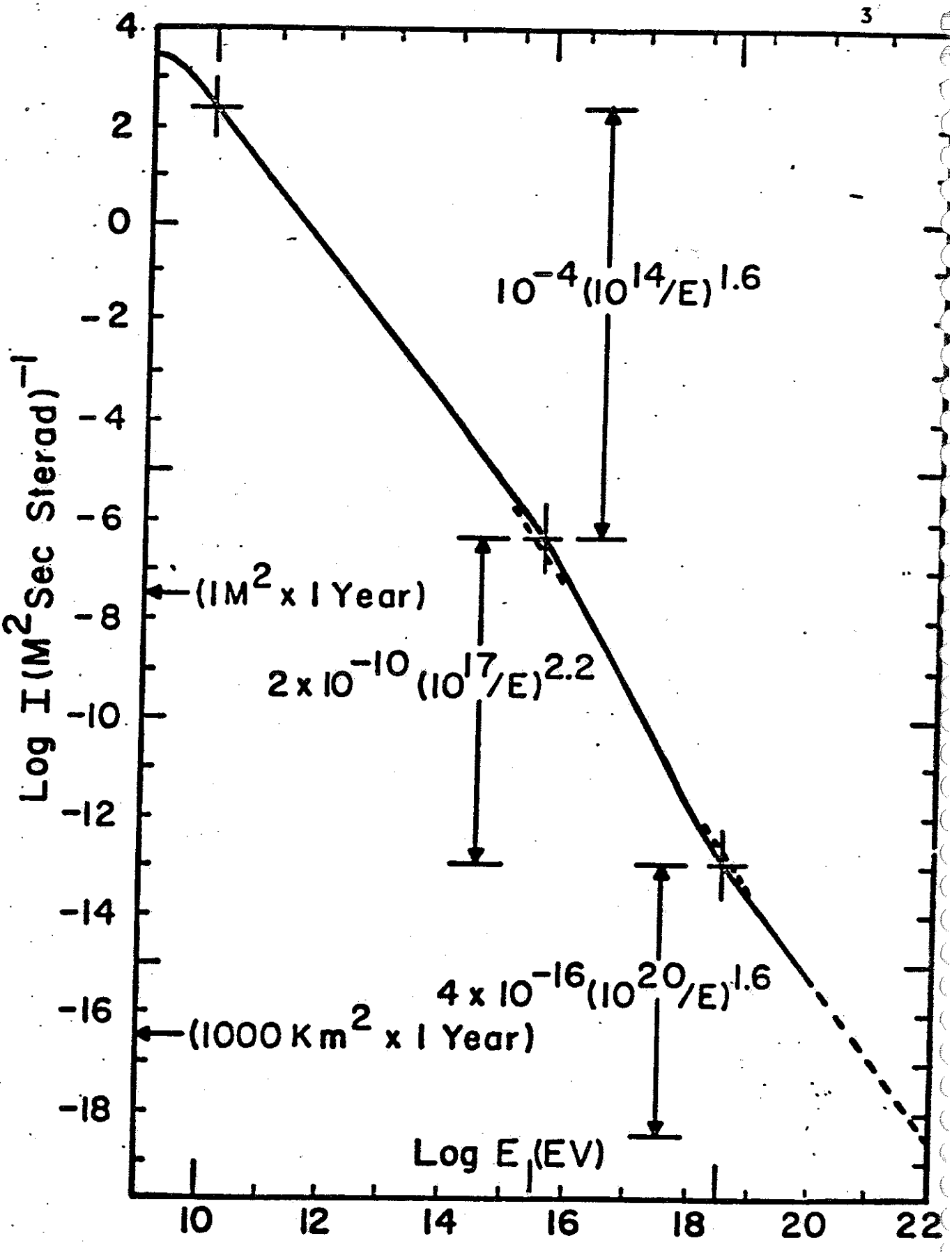

Figure 1.1 Approximate Integral Energy Spectrum of Primary Cosmic Rays

dominated by electromagnetic processes involving thousands of secondary particles spread over a relatively wide area.

The increase of the slope of the integral spectrum in the vicinity of 10^{15} ev is now quite well established (8, 12, 96, 97). Although the statistical accuracy of the experimental points in the region 10^{15} ev to 10^{18} ev is not excellent, the slope can be measured accurately even without knowing the absolute rates.

However, the reduced exponent above 10^{18} ev is not well substantiated; it represents only the fact that in experiments at Cornell and at Volcano Ranch, in a region where 2 or 3 events were expected on the basis of the 2.2 slope, about 9 were recorded (9).

Emulsion measurements for particles of several Gev per nucleon have shown that primaries having a given velocity (or energy per nucleon) consist of about 93% protons, 6.3% alphas, and 0.7% heavier nuclei (3).

Furthermore, there is strong evidence that the spectra of these components are very parallel up to at least 10^{13} ev/nucleon (9,12,98,99,100). In the regime of extensive air showers the observed energy spectrum of the primaries relates to the total energy of the particles causing the showers rather than to the energy per nucleon. By this measure, cosmic rays are less than half protons, as shown in the table on the next page (3,16). Clearly, a satisfactory theory for the origin and motion of cosmic rays must explain this unusual charge distribution, as well as the presence of anomalous isotopic ratios,

Table 1.1

Cosmic Ray Composition

	With a Given Energy/Nucleon	With a Given Total Energy
Protons	93 %	49 %
Alphas	6.3	26
Li, Be, B	0.14	2
C, N, O, F	0.42	11
$Z \geq 10$	0.14	12
$Z \geq 20$	0.04	7
γ-rays	0.1	0.1

such as the observed high relative abundance of He^3 nuclei (6,8). This observation has been interpreted as the result of fragmentation of heavier nuclei in nuclear interactions in the interstellar medium. Calculation then indicates that these cosmic rays have passed through from 2 to 10 gm/cm^2 of material, which corresponds to many galactic rotations, if these particles are contained in the galaxy. The chemical composition (Table 1.1) indicates either that the sources of cosmic rays are anomalously rich in heavy nuclei or, more probably, that the acceleration of heavy nuclei is more efficient than that of protons and alpha particles.

It has been suggested that the question of the composition of the cosmic ray flux at very high energies may be linked with the observed changes in the slope of the spectrum through the following explanation (3,13,108). If the galaxy is only able to contain particles up to a rigidity of 10^{15} - 10^{16} ev/c, then protons should disappear from the galactic component of the cosmic ray flux above 10^{16} ev and higher-Z primaries at proportionately higher energies. Therefore between 10^{16} and $3x10^{17}$ ev the spectrum may be expected to reflect only the flux of heavy primaries in our galaxy. Above 10^{18} ev, however, the flux of galactic cosmic rays falls so low that the extra-galactic cosmic rays dominate. These particles have travelled much longer paths than galactic cosmic rays and may be assumed to have undergone considerable fragmentation by nuclear interaction and photodisintegration. Hence, only protons may remain in the cosmic ray flux above 10^{18} ev, if the acceleration and

loss mechanisms of extragalactic cosmic rays are similar to those within our galaxy. However, alternate explanations of the changes in spectral slope have been offered, and the answer is not yet well-established.

With regard to the asymmetry of arrival of cosmic rays, particles of the highest energy have the largest radius of curvature in the galactic magnetic field, and hence are expected to reflect best the direction of their source region. At present, although there are indications of a preference for trajectories lying in the galactic plane (7,8), the isotropy is good to within 0.1% at 10^{14} ev, to within 1% at 10^{16} ev, and to within 3% at 10^{17} ev (2,3).

The highest energy so far observed is about 10^{20} ev in a particle that may have been a proton (13,17). Using

$$\text{Cyclotron radius} = 3.5\times10^{-21}\ \frac{E(\text{ev})}{Z\ B\ (\text{gauss})}\ \text{light years}, \quad (1.1)$$

and accepting a field strength of 10^{-5} gauss (10), which represents an upper limit for our galaxy, we arrive at a radius of curvature of at least 3×10^{4} light years, and a diameter of at least 6×10^{4} light years, which is about 60 times the thickness of the galactic disc. It is difficult to find a mechanism for containing particles efficiently over such a vast distance, since such containment implies a coherent magnetic field over distances greater than the cyclotron diameter.

Cosmic Ray Astrophysics -

To understand the importance of extending our present knowledge of the high energy cosmic ray spectrum we must inquire briefly into current theories for the acceleration and loss mechanisms of these particles.

Most theories for the origin of cosmic rays make use of an electromagnetic acceleration mechanism and a magnetic field which varies either in time or in space. The presence of a magnetic field B causes a particle to be deflected with a radius of curvature given by

$$\rho = \frac{p(ev/c)}{300\ Z\ B(gauss)} \quad cm. \qquad (1.2)$$

where p is the momentum of the particle, and Z is the particle's charge. If the acceleration is slow, requiring very many orbits or magnetic reflections of the particles to build up the energy by a substantial factor, the fields must be able to contain the particles for very many orbits despite the drifts caused by the pitch angles and field gradients. Then the dimension R of the field-containing region must exceed the cyclotron diameter ρ by at least, let us say, a factor of 30. Therefore

$$R > 30\ \frac{E(ev)}{300\ Z\ B(gauss)} \quad cm. \qquad (1.3)$$

Furthermore, the source size must be large enough to avoid losses which deplete the flux of high energy particles more rapidly than they are accelerated. For very high energy protons, synchrotron radiation becomes an important energy

drain (24), amounting to a relative loss of

$$\frac{\Delta E}{E} = \frac{2}{3} \frac{e \beta^2}{(Mc^2)^4} Z E^2 B \qquad (\text{radian})^{-1} \qquad (1.4)$$

(where M = proton mass), which must be very small compared to one. For protons of 10^{20} ev, this implies $B \ll 0.1$ gauss.

Combining this restriction on the magnetic field strength with (1.3), the source size is restricted by

$$R \gg 2 \times 10^{-40} E^3 \text{ cm} \qquad (1.5)$$

or

$$R \gg 2 \times 10^{-13} \gamma^3 \text{ cm}, \qquad (1.6)$$

$$\text{for protons, where } \gamma = E/Mc^2. \qquad (1.7)$$

Therefore for protons of energy $E = 10^{19}$ ev, $\gamma = 10^{10}$ and R must be $\gg 2 \times 10^{17}$ cm = 0.2 light year, and for $E = 10^{20}$ ev, $R \gg 2 \times 10^{20}$ cm = 200 light years.

Therefore to allow the acceleration of particles to very high energies without severe losses requires a source region of very large volume and consequent large total magnetic energy. Writing the total magnetic energy as

$$W_m = \frac{4}{3} \pi R^3 \left(\frac{B^2}{8\pi} \right) , \qquad (1.8)$$

from (1.3),

$$W_m \gg 3 \times 10^{-4} \frac{E^3 \text{ (ev)}}{Z^3 B(\text{gauss})} \text{ ergs} \qquad (1.9)$$

and therefore from (1.4),

$$W_m \gg 6 \times 10^{-44} \frac{E^5 \text{ (ev)}}{Z^2} \text{ ergs}, \qquad (1.10)$$

or

$$W_m \gg 50 \ \gamma^5 \text{ ergs}. \qquad (1.11)$$

Therefore, for example, a source region having a total magnetic energy much greater than 5×10^{56} ergs is required for the production of 10^{20} ev protons. This is comparable with the estimated magnetic energy content of galactic nuclei or quasars (3,24).

The presence of a substantial fraction of heavy nuclei in the cosmic ray flux up to an energy of 10^{12} ev implies that the acceleration process be collisionless and gradual (3). One mechanism that has been advanced in various forms is that of statistical acceleration of particles by repeated scattering off moving magnetic field inhomogeneities ("Fermi mechanism") (3,4,5,101). For particles to receive a net energy gain by this process, it is necessary that they be injected with energies on the order of 1 Gev (4). This injection might be provided by supernovae (3,18,19,20), either with the acceleration to high energies taking place at the shock front of the expanding supernova envelope (20), or with the supernova injecting into a large-scale interstellar Fermi mechanism (3,4). Supernovae occur in our galaxy every 50 to 200 years (3), with perhaps 0.1% of a typical 10^{52} ergs energy release going into high energy particles. In this case one expects a high proportion of heavy elements (from the interior of the highly evolved star) up to iron, and cosmic abundance above iron (20). One can also make predictions about certain isotopic ratios injected (21).

The Fermi acceleration mechanism predicts a power law energy spectrum of the form (3,5,11,22)

$$I\ (>E) \;=\; (\text{constant}) \times E^{-\frac{1}{\alpha T}} \qquad (1.12)$$

where α is the relative rate of increase of energy

$$\frac{dE}{dt} = \alpha E \;, \quad E = E_o \; e^{\alpha t} \qquad (1.13)$$

and T is the mean life of a particle in the region where the acceleration is active

$$\frac{1}{T} = \frac{1}{T_{\text{diffusion}}} + \frac{1}{T_{\substack{\text{nuclear} \\ \text{interaction}}}} + (\text{terms for other losses}). \qquad (1.14)$$

The coefficient α is given by (3)

$$\alpha = \frac{V^2}{c^2 \tau} \qquad (1.15)$$

where V = average velocity of the magnetic clouds,

τ = mean travel time between clouds.

If the mean lifetime T is dominated by diffusive leakage out of the accelerating region, then T will be independent of charge Z, for particles of a given rigidity. If the rate of acceleration α is also independent of Z then the energy spectrum will have the same slope for all constituents.

However, the Fermi model is basically an inefficient acceleration mechanism, requiring many repeated scatterings to achieve very high energies. Statistical acceleration can hardly occur in interstellar space because the vast distances involved lead to time constants for acceleration on the order of 10^{18} seconds (101). Furthermore, the arguments advanced earlier concerning the size and energy content of the source regions restrict the maximum particle energy attainable by

this process. The spectral index of the integral cosmic ray spectrum in the energy range 10^{12} to 10^{15} ev has a value of

$$\frac{1}{\alpha T} = \frac{c^2}{V^2 T} \approx 1.5 \qquad (1.16)$$

which requires the mean life against loss, $T \gg \tau$, the mean time between scatterings, unless $V \approx c$. This condition may still be met in the expanding envelopes of supernovae (3,101) or the region near the galactic center, where higher velocity, relatively small-scale motion may produce more rapid acceleration (3). In these cases we might expect a power-law spectrum up to some energy depending on the source size, followed by a fairly fast cut-off due to rapid leakage loss from the source region. The interstellar galactic fields would then serve to diffuse the accelerated particles throughout the galaxy leading to an isotropic flux up to, say, 10^{16} ev/nucleon.

In summary, localized galactic sources may contribute the main part of the observed cosmic ray spectrum up to the energy at which leakage into intergalactic space becomes rapid, beyond which only extragalactic and metagalactic cosmic rays remain, arising for example from quasars or other extragalactic radio sources, where the existence of synchrotron emission signals the presence of an abundance of high energy particles.

It is of interest to consider some predictions applying to the very high energy primaries. For cosmic ray nuclei above 10^{16} ev ordinary starlight photons can produce photodisintegration with a fairly high cross section. At higher energies,

infrared photons and radio waves can produce the same break-up of heavy primaries (3,24). This effect could be important for very high energy primaries passing near the Sun, and leads to the possibility of detecting correlated extensive air showers a few hundred kilometers apart on Earth (3,25). Also, photo-disintegration of heavy nuclei could produce very high energy neutrons, which are undeflected by galactic magnetic fields (24). A neutron of 10^{16} ev could travel 400 light years before decay, and a 10^{20} ev neutron could reach us from as far as 2×10^{7} light years. Thus, for example, a neutron would have to have 10^{17} ev energy to reach us from the Crab Nebula. The possibility exists of observing some anisotropy of very high energy particles by this effect. Also, if photodisintegration affects the majority of very high energy primaries before reaching the earth, this could explain Linsley's observation of muon ratios which indicated that primaries above 10^{17} ev are most probably all single nucleons (13).

Greisen (24) has pointed out that the structure of very high energy air showers may be affected, since the decay of the π^{o}-mesons is inhibited above 10^{19} ev, thus delaying the growth of the electromagnetic component of the showers.

If we accept the hypothesis that cosmic rays of energy 10^{18} ev and greater may have travelled over intergalactic distances, it is important to calculate the effect of various loss mechanisms on these particles.

The mean free path for nuclear interaction between protons is approximately 50 gm/cm^{2}, which imposes a restriction

again on the source region, namely that

$$n \, m \, R \ll 50 \text{ gm/cm}^2 \tag{1.17}$$

where n = gas density in source region in protons/cm^3

m = proton mass in gm,

R = radius of source region in cm.

Writing this condition in terms of the mass M of the source region,

$$M = \frac{4}{3} \pi \, n \, m \, R^3 , \tag{1.18}$$

and therefore

$$R \gg \left(\frac{3}{4\pi} \frac{M}{50} \right)^{1/2} \text{ cm}, \tag{1.19}$$

implying, for example, that $R \gg 10^3$ light years for a gaseous mass equal to the total mass of our galaxy. The probability of an additional interaction in interstellar or intergalactic space is small, since the maximum thickness of the galaxy is less than 0.1 gm/cm^2 and even the thickness of the observable universe is only about 0.2 gm/cm^2 (10).

The probabilities for nuclear interaction are somewhat greater for heavy nuclei, but a much more rapid loss occurs for primaries above 5×10^{18} ev/nucleon in the previously mentioned photodisintegration. The threshold for this reaction is on the order of 10 Mev for most nuclei in the frame of reference of the nucleus, and the cross section rises rapidly to about 10^{-25} cm^2 (49). This reaction will then occur with the recently discovered thermal microwave radiation (102), which is assumed to pervade all space uniformly, provided the particle energies are above 5×10^{18} ev/nucleon, with a mean free

path of only about 10^{22} cm = 10^4 light years.

The thermal microwave radiation also imposes an upper limit on the expected spectrum of cosmic ray protons, through the action of pion photoproduction (103), which has a threshold near 10^{20} ev and a cross section which quickly rises to about 4×10^{-28} cm^2:

$$\left.\begin{aligned} \gamma + p &\rightarrow \pi^o + p \\ &\quad\ \pi^+ + n \end{aligned}\right\} \qquad (1.20)$$

Accepting an average cross section of 2×10^{-28} cm^2 and a photon density of 600 photons/cm^3, the consequence of these reactions is a mean free path of about 10^{25} cm = 10^7 light years, which is approximately the diameter of the "Local Group" of galaxies. Only if the high energy protons are generated well within this radius will they avoid this effect for energies above 10^{20} ev.

A less strong loss of energy for very high energy protons arises from the momentum transfer when a microwave photon undergoes pair production in the field of a proton (103):

$$\gamma + p \rightarrow e^+ + e^- + p \qquad (1.21)$$

This reaction has a threshold at a proton energy of about 7×10^{17} ev with a cross section of about 2×10^{-27} cm^2 (103). Greisen has shown (103) that the fractional energy loss to the proton in this reaction is approximately

$$\frac{10^{-3}\, E_{thresh}}{E} ,$$

where $E_{thresh} = 7\times10^{17}$ ev. This has the effect of reducing

the primary spectrum by a small factor in the energy range 10^{18} to 10^{20} ev.

Finally, an effect has been predicted (104,105) which severely limits the spectrum of very high energy primary gamma rays due to pair production in photon-photon collisions:

$$\gamma + \gamma \rightarrow e^+ + e^- \qquad (1.22)$$

For thermal photons of energy about 7×10^{-4} ev, this reaction has a rapidly rising cross section for gamma rays near 10^{14} ev and reaches a maximum average cross section of about 10^{-25} cm^2. The mean free path for this catastrophic loss of high energy gamma rays reaches a minimum of 10^{22} cm = 10^4 light years, at a gamma energy of 10^{15} ev.

The discovery of this low energy black-body spectrum, which is interpreted as a red-shifted remnant of the primeval fireball, thus has important implications for cosmic ray astrophysics, and provides incentive for a search for the upper limit to the primary proton spectrum. An observational study of this upper limit not only can provide additional confirmation of an evolutionary cosmology, but may yield an estimate of distance to the sources of very high energy cosmic rays.

Chapter 2
THE ATMOSPHERE AS A COSMIC RAY SCINTILLATOR

The passage of high energy particles through a gas results in the ionization and excitation of its molecules. The electronic excitation energy of the molecules is either dissipated non-radiatively by collisional or internal quenching processes* or it is emitted as visible or ultraviolet photons. This radiation is called fluorescence (or more technically exact, luminescence) or scintillation light. To estimate the quality of air as a scintillator it is necessary to find the efficiency of the fluorescence, that is, the fraction of the energy lost by ionization and excitation that goes into fluorescence photons.

In the case of cosmic ray showers, the ionization and excitation are produced by a sort of shock front of secondary particles, mostly electrons, which propagates down through the atmosphere at velocity $\approx$ c. Since the lateral distribution of these secondaries is on the order of tens of meters for a primary energy of 10^{16} ev (2) and the thickness of the shower front is even less, typically 2 or 3 meters, then when observed at distances of several kilometers, the shower can be considered

*By internal quenching we mean any process by which an isolated molecule can accomplish a downward electronic transition without radiation, such as transfer of electronic excitation energy to high vibrational levels of a lower electronic state, with subsequent emission of infrared radiation. See reference 26, pages 59, 72, 574.

as a small source of isotropic light moving through the atmosphere at velocity c.

The detection of cosmic ray showers by this process offers several advantages over conventional particle sampling techniques. The fluorescent intensity as a function of distance along the trajectory yields directly the longitudinal structure of the shower, about which little is known at present. Conventional detection methods observe only a cross section of the shower at ground level and may leave an ambiguity as to whether an observed secondary particle distribution represents a large air shower growing towards maximum or a smaller shower decaying. Similarly, a spectrum of shower sizes recorded with a ground-level detector may display a deceptive bend in the energy region corresponding to air showers which reach their maximum near ground level (97).

In the case of the air fluorescence detector, the total light output yields the total energy dissipated in the atmosphere and hence the primary energy without being subject to the fluctuations of a particle sampling determination, provided most of the energy has been dissipated before striking the earth. Most important, if the radius of visibility is limited only by Rayleigh scattering and is therefore roughly 20 km (at 4000 Å) then the effective area for detection can be as great as 6000 km^2 - steradians.

The primary limitation is the presence of a background of light from the night sky. A photoelectric detector viewing

this background produces a signal which is subject to statistical fluctuations. Since a pulse of light no longer than 100 microseconds (travel time through the atmosphere) is expected, the background consists of the fluctuations having this time scale or shorter. Included in the background will be occasional pulses of light from the Cerenkov radiation of small air showers (27) and possible contributions from man-made sources.

Therefore, this technique is restricted to clear, moonless nights free from atmospheric electrical disturbances and well removed from artificial light sources.

Longitudinal Shower Development -

High energy nucleon induced air showers consist of a "backbone" of nuclear interactions with an accompanying electromagnetic cascade of electrons, positrons and gamma rays. A number of authors have attempted to account statistically for the complexities of the nuclear cascade (6,8,9) but the cross sections for multiple pion generation, photoproduction, nucleon antinucleon creation, etc., are not well known at very high energies, and the relatively few high energy nuclear interactions comprising the shower "backbone" makes the end result subject to large fluctuations. However, a few "rules of thumb" have evolved: A usual assumption is that an air shower from a primary of A nucleon masses of energy E_o is equivalent to a superposition of A showers from primary nucleons each of

energy E_o/A. The nuclear interactions give rise to secondary nucleons, antinucleons, hyperons and mesons. The decay of K mesons and charged π mesons produces muons which lose their energy by ionization. The decay of π^o mesons produces gamma rays, each of which initiates an electromagnetic cascade, the theory of which is well known; see, for example, Rossi and Greisen (28). When the shower reaches its maximum in terms of number of secondary particles, electrons and positrons are by far the most numerous particles. After this "soft component" has been absorbed, mainly muons remain.

In order to predict the output of fluorescence light along the shower path, it is necessary to know the rate of energy loss by collisions as a function of distance along the path, and the fraction of the collision loss that goes into visible photons. Since the dominant contribution to the collision loss in a high energy shower comes from minimum ionizing particles, and since the majority of the particles in the main part of the shower are electrons and positrons, then it is a safe assumption that the rate of energy loss by collisions is simply proportional to the number of secondary particles in the shower.

The probability for a charged particle of kinetic energy E and velocity β traversing a thickness dx gm/cm^2 to transfer an energy between E' and E' + dE' to an atomic electron is given approximately by (1)

$$\phi_{col}(E,E')dE'dx \approx \frac{2C\,mc^2}{\beta^2}\,\frac{Z}{A}\,\frac{dE'}{E'^2}\,dx \qquad (2.1)$$

where m = electron rest mass

Z = charge number of the material traversed

A = mass number of the material traversed

C = 0.150

This formula treats the atomic electrons as free, and is valid when β substantially exceeds the velocities of the atomic electrons, provided $\varepsilon_j \ll E' \ll E_o$ where ε_j are the binding energies of the electrons and E_o is the primary energy of the ionizing particle. Under the above condition on β, it is also true that the ratio of ionization and excitation probabilities is independent of the nature and energy of the incident particle (provided it is singly charged).

To a first approximation, we can therefore assume that the rate of excitation is proportional to the number of secondary particles in the shower.

Rossi and Greisen (28) have calculated theoretically the number of secondary particles N of energy greater than E electron volts as a function of distance t for an electromagnetic shower of initial energy E_o under two approximations: (a) assuming energies large compared with the critical energy E_c* and neglecting collision losses and Compton effect, and (b) neglecting Compton effect and describing the collision

---

*E_c = the energy at which a particle would dissipate all its energy by collision loss in one radiation length, = 84.2 Mev for air.

loss as a constant energy dissipation. Their results are shown on pages 23 and 24. The distance t is measured in radiation lengths, where one radiation length is the length in which a fast electron loses all but 1/e of its energy by radiation; this length is equal to 37.1 gm/cm^2 in air (29).

Since, from the point of view of numbers of secondary electrons, a nucleon induced air shower can be considered as some sort of superposition of electromagnetic cascades, and since the nuclear interaction length in air is not very different from the radiation length, it is expected that true (nucleon induced) air showers will exhibit shower curves similar to those shown.

Theory of the Fluorescence Process -

Now it is of interest to determine the efficiency of the fluorescence process on particle bombardment. Many authors have studied this problem, both experimentally and theoretically (26,30,31,32,33). It has been shown experimentally (30,32,34) that, down to very low pressures, the fluorescence radiation from air results almost entirely from electronic transitions in the N_2 molecule and N_2^+ molecular ion. A schematic energy level diagram of the N_2 molecule including some levels of the N_2^+ ion is shown in page 25, where the electronic levels (heavy horizontal lines) are labelled according to standard spectroscopic notation (34,35) and the vibrational sub-levels of the electronic states are indicated

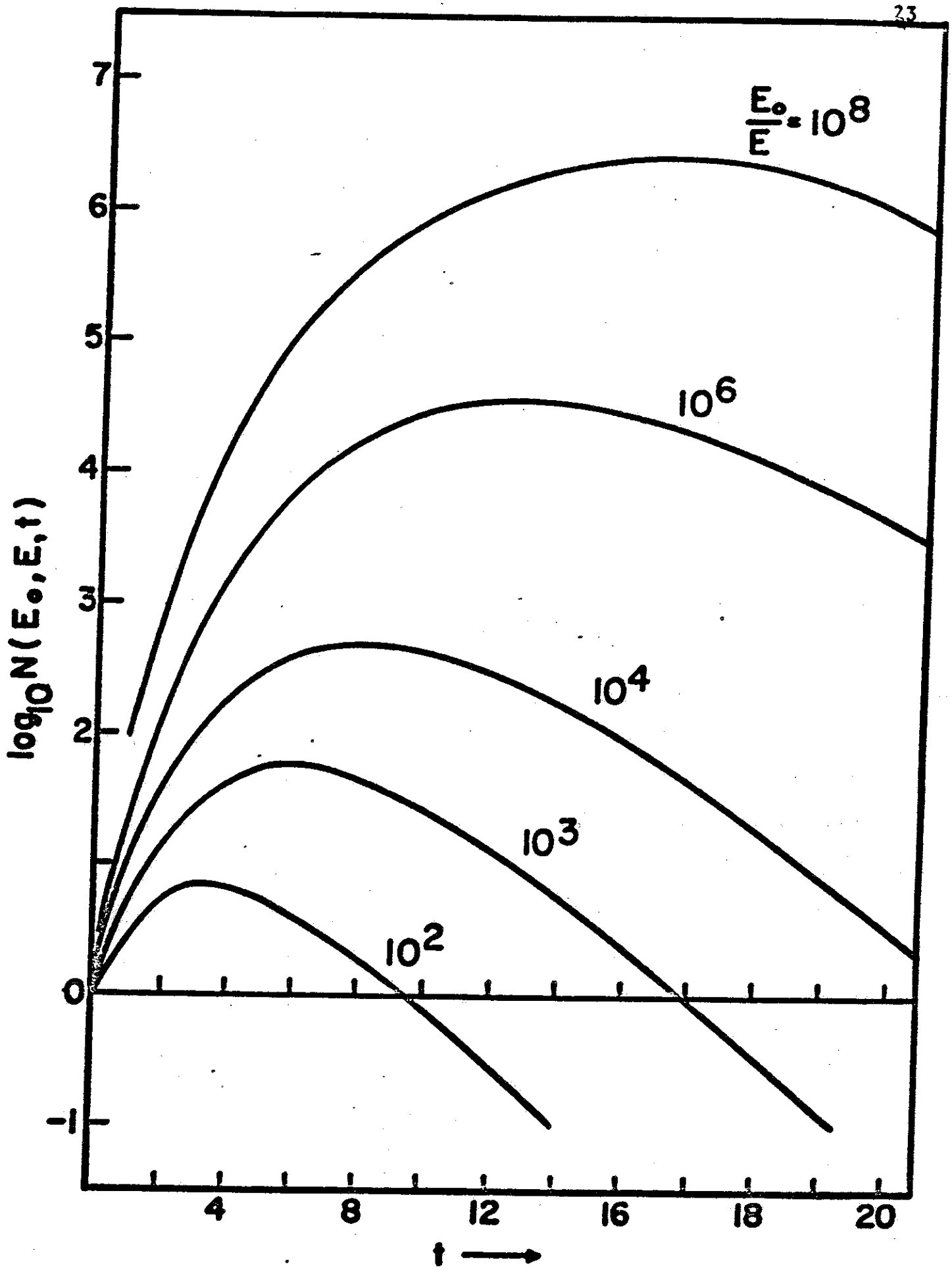
$\frac{E_o}{E} = 10^8$
10^6
10^4
10^3
10^2
$\log_{10} N(E_o, E, t)$
7
6
5
4
3
2
0
-1
4
8
12
16
18
20
t

Figure 2.1

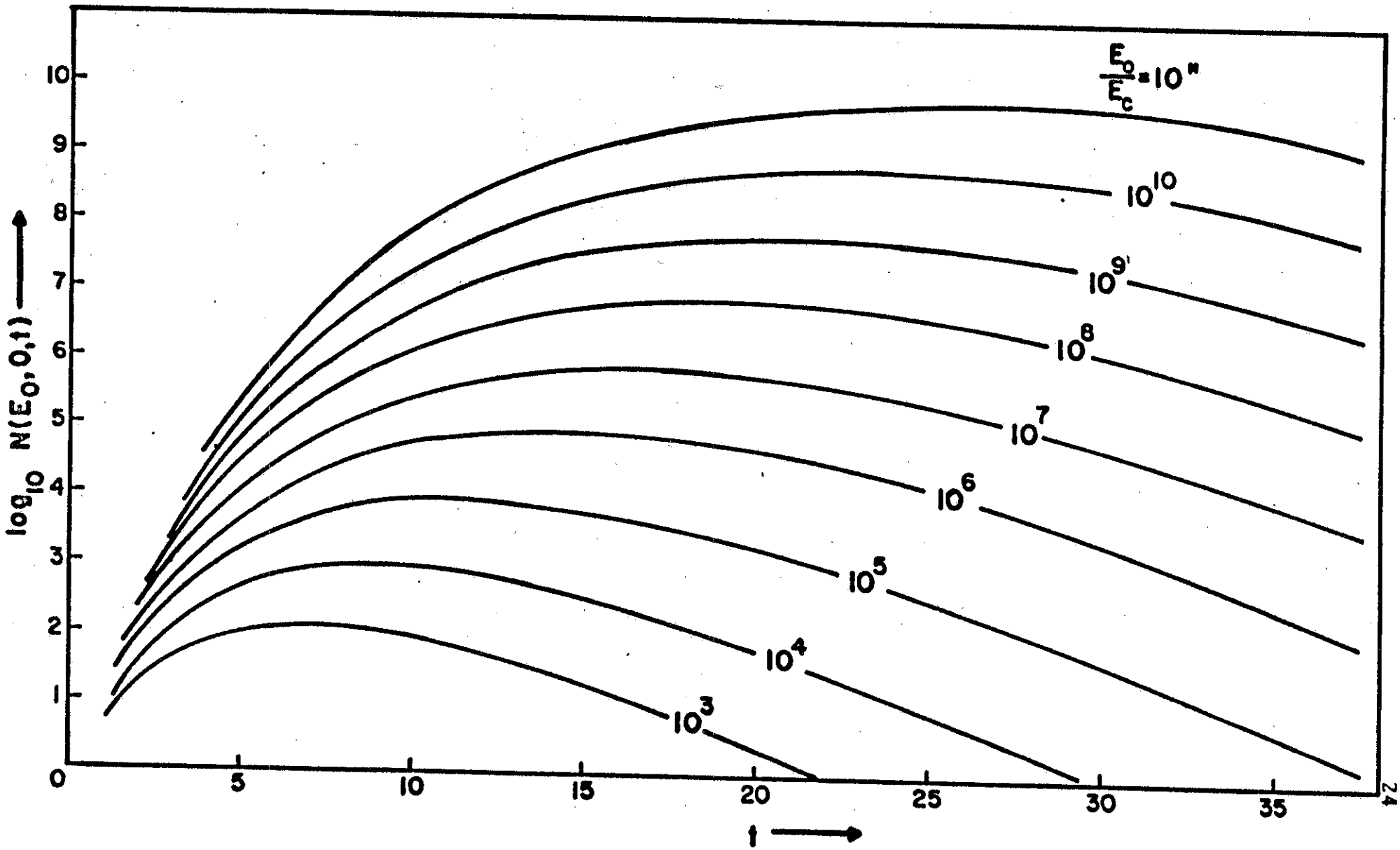
$\frac{E_0}{E_c} = 10^n$
10^{10}
10^9
10^8
10^7
10^6
10^5
10^4
10^3
$\log_{10} N(E_0, 0, t)$
t
0
5
10
15
20
25
30
35
24

Figure 2.2

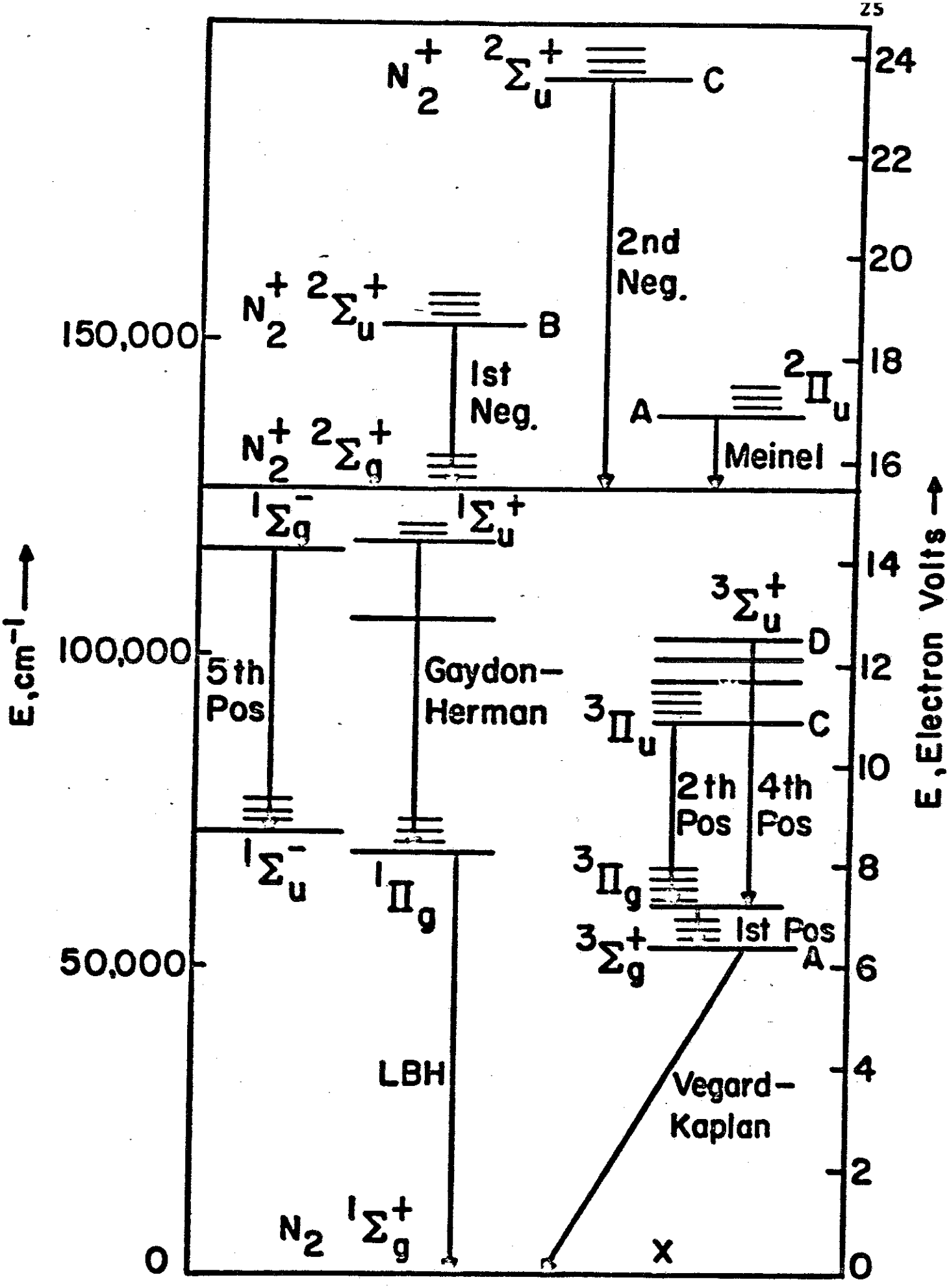
N_2^+ $^2\Sigma_u^+$
C
2nd Neg.
N_2^+ $^2\Sigma_u^+$
B
1st Neg.
N_2^+ $^2\Sigma_g^+$
$^2\Pi_u$
A
Meinel
$^1\Sigma_g^-$
$^1\Sigma_u^+$
$^3\Sigma_u^+$
D
5th Pos
Gaydon–Herman
$^3\Pi_u$
C
2th Pos
4th Pos
$^1\Sigma_u^-$
$^1\Pi_g$
$^3\Pi_g$
1st Pos
$^3\Sigma_g^+$
A
LBH
Vegard–Kaplan
N_2 $^1\Sigma_g^+$
X
150,000
100,000
50,000
0
E, cm^{-1}
E, Electron Volts
24
22
20
18
16
14
12
10
8
6
4
2
0

Figure 2.3

by the short lighter lines.

It has been found that for pressures down to at least 40 microns Hg, corresponding to altitutdes up to 60 km, the fluorescence spectrum consists almost entirely of the N_2 second positive (2P) system and the N_2^+ first negative (1N) system (36,37).

Let us consider the possible excitation mechanisms for these systems. The upper level of the N_2^+ 1N system can be excited by direct ionization with excitation by any high energy incident particle, for example

$$N_2 + e \longrightarrow N_2^{+*} + e + e \qquad (2.2)$$

On the other hand, the N_2 2P (and also N_2 1P) upper levels cannot be directly excited from the ground state by a high energy interaction because a change in the resultant electronic spin of the molecule is necessary which is forbidden (38,39). However, these levels can be excited by low velocity electron collisions involving electron exchange with a resultant spin change (37,38,40), or by cascading from higher levels, for example following recombination

i.e. $$N_2 + e(\uparrow) \longrightarrow N_2^*(^3\Pi_u) + e(\downarrow) \qquad (2.3)$$

or $$N_2^+ + e \longrightarrow N_2^*(^3\Pi_u) \; . \qquad (2.4)$$

Excitation -

The absolute intensity of a band in terms of photons per unit time, in the absence of collisional quenching, is

proportional to $N_{v'}A_{v'v''}$, where $N_{v'}$ is the number of molecules per unit volume in the state v', and $A_{v'v''}$ is the transition probability for a radiative transition from the level v' to the level v". The Einstein A coefficients for nitrogen have been tabulated, for example, by Nicholls (51).

The distribution of populations in various excited states of nitrogen on electron impact has been calculated approximately by Bates (52) using the Frank-Condon principle, the principle that molecular electronic transitions (both excitations and de-excitations) occur so rapidly that the internuclear separation stays constant (34,38,53). Then the probability of an allowed transition between states a and b is proportional to the overlap integral of the wave functions of the two states:

$$P_{ab} \propto \left| \int \psi_a(r) \quad \psi_b(r) dr \right|^2 . \qquad (2.5)$$

Figure 2.4 shows the potential energy functions of several N_2 and N_2^+ states (69,78). Since the Frank-Condon principle demands that transitions be vertical on this diagram, it is clear for example that the transition probability for the Vegard-Kaplan VK(0,0) transition must be very small.

At the normal temperatures prevailing in the lower atmosphere and in most laboratory experiments, the undisturbed nitrogen molecules are almost entirely in their ground electronic state and zeroth vibrational level. The rate of excitation to a level v' by electron impact is then, to a first

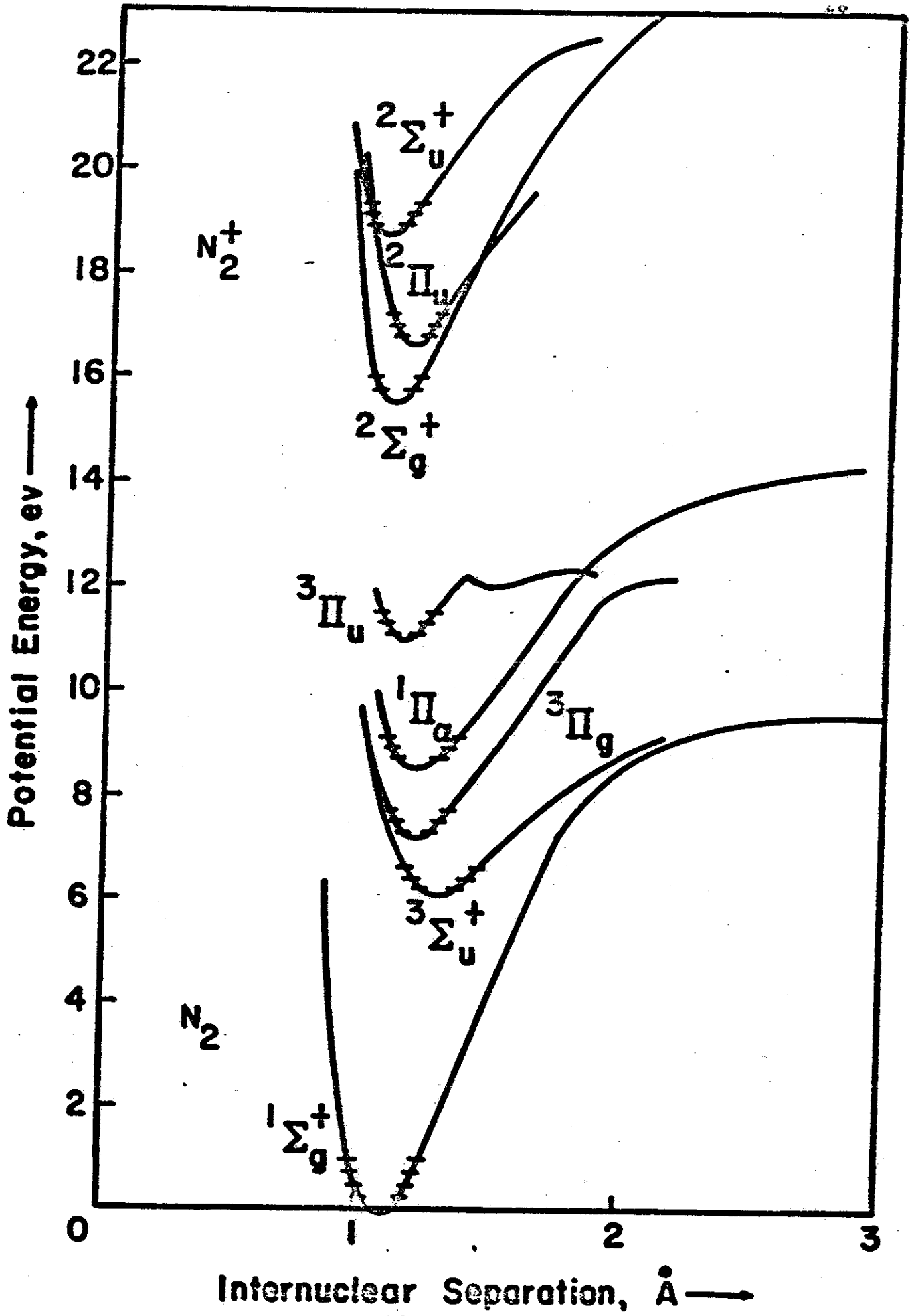
Potential Energy, ev
Internuclear Separation, Å
N_2^+
N_2
$^2\Sigma_u^+$
$^2\Pi_u$
$^2\Sigma_g^+$
$^3\Pi_u$
$^1\Pi_g$
$^3\Pi_g$
$^3\Sigma_u^+$
$^1\Sigma_g^+$
0
2
4
6
8
10
12
14
16
18
20
22
1
2
3

Figure 2.4

approximation, proportional to $\frac{A_{v'v_i}}{E_{v'v_i}^3}$, where v_i represents the initial state and $E_{v'v_i}$ is the change in energy level (52). In this case the photon flux corresponding to the transition (v',v") would be proportional to

$$\frac{A_{v'v_i}}{E_{v'v_i}^3} A_{v'v"} \qquad (2.6)$$

We may define a cross section $\sigma_v(E)$ for excitation of a level v by bombardment of particles with kinetic energy E by the equation

$$\frac{\text{No. of v excitations}}{\text{cm}^3 \text{ sec}} = N \sigma_v(E) n \qquad (2.7)$$

where N = number of molecules per cm^3

n = incident flux in particles per cm^2-sec.

Similarly the cross section for ionization producing free electrons in an energy range (E', E'+dE'), which we call $\sigma_{ion}(E,E')$, is defined by

$$\frac{\text{No. of ionizations producing electrons in } (E',E'+dE')}{\text{cm}^3 \text{ sec}} dE' = N\sigma_{ion}(E,E')n \, dE' \qquad (2.8)$$

The excitation cross sections for some of the states of N_2 and N_2^+, as well as the total ionization cross section, are shown in Figure 2.5 for electron excitation up to 10 Kev (65). The ionization potential of N_2 is 15.7 ev, whereas the average energy loss per ion pair in air is about 34 ev, so it is clear that ionization results in a distribution of secondary electrons (delta rays) having typically several electron volts

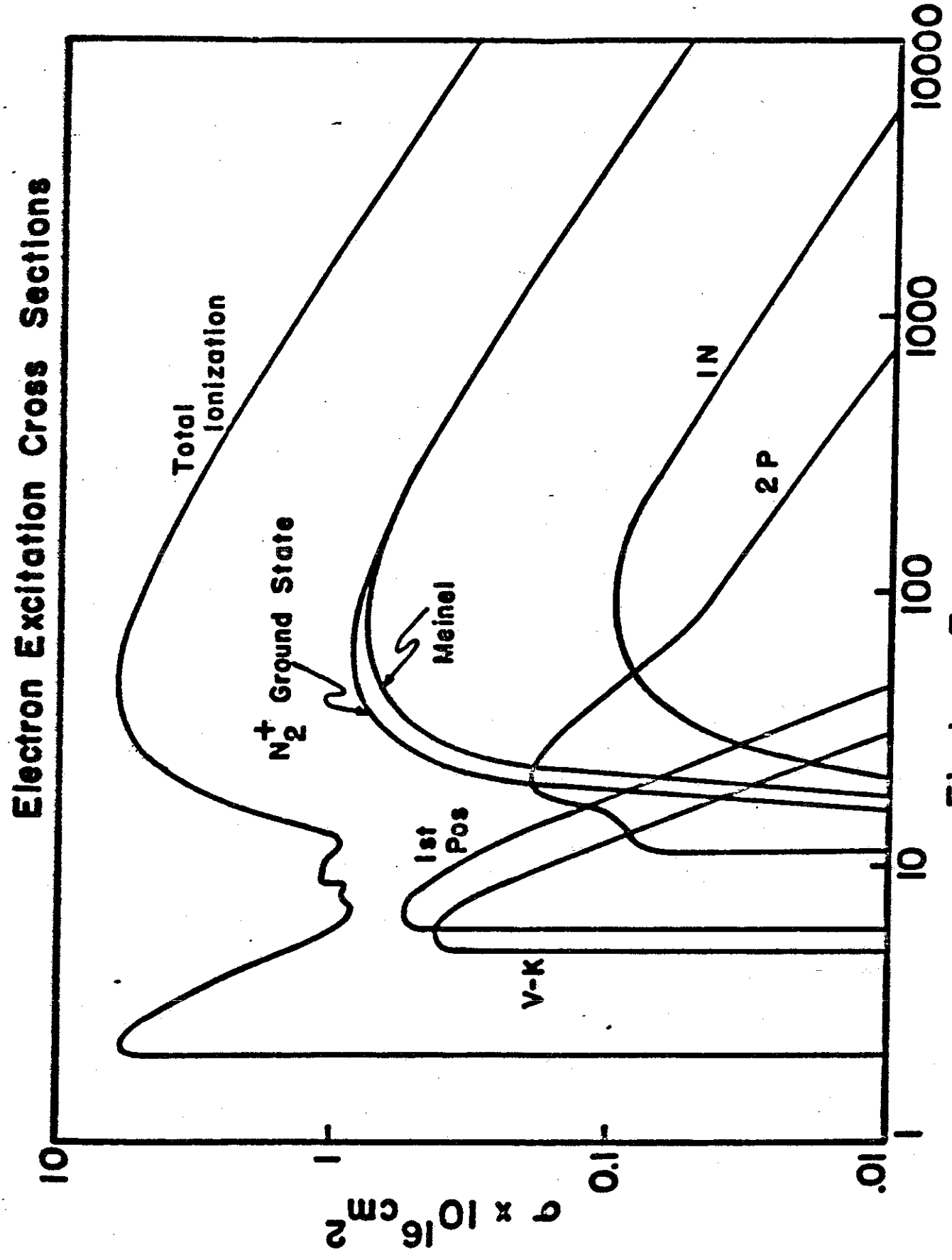
Electron Excitation Cross Sections
Total Ionization
N_2^+ Ground State
Meinel
1N
2P
1st Pos
V-K
10
1
0.1
0.01
$\sigma \times 10^{16}$ cm^2
1
10
100
1000
10000
Electron Energy, ev

Figure 2.5

energy, sufficient to excite both the B $^2\Sigma_u^+$ level and the C $^3\Pi_u$ level of N_2.

Therefore a single high energy electron of energy E passing through pure nitrogen will produce N $\sigma_{ion}^e(E,E')$ dE' secondary electrons in the energy range (E', E'+dE') per centimeter. The total number of excitations produced by a secondary electron of energy E' is given by

$$S(E') = \int_0^{E'} \frac{\sigma_v(E)\, dE}{M\left(\frac{dE}{dx}\right)} \qquad (2.9)$$

where $\frac{dE}{dx}$ is the rate of energy loss of the electron per gm/cm^2, and M is the molecular mass of the target gas.

Therefore the number of excitations to upper levels of the 2P system, for example, will be

$$\frac{\text{2P excitations}}{cm} = N\, \sigma_{2P}^e(E) + N \int_0^{E'_{max}} \sigma_{ion}^e(E,E')S(E')dE' \qquad (2.10)$$

ignoring third order effects and recombination.

Also, since a high energy particle has about equal probability of interacting with any atomic electron, a certain number of ionizations will liberate K-electrons and lead to the emission of Auger electrons. In fact, since the probability of Auger (radiationless) transition is close to 100% for nitrogen (49), approximately 2 out of 7 secondary electrons will be accompanied by Auger electrons, having an energy of about 322 ev. For oxygen, the ratio is 2 out of 8 and the

energy is 446 ev.

If we define a cross section for the Auger process for an incident particle of energy E by

$$\frac{\text{No. of Auger electrons of energy } E_A}{\text{cm}} = N\sigma_A(E) \qquad (2.11)$$

then the total number of 2P excitations for an incident electron is

$$\frac{\text{2P excitations}}{\text{cm}} = N\sigma^e_{2P}(E) + N\int_0^{E'_{max}} \sigma^e_{ion}(E,E')S(E')dE' + N\sigma^e_A(E)S(E_A) \qquad (2.12)$$

again ignoring third order effects and recombination.

On the other hand, because of the impossibility of protons directly exciting the upper level of the 2P system, a proton in nitrogen will produce

$$N^2\int_0^{E'_{max}} \sigma^p_{ion}(E,E')S(E')dE' + N\sigma^p_A(E)S(E_A)\frac{\text{2P excitations}}{\text{cm}} \cdot \qquad (2.13)$$

De-excitation -

If m molecules are excited to a level v and if τ_v, τ_c and τ_i are the mean lives of the excited state for radiation to any lower state, collisional de-excitation and internal quenching (26) respectively, then the total rate of de-excitation is

$$\frac{dm}{dt} = m\left(\frac{1}{\tau_v} + \frac{1}{\tau_c} + \frac{1}{\tau_i}\right) \text{ molecules per second} \qquad (2.14)$$

or, letting

$$\frac{1}{\tau_o} = \frac{1}{\tau_v} + \frac{1}{\tau_i} \quad , \tag{2.15}$$

$$\frac{dn}{dt} = m\left(\frac{1}{\tau_o} + \frac{1}{\tau_c}\right) \quad \text{molecules per second} \tag{2.16}$$

and the quantum efficiency of fluorescence is the ratio of the rate of de-excitation by radiation to the total rate of de-excitation:

$$\text{Fluorescent Efficiency} = \frac{(\tau_o/\tau_v)}{1 + \tau_o/\tau_c} \text{ photons per excitation.} \tag{2.17}$$

From kinetic energy, the mean time between quenching collisions in pure nitrogen is given by

$$\tau_c = \frac{1}{\sqrt{2}\, N\, \sigma_{nn}\, \bar{v}} \tag{2.18}$$

where σ_{nn} = cross section for nitrogen-nitrogen collisional de-excitation in cm^2.

$\bar{v}$ = mean molecular velocity = $\sqrt{\frac{8kT}{\pi M}}$.

Therefore $\tau_c = \frac{1}{4N\sigma_{nn}} \sqrt{\frac{\pi M}{kT}}$ (2.19)

where M = molecular mass.

In general, σ_{nn} will be different for different excited states and will be a function of temperature.

Using the ideal gas law, p = NkT, and therefore we may write τ_c in terms of the gas pressure, p:

$$\tau_c = \sqrt{\frac{\pi MkT}{4\sigma_{nn}}}\,\frac{1}{p}$$

$$= \frac{\sqrt{\pi MkT}}{\sigma_{nn}}\,\frac{1.87\times10^{-4}}{p} \quad \text{seconds} \qquad (2.20)$$

where p is measured in mm Hg.

Letting

$$p' = \frac{\sqrt{\pi MkT}}{\sigma_{nn}}\,\frac{1.87\times10^{-4}}{\tau_o} \quad \text{mm Hg,} \qquad (2.21)$$

we then have

$$\text{Fluorescent efficiency} = \frac{(\tau_o/\tau_v)}{1 + p/p'} \quad \text{photons per excitation.} \qquad (2.22)$$

The decay time of the fluorescence, τ, is given by

$$\frac{1}{\tau} = \frac{1}{\tau_v} + \frac{1}{\tau_i} + \frac{1}{\tau_c} = \frac{1}{\tau_o} + \frac{1}{\tau_c} \qquad (2.23)$$

or,

$$\tau = \frac{\tau_o}{1 + \tau_o/\tau_c} = \frac{\tau_o}{1 + p/p'} \quad . \qquad (2.24)$$

Thus τ_o is the fluorescence decay time in the absence of collisional quenching.

Various authors have discussed collisional deactivation in molecular nitrogen (26,38,45,48,50). While the description above measures the quenching effect in terms of deactivation cross section σ, or reference pressure p', an equivalent description can be given in terms of quenching speed δ or quenching coefficient z defined below.

The quenching coefficient is defined as

$$z = \frac{p}{Np'} = \frac{7.5\times10^{-4}\ kT}{p'}\ \text{cm}^3 \quad (47) \qquad (2.25)$$

The quenching speed is defined as $\delta = u\sigma$, where u is the average relative velocity of the gas molecules and equals $\sqrt{2}$ times the mean molecular velocity, $\bar{v}$ (44). Therefore $\delta = \frac{z}{\tau_o}$, and is measured in cm^3/sec. δ is also the rate of reaction in the equation

$$\frac{dN^*}{dt} = -\delta N^* N, \tag{2.26}$$

where N^* represents the density of excited molecules.

In a gas which is a mixture of two components the above equations must be modified. For example, an excited N_2 molecule in air may encounter a deactivating collision with an O_2 molecule, the number of such collisions being

$$\frac{1}{\tau_{no}} = N_o \sigma_{no} u = 2N_o \sigma_{no} \sqrt{\frac{2kT\,(M_n + M_o)}{\pi\, M_n M_o}} \text{ deactivations} \tag{2.27}$$

with oxygen per second (38) where σ_{no} is the effective nitrogen-oxygen collision cross section for de-excitation, N_o is the number of oxygen molecules per cm^3, and M_n and M_o are the nitrogen and oxygen molecular masses.

Then if m nitrogen molecules are excited to a particular excited state, the total rate of de-excitation is given by

$$\frac{dm}{dt} = m\left(\frac{1}{\tau_o} + \frac{1}{\tau_{nn}} + \frac{1}{\tau_{no}}\right) \text{ molecules per second.} \tag{2.28}$$

Therefore the decay time of the fluorescence is given by

$$\tau = \frac{\tau_o}{1 + \tau_o\left(\frac{1}{\tau_{nn}} + \frac{1}{\tau_{no}}\right)} \tag{2.29}$$

and the fluorescent efficiency is

$$\frac{(\tau_o/\tau_v)}{1 + \tau_o(\frac{1}{\tau_{nn}} + \frac{1}{\tau_{no}})} \quad \text{photons per excitation}$$

$$= \frac{(\tau_o/\tau_v)}{1 + p/p'} \quad \text{photons per excitation,} \qquad (2.30)$$

where

$$\frac{1}{p'} = \frac{\tau_o}{1.87\times10^{-4}\sqrt{\pi MkT}} \left(f_n\sigma_{nn} + f_o\sigma_{no}\sqrt{\frac{M_n + M_o}{2M_o}} \right) (\text{mm Hg})^{-1} \qquad (2.31)$$

f_n and f_o being the fractions by volume of the two constituents. Therefore the quenching speed becomes

$$\delta = 4\sqrt{\frac{kT}{\pi M_n}} \left(f_n\sigma_{nn} + f_o\sigma_{no}\sqrt{\frac{M_n + M_o}{2M_o}} \right) \text{cm}^3/\text{sec.} \qquad (2.32)$$

For air, $f_n = 0.79$, $f_o = 0.21$, and the factor $\sqrt{\frac{M_n + M_o}{2M_o}} = 0.967$.

The radiative lifetimes and the quenching cross sections depend on the excited state and in general depend on the vibrational quantum number as well as the electronic parameters of the state (50). In fact, the inverse radiative lifetime of an excited state v' is equal to the sum of the Einstein transition probabilities for all the possible radiative transitions from this state:

$$\frac{1}{\tau_{v'}} = \sum_{v''} A_{v'v''} \qquad (2.33)$$

The foregoing analysis can be applied to all the excited states of nitrogen and in particular, if the excitation cross

sections are such that the fluorescent efficiency of a band at λ_i in the absence of collisional quenching is $E(\lambda_i)$ (electron volts of optical output per ev deposited), then the pressure dependence of the efficiency will be a sum over all bands:

$$E(p) = \sum_i \frac{E(\lambda_i)}{1 + p/p_i'} \qquad (2.34)$$

The decay of the fluorescence from many bands will, of course, no longer be a simple exponential if the various excited states have different decay times, and in fact the intensity of the fluorescence as a function of time $I(t)$ will obey a sum of exponentials

$$I(t) \propto \sum_i E(\lambda_i) \exp\left[-\frac{t}{\tau_o}\left(1 + \frac{p}{p'}\right)\right] \qquad (2.35)$$

Experimental Studies -

To compare these predictions with available experimental information, it is necessary to understand that measurements on the excitation of a gas may be made under thin target, thick target or total absorption conditions. Thin target conditions mean that the exciting particles lose a small fraction of their kinetic energy in traversing the measurement volume. In a thick target, account must be taken of the changing energy and consequent changing specific ionization of the exciting particle. In the total absorption case, the number of excitations and ionizations produced is a function of the incident particle energy only, and not of the gas pressure. The equations on

pages 31-32 refer to thin target conditions.

Table 2.1 summarizes the predicted low pressure relative intensities of the prominent nitrogen bands for electron excitation, based on calculations of Bates (52) and low pressure measurements by Tyte (57), Smyth and Arnott (56). The accuracy is poor for the weaker bands. The units are arbitrary, normalized to 100 for the 1N (0,0) band and to 30 for the 2P (0,0) band. The relative intensity of the 1N and 2P systems depends strongly on the geometry of the arrangement for light collection from the target gas because of the difference in excitation mechanisms. The energy distribution of the secondary electrons becomes softer in the region peripheral to the exciting beam and near the end of the range of the primary particles, preferentially exciting the 2P system in these regions. The measured ratio of the intensities of the transitions 1N(0,0)/2P(0,0) for electron excitation ranges from 2.5 to 5 (31,39,52,56). The ratio of 1N intensity to 2P intensity is considerably greater for heavy particle excitation (37,58,59), because of the impossibility of heavy particles directly exciting the C $^3\Pi_u$ state.

The absolute fluorescent efficiency at low pressures has been studied in detail for one transition, the famous 3914 Å band (55,60,61). The results of calculations by Frankenthal, Manley and Treve (61) and an experimental measurement by Hartman (31) are summarized in Figure 2.6 for electron impact on nitrogen. The fall-off of fluorescent efficiency for

Table 2.1

Predicted Low Pressure Relative Intensities of Nitrogen Bands (normalized to 100 for 3914 Å)

System	v'	v''	λ(Å)	Intensity
1N	0	0	3914	100
		1	4278	32
		2	4709	6.7
		3	5228	1
	1	0	3582	5.6
		1	3884	3.8
		2	4236	3.8
		3	4652	1.8
		4	5149	0.4
2P	0	0	3371	30
		1	3577	19
		2	3805	6.6
		3	4059	1.8
		4	4344	0.3
		5	4667	0
	1	0	3159	25
		1	3339	1.3
		2	3537	8.8
		3	3756	8.2
		4	3998	3.7
		5	4270	0.4
		6	4574	0
2P	2	0	2977	4.6
		1	3136	8.1
		2	3309	0.6
		3	3500	1.2
		4	3711	2.7
		5	3943	2.0
		6	4201	1.3
		7	4490	0.4
	3	0	2820	
		1	2962	4.1
		2	3117	3.2
		3	3285	1.4
		4	3469	
		5	3672	0.8
		6	3894	
		7	4141	0.5
		8	4416	0.2

electrons above 1 Mev is due mainly to the onset of radiative energy loss (bremsstrahlung). The variation with electron energy below 100 Kev is due largely to the fall-off of the first negative excitation cross section (Figure 2.5) as the average energy of the secondary electrons, which are mainly responsible for the excitations, falls below 100 electron volts.

The absolute efficiency at high pressures has been measured for nitrogen and for air by Davidson and O'Neil (32) and Bunner (30), with fair agreement (see Table 2.6). The pressure dependence of the 2P(0,0) transition in air has been measured directly by Bunner (30) which, along with revised calculations, yields a value for $p'_{2P,0}(\text{Air})$ of $15\ ^{+2}_{-5}$ mm Hg. These results are shown in Figure 2.7. Also, Schmidt (41) has measured the scintillation decay time of pure nitrogen at high pressures as a function of pressure, yielding $p'_{2P,0}(N_2) = 90$ mm Hg. The difference of a factor 6 between this value of p' and the value obtained by Bunner for air reveals the strength of the quenching influence of oxygen.

Armed with these experimental data, we are now prepared to calculate the quenching coefficients or deactivation cross sections for the various radiative species of nitrogen. These numbers are shown in Table 2.2, and refer to a gas temperature of 300°K. The values $p'_{1N,0}(N_2) = 15$ mm Hg and $p'_{2P,0}(\text{Air}) = 90$ mm Hg are accepted, and values for the other cases are calculated by comparison of the low pressure relative intensities (Table 2.1) and the high pressure measurements of

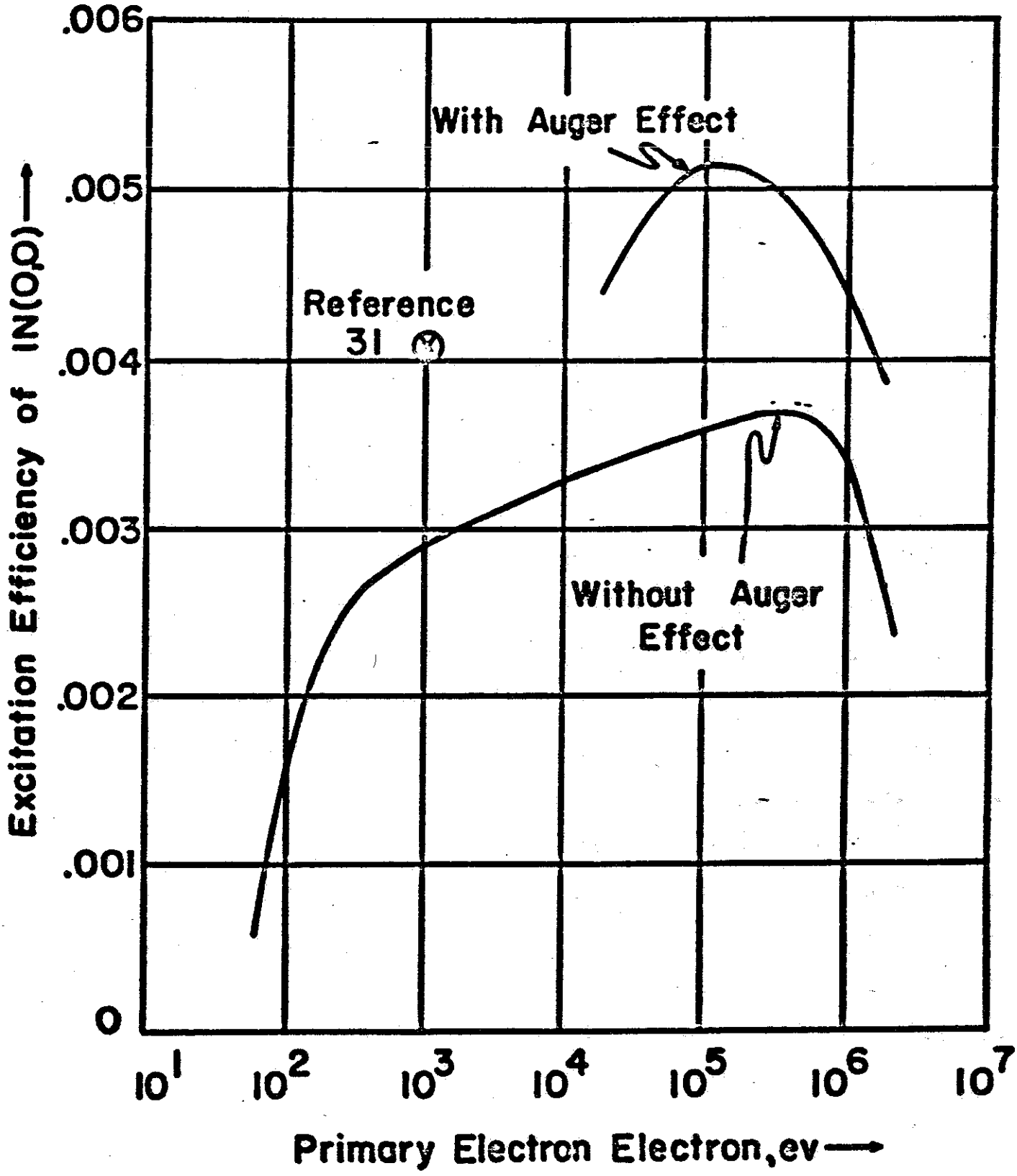
.006
.005
.004
.003
.002
.001
0
Excitation Efficiency of IN(O,O)
With Auger Effect
Reference
31
Without Auger
Effect
10^1
10^2
10^3
10^4
10^5
10^6
10^7
Primary Electron Electron, ev

Figure 2.6

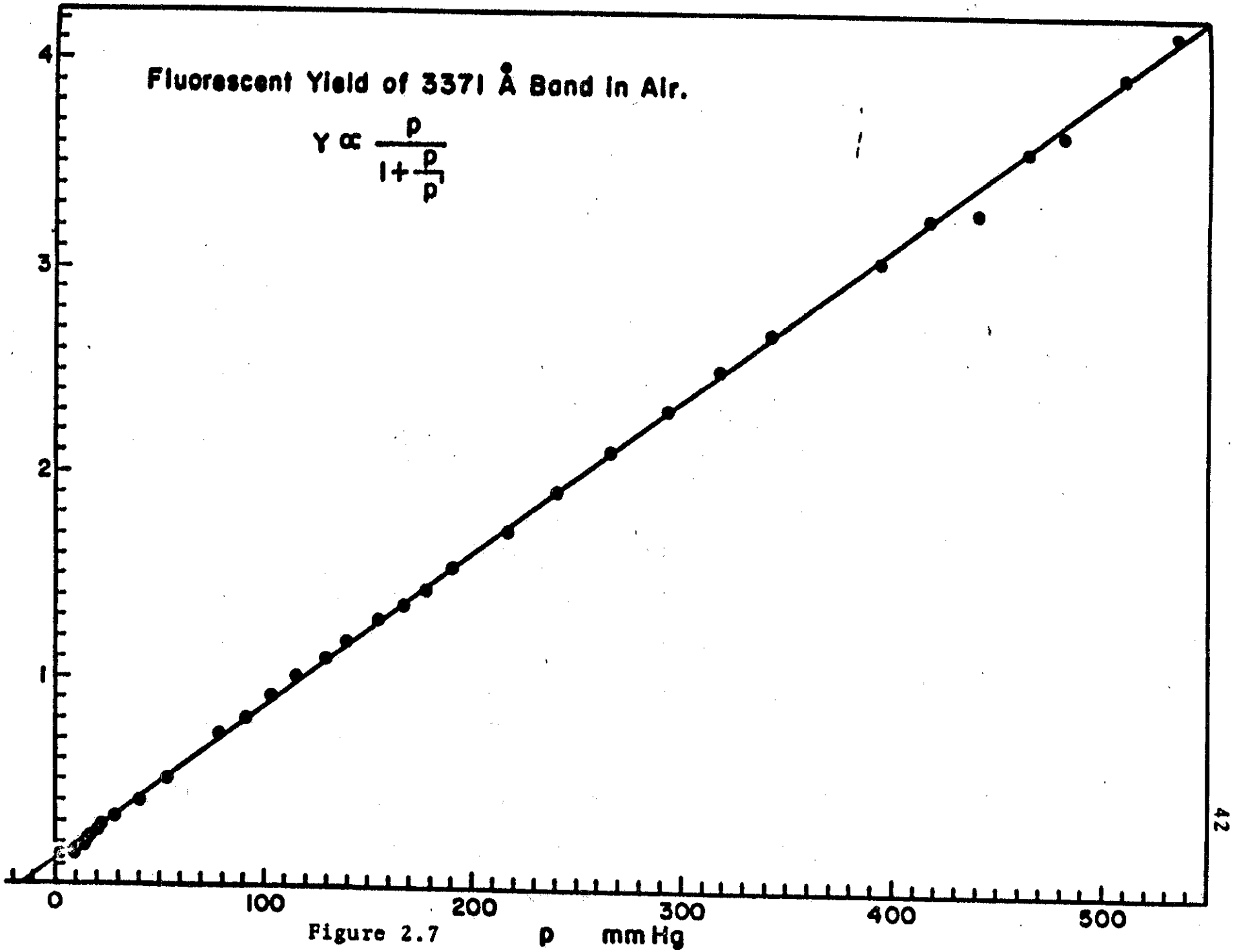
Fluorescent Yield of 3371 Å Band in Air.
$Y \propto \frac{p}{1+\frac{p}{p'}}$
p/Y Arbitrary Units
0
1
2
3
4
100
200
300
400
500
p mm Hg

Figure 2.7

Table 2.2

Deactivation Constants for Nitrogen and Air

		$p'(N_2)_{mm}$	$p'(Air)_{mm}$	$\delta(N_2)\ \frac{cm^3}{sec}$	$\delta(Air)\ \frac{cm^3}{sec}$	$\sigma_{no}\ cm^2$	$\sigma_{nn}\ cm^2$	$\tau_o \times 10^8$ sec
1N	v = 0	1.49	1.08	2.9×10^{-10}	4.0×10^{-10}	13×10^{-15}	4.37×10^{-15}	$6.58\pm.35$
2P	v = 0	90	15	7.0×10^{-12}	4.2×10^{-11}	2.1×10^{-15}	1.0×10^{-16}	$4.45\pm.6$
	1	24.5	6.5	2.3×10^{-11}	8.8×10^{-11}		3.5×10^{-16}	4.93
	2	10.9	4.6	5.8×10^{-11}	1.4×10^{-10}		8.8×10^{-16}	4.45
	3	5.4	2.5	7.7×10^{-11}	1.7×10^{-10}		1.2×10^{-15}	6.65

Table 2.3 (Reference 50)

1N	v = 0	$1.18\pm.42$	1.2	3.8×10^{-15}	5.53×10^{-15}
2P	v = 0	66.7 ± 9	9.45		
	1	24.4 ± 2.4	8.05		
	2	21.3 ± 4.3	7.65		

Davidson and O'Neil and Bunner. Also shown for comparison are the results of experimental studies by Brocklehurst (50). The right-hand column shows the radiative lifetime of the important levels, from Bennett and Dalby (63) and Nicholls (51).

There are experimental discrepancies, however. The measurements of Davidson and O'Neil indicate, provided their method of excitation of nitrogen and of air were the same, that $p'_{2P,0}(N_2)$ is about 20 times larger than $p'_{2P,0}(Air)$, inconsistent with the results of Schmidt and Bunner, and with the results of Brocklehurst. In fact, a comparison of Davidson and O'Neil's results for nitrogen and air yields directly the ratios shown in the table below:

Table 2.4

	$p'_{1N,v}(N_2)/p'_{1N,v}(Air)$	$p'_{2P,v}(N_2)/p'_{2P,v}(Air)$
v = 0	1.38	22.3 ± 3
1		10.5
2		7.4
3		3.8

Brocklehurst measured the deactivation of nitrogen fluorescence by bombarding nitrogen and nitrogen-oxygen mixtures at various pressures with 5 Kev to 45 Kev X-rays. However, some doubt is cast upon his results due to his assumption that the pressure variation of his light collecting efficiency is the same for all bands. In fact, at low pressures, secondary

electrons may reach the walls before dissipating all their energy, thus decreasing the yield of 2P radiation relative to 1N radiation. This would mean that radiating species actually having small p' values would appear to have higher values.

Calculation of quenching speeds and deactivation cross sections from p' requires knowledge of the radiative lifetime τ, which also has some uncertainty. While most investigators accept the values found by Bennett and Dalby (63), Schmidt (41) has inferred considerably shorter lifetimes from a study of scintillation decay times, namely 3.4×10^{-8} sec for the 1N system and 2.4×10^{-8} sec for the 2P system. Jeunehomme and Duncan (68) have measured a lifetime of $3.82 \pm 0.8 \times 10^{-8}$ sec for the 2P,0 state, while a later paper by Jeunehomme (84) finds $\tau_o(1N,0) = 7.15 \pm 0.50 \times 10^{-8}$ sec and $\tau_o(2P,0) = 4.9 \pm 0.5 \times 10^{-8}$ sec. Anton (83) has used a modulated discharge and phase sensitive detector to find $\tau_o = 3.7 \pm 0.3 \times 10^{-8}$ sec for the spectral region 3000 Å to 3900 Å, which is predominantly 2P,0 radiation. These results are summarized in Table 2.5. At very low pressures, the measurements of radiative lifetimes may be affected by contributions due to recombination or cascading processes. In this case the decay of the fluorescence may reflect a superposition of two or more decay processes. After consideration of these questions, Jeunehomme (84) has recommended values of $6.75 \pm 0.5 \times 10^{-8}$ seconds for the true 1N,0 radiative lifetime and $4.7 \pm 0.8 \times 10^{-8}$ seconds for the true 2P,0 lifetime.

A number of other laboratory experiments have studied

Table 2.5

Experimental Nitrogen Radiative Lifetimes in Nanoseconds

Reference	^1N $v' = 0$	^2P $v' = 0$	^2P $v' = 1$	^2P $v' = 2$	^2P $v' = 3$
Bennett and Dalby (63)	65.8±3.5	44.5±6			
Nicholls (assuming $\tau_o(^2P,0) = 44.5$)			49.3	44.5	66.5
Schmidt (41)	34	24			
Jeunehomme and Duncan (68)		38.2±8.0			
Fink and Welge (92)	65 ± 4	27 ± 5			
Jeunehomme (84)	71.5±5.0	49 ± 5			
Anton (83)	40 ± 20	37 ± 3			

various aspects of the fluorescence of nitrogen without resolving the spectral components of the radiation. Grun and Schopper (45) have measured the fluorescent yield of nitrogen-oxygen mixtures at a constant pressure p = 585 mm Hg as a function of O_2 concentration. They do not observe as strong an oxygen quenching effect as Davidson and O'Neil's results would predict, finding

$$\frac{\text{Yield (Air)}}{\text{Yield } (N_2)} = .20 \quad \text{at } p = 585 \text{ mm Hg.} \quad (2.36)$$

However, Grun and Schopper's data are consistent with the parameters $p'_{2P,0}(N_2) = 90$, $p'_{1N,0}(N_2) = 1.18$, $p'_{2P,0}(\text{Air}) = 15$ and $p'_{1N,0}(\text{Air}) = 1.0$ mm Hg of Table 2.2, and a best fit then yields that at an oxygen concentration of 21%, the composition of air, the emission seen is 70% 2P, v' = 0 radiation.

Grun and Schopper also measured the pressure dependence of the fluorescence of pure nitrogen bombarded by 4.6 Mev alpha particles under thin target conditions (45). Their results are consistent with a single quenching equation of the form

$$\text{Yield} \propto \frac{p}{1 + p/p'} \text{ , with } p' = 35 \text{ mm Hg.} \quad (2.37)$$

However, the data may also be fitted quite closely by the sum of three terms

$$\text{Yield} \propto \frac{.05p}{1 + p/90} + \frac{.27p}{1 + p/24.5} + \frac{.65p}{1 + p/1.18} \quad (2.38)$$

which takes account of transitions from the three levels 2P,0 2P,1 and 1N,0.

Grun and Schopper applied a photomultiplier with an S-5 spectral response, thus observing fluorescence from well into the ultraviolet.

Legler (93) repeated the experiment of Grun and Schopper, exciting pure nitrogen with a low energy electron swarm and viewing the fluorescence with an S-11 photomultiplier. Legler found $p' = 60 \pm 10$ mm Hg, which may be understood as the consequence of a more restricted spectral response. Also, the low energy electron swarm may be expected to excite more second positive emission relative to first negative emission than the alpha particle source.

The pressure dependence of pure nitrogen emission on alpha particle bombardment has also been studied by Brown and Miller (64) under thin target conditions. Their data are quite detailed in the pressure range 0.2 to 100 mm Hg and are not consistent with $p'_{1N}(N_2) = 1$ mm Hg, provided the conditions of excitation are still linear at this low pressure, that is, provided the secondary electrons which are predominantly responsible for the excitation are still totally absorbed in the target gas. However, the data may be fitted quite well by the sum of three terms

$$\text{Yield} \propto \frac{.05p}{1 + p/90} + \frac{.004p}{1 + p/20} + \frac{.93p}{1 + p/0.5} \qquad (2.39)$$

implying $p'_{1N,0}(N_2) \approx 0.5$ mm Hg. Brown and Miller's experiment is not, however, a sensitive test of the high pressure parameter $p'_{2P,0}(N_2) = 90$.

Schmidt (41) has made a detailed study of the scintillation decay times of nitrogen and other gases, excited by 50 Kev electrons, as a function of pressure, by means of a modulated source and a phase sensitive detector. His results are plotted in Figure 2.8. Schmidt interprets these results as due to 1N radiation with $\tau_o = 3.4 \times 10^{-8}$ sec and $p'_{1N}(N_2) = 4.6$ mm Hg for $p < 10$ mm Hg, and primarily 2P radiation for $p > 10$ mm Hg with $\tau_o = 2.4 \times 10^{-8}$ sec and $p'_{2P}(N_2) = 90$ mm Hg.

The observed decay time of the fluorescence as seen by a detector lacking spectral resolution will be a weighted average of the decay times of the different upper levels involved, the weights being the observed relative intensities of the radiating species as a function of pressure.

$$\text{If } \tau_{1N}(p) = \frac{\tau_{1N}(0)}{1 + p/p'_{1N}} \text{ and } \tau_{2P}(p) = \frac{\tau_{2P}(0)}{1 + p/p'_{2P}}, \qquad (2.40)$$

then

$$\tau_{(\text{observed})} = \frac{Y_1}{Y_1 + Y_2}\left(\frac{\tau_{1N}(0)}{1 + p/p'_{1N}}\right) + \frac{Y_2}{Y_1 + Y_2}\left(\frac{\tau_{2P}(0)}{1 + p/p'_{2P}}\right); \qquad (2.41)$$

and if

$$Y_1 = \frac{Cp}{1 + p/p'_{1N}} \quad \text{and} \quad Y_2 = \frac{Ap}{1 + p/p'_{2P}}, \qquad (2.42)$$

then

$$\tau(p)_{(\text{observed})} = \frac{\dfrac{Cp\tau_{1N}(0)}{(1 + p/p'_{1N})^2} + \dfrac{Ap\tau_{2P}(0)}{(1 + p/p'_{2P})^2}}{\dfrac{Cp}{1 + p/p'_{1N}} + \dfrac{Ap}{1 + p/p'_{2P}}} \qquad (2.43)$$

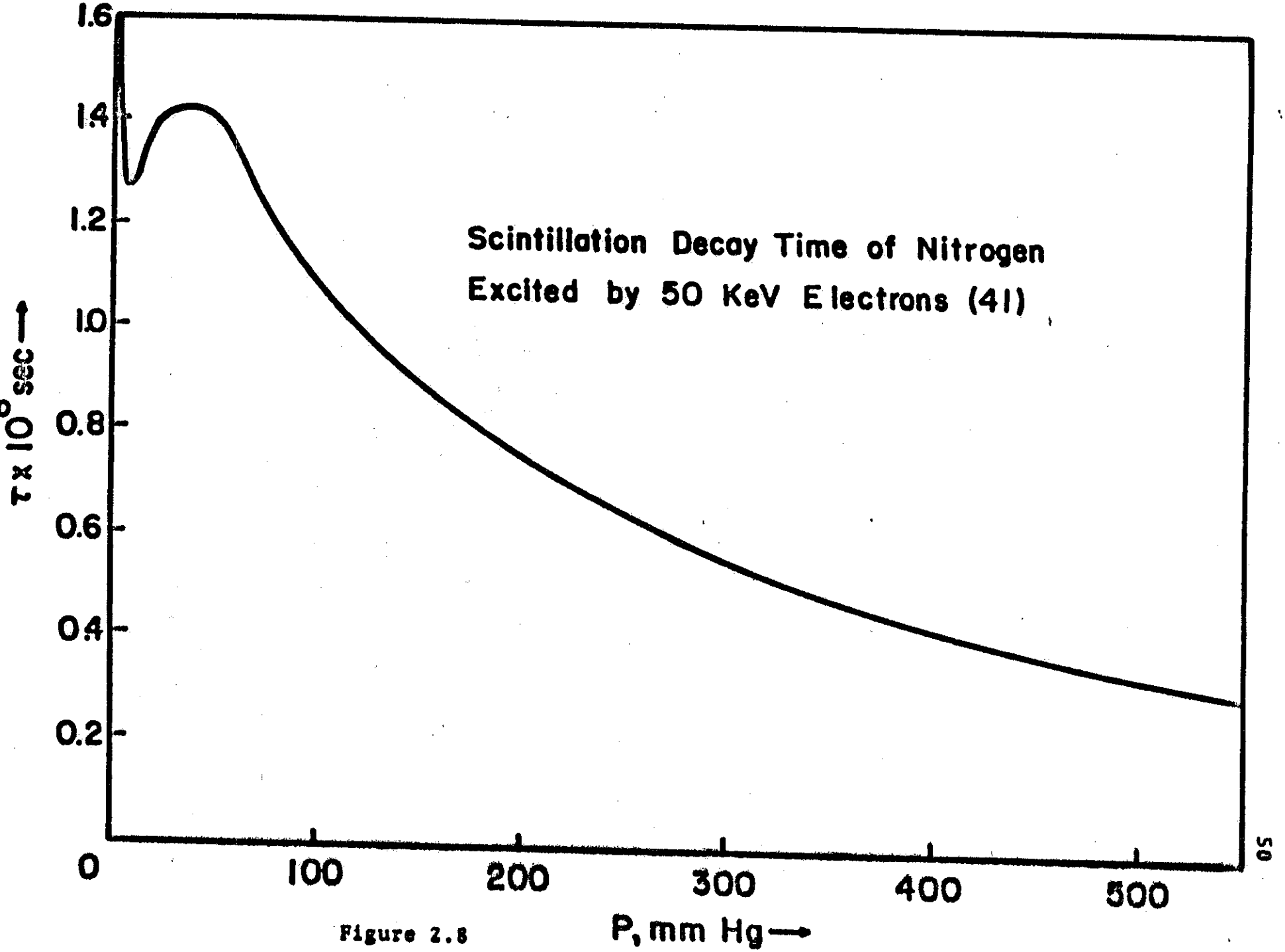
Scintillation Decay Time of Nitrogen
Excited by 50 KeV Electrons (41)
τ x 10^8 sec
P, mm Hg
1.6
1.4
1.2
1.0
0.8
0.6
0.4
0.2
0
100
200
300
400
500
50

Figure 2.8

Fitting Schmidt's data to this function, a somewhat smaller value of p'_{1N} is required than Schmidt's value. In fact, a good fit to the data is obtained with the parameters

$$\left.\begin{aligned} &p'_{1N} = 1 , \quad p'_{2P} = 90 \text{ mm Hg} \\ &\tau_{1N}(0) = 3.73 , \quad \tau_{2P}(0) = 2.63\times10^{-8} \text{ sec} \\ &C/A = 10 , \end{aligned}\right\} \qquad (2.44)$$

implying as usual that the first negative emission is dominant by a large factor at very low pressures. No explanation is offered for these apparently low values of the radiative lifetimes.

Schmidt (41) has also studied the scintillation decay times of nitrogen held at a fixed partial pressure of 100 mm Hg, adding oxygen to determine its quenching power. At this pressure the fluorescence is predominantly 2P,0 radiation. He finds

$$\tau(p) = \frac{1.1\times10^{-8} \text{ sec}}{1 + \frac{p(O_2)}{6 \text{ mm}}} , \qquad (2.45)$$

where $p(O_2)$ is the partial pressure of oxygen, which implies that $\sigma_{no}(2P)/\sigma_{nn}(2P) = 33$, if $p'_{2P}(N_2) = 90$ mm Hg. This result agrees well with Brocklehurst (50), who finds the ratio $\sigma_{no}(2P,0)/\sigma_{nn}(2P,0) = 31$, although Brocklehurst reported $p'_{2P,0}(N_2) = 66.7$ mm Hg.

The results of Davidson and O'Neil, on the other hand, show a more severe effect from oxygen on comparison of their fluorescent efficiencies for air and nitrogen, yielding a ratio $\sigma_{no}(2P,0)/\sigma_{nn}(2P,0) = 100$, fairly insensitive to the

value of $p'_{2P}(N_2)$. The possible errors in these ratios are on the order of 10 to 20% and this discrepancy remains unresolved.

Finally, Grun (33) has measured the fluorescent efficiency of air bombarded by 4 to 40 Kev electrons, under thin target conditions, as a function of pressure from 10 to 600 mm Hg. Plotting the reciprocal of the light yield versus pressure, Grun finds a linear function that is fitted by

$$\frac{1}{\phi} = 1 + \frac{p}{11.5 \text{ mm}} \quad . \tag{2.46}$$

However, again because of the property that a sum of terms of the form $\frac{A_i}{1 + p/p'_i}$ may closely resemble a function $\frac{B}{1 + p/p'_{eff}}$, Grun's data may be fitted to within the accuracy of the experimental points by the sum of three terms:

$$\phi = \frac{.58}{1 + p/15} + \frac{.32}{1 + p/6.5} + \frac{.7}{1 + p/1} \quad , \tag{2.47}$$

which we interpret as the contributions of the 2P,0 2P,1 and 1N,0 band systems, respectively. However, Grun's data do not provide a sensitive test of the value of the low pressure parameter $p'_{1N}(Air)$.

An estimate of $p'_{1N}(Air) = 6$ mm Hg was made by Bunner (30) on the basis of measurements of the absolute fluorescent efficiency of the 3914 Å band at a few different pressures. However, the pressure was accurately monitored only as low as 20 mm Hg and therefore the accuracy of this determination is very poor. In fact, combining Bunner's results with the absolute 3914 Å band measurements of Davidson and O'Neil (32)

and Hartman (31) yields the graph shown on the next page, which is fairly well fitted by $p'_{1N}(\text{Air}) = 1.1$ mm Hg.

For the first negative, v' = 1 level, comparison of Davidson and O'Neil's figure for the fluorescent efficiency of the 5149 Å band at 600 mm Hg with the low pressure measurements of Hartman (31) and with Table 2.1 indicates that $p'_{1N,1}(\text{Air}) = 2.0 \pm 1.5$ mm Hg and $p'_{1N,1}(N_2) < 7$ mm Hg. The radiative lifetime of this state, from Jeunehomme, is 7.6×10^{-8} seconds, and therefore $\sigma_{nn}(1N,1) > 8 \times 10^{-16}$ cm^2.

In summary, the best self-consistent set of collision quenching parameters is provided by Table 2.2. Since the distribution of secondary electron energies and the energy dependence of the excitation cross sections are still not well known for high energy particle impact, in order to calculate the absolute fluorescent efficiency, $E(\lambda_i)$, in the absence of quenching, we must combine these quenching parameters with the absolute efficiency measurements of Hartman, Bunner, and Davidson and O'Neil. Table 2.6 shows their experimental results for the 2P and 1N band systems extrapolated to zero pressure using Table 2.1 along with the low pressure discharge relative intensity expectations from Bates (52) and Tyte (57), normalized arbitrarily to 0.33% at 3914 Å. Hartman's attention was concentrated on the 3914 Å band, and the efficiency for other bands in this column has been estimated from his published spectrum (31). Davidson and O'Neil's study extended well into the red end of the spectrum, and Bunner's results went well into the ultraviolet. All three experimenters estimated an accuracy of

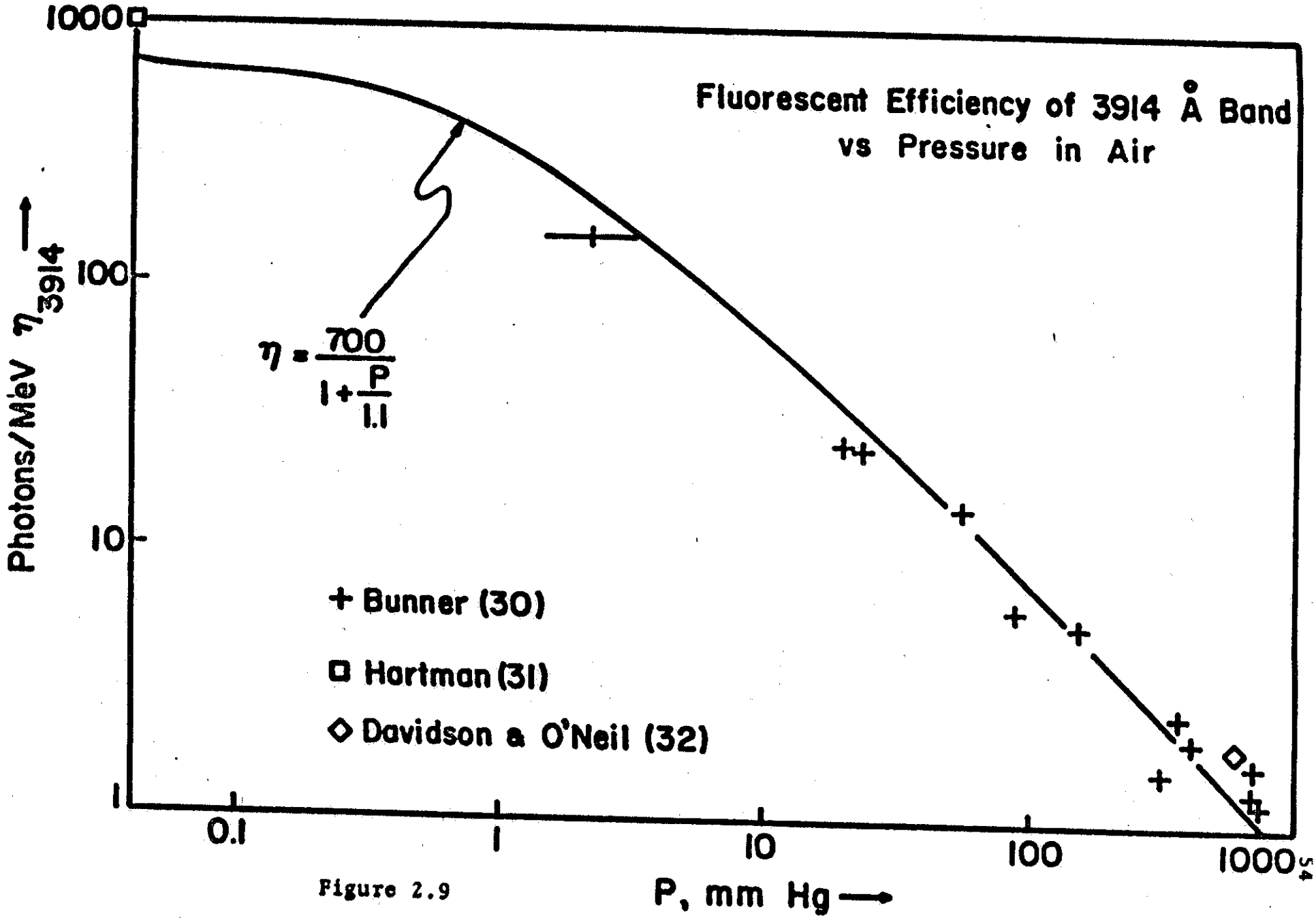
Fluorescent Efficiency of 3914 Å Band
vs Pressure in Air
Photons/MeV η_{3914} ⟶
1000
100
10
1
$\eta = \frac{700}{1+\frac{P}{1.1}}$
+ Bunner (30)
□ Hartman (31)
◇ Davidson & O'Neil (32)
0.1
1
10
100
1000
P, mm Hg ⟶

Figure 2.9

Table 2.6

Experimental Results for Efficiencies of 2P and 1N Bands in Air, Extrapolated to Zero Pressure

Transition (v',v") (2P system, unless otherwise noted)		λ, Å	Ref. 32 %	Ref. 30 %	Ref. 31 %	Low Pressure Relative Intensity	Best Value %
	(3,0)	2820		.011			.011
	(2,0)	2977		.019		.015	.016
	(1,0)	3159		.050	.029	.084	.050
	(3,3)	3285	.0154	.0090	.0158	.0046	.0154
	(0,0)	3371	.086	.035	.082	.100	.082
	(3,4)	3469	.0063	.0193			.0063
	(2,3)	3500	.0029	.0092		.0040	.0040
	(1,2)	3537	.0298	.017	~.029	.0291	.029
	(0,1)	3577	.0615	.024	.066	.0628	.0615
	(3,5)	3672	.0046		~.01	.0026	.0046
	(2,4)	3711	.010	.010	~.03	.009	.010
	(1,3)	3756	.028	.0168		.0271	.0271
	(0,2)	3805	.0213	.017		.0218	.0213
1N	(0,0)	3914	.421	.272	.33	.33	.33
	(2,5)	3943	.0064			.0066	.0064
	(1,4)	3998	.017	.0145	~.016	.0122	.016
	(0,3)	4059	.0074	.0067	~.013	.0059	.0067
	(2,6)	4201	.0046			.0041	.0046
	(1,5)	4270	~.0035	~.0035		.0013	.0035
1N	(0,1)	4278	.120	~.11	.082	.106	.11
	(0,4)	4344	.0019			.0010	.0019
	(2,7)	4490	.0015	.0018		.0011	.0015
	(1,6)	4574	.0015	.0016	~.003		.0016
	(0,5)	4667	.0004		~.004		.0004
1N	(0,2)	4709	.021	.020	.009	.022	.020
	(2,8)	4815	.0008		.0008		.0008
	(1,7)	4917	.0004				.0004

not better than $\pm$ 30%. Agreement is fair, with the most serious discrepancy being between Bunner and Davidson and O'Neil concerning the 2P(0,0) and 2P(0,1) bands. Since the latter used 50 Kev electrons rather than heavy ions, we are tempted to favor their values. Also, the spectral resolution of the D and O experiment was higher, allowing less possibility of error due to overlapping bands. The final column offers a set of weighted averages which appear to provide the best available numbers for the $E(\lambda_i)$ for high energy electrons. Until more detailed measurements for individual spectral bands are made we shall use these figures, along with Table 2.2, for estimation of the photon yield from cosmic ray air showers. These estimates are summarized together in Table 2.8.

Other Band Systems -

Low pressure studies have shown that considerable energy is also channelled into excitation of the A $^2\Pi_u$ and C $^2\Sigma_u^+$ states of N_2^+, the upper levels of the Meinel and second negative band systems. In fact, nitrogen ionizations on electron impact appear to divide up approximately as follows: (65,66,67)

50% X $^2\Sigma_g^+$ (Ground State)

40% A $^2\Pi_u$ (Meinel)

8% B $^2\Sigma_u^+$ (First Negative)

1% C $^2\Sigma_u^+$ (Second Negative)

Excitation cross sections for N_2 published by Green and

Barth (65) show that excitation to singlet states such as a $^1\Pi_g$, b $^1\Pi_u$, h $^1\Sigma_u^+$ must account for much of the energy deposited in nitrogen excitations. The fact that the resulting emission bands (Lyman-Birge-Hopfield, Gaydon-Herman, etc.) are observed only at very low pressures seems to imply that these states are strongly quenched, although most of these emissions lie in the ultraviolet region and are thus also lost through absorption. The Lyman-Birge-Hopfield bands result from a magnetic dipole transition with a radiative lifetime which has been measured as 1.7×10^{-4} seconds (69). If we assume a quenching cross section of 5×10^{-15} cm^2 we would then expect a pressure constant on the order of $p' \sim 0.5$ microns Hg.

The fourth positive system, another ultraviolet N_2 band system, has been observed by the author after deuteron bombardment in air at atmospheric pressure with an efficiency on the order of 0.3 photons per Mev (30). Since this system is relatively weak even at low pressure (35), it is evidently not strongly quenched in air and may have a pressure constant of about $p' \sim 30$ mm Hg, in spite of a relatively long radiative lifetime, estimated by Jeunehomme and Duncan as about 3×10^{-6} seconds (68).

The de-excitation parameters have been measured in more detail for some other band systems. Nicholls, Reeves and Bromley (36) observed a fall-off of intensity of the N_2 first positive system, which dominates the infrared emission spectrum, between 63 μ Hg and 5 mm Hg, implying $p'_{1P}(N_2) \sim 0.1 \rightarrow 1$ mm Hg,

and the results of Keck et al. (46) on the emission from shock-heated air indicate $p'_{1P}(N_2) \sim 0.3$ mm Hg. Jeunehomme and Duncan (68) observed the first positive fluorescent decay time in nitrogen as a function of pressure and vibrational quantum number, leading to the results shown below.

Table 2.7

Deactivation Parameters for First Positive System

v'	$p'_{1P,v'}(N_2)$	$\tau_{v'}$ (sec)	$\sigma_{nn}(1P,v')$ cm^2
0	.23 mm		
1	.23		
2	.12		
3	.03		
4	.036		
5	.04	10×10^{-6}	7.5×10^{-18}
6	.084	10.4	4.9
7	.037	16.9	6.8
8	.028	18.1	8.4
9	.030	18.3	7.7
10	.045	18.3	5.2
11	.058	12.0	6.2
12	.50*	8	1.1

*This anomalously high value has not yet been confirmed by other experimenters.

Calculations for v' = 0 to 4 are based on the results of Hartman (31) and Davidson and O'Neil (32). Figure 2.10 shows the variation of the pressure constant $p'_{1P}(N_2)$ with vibrational quantum number v'. There is some question as to whether the values of p' from Jeunehomme and Duncan's data truly reflect the deactivation of the state in nitrogen, since at pressures on the order of 0.1 to 1 mm Hg it may be possible for a long-lived higher level to populate the $^3\Pi_g$ level by cascading. In any case, the results of Davidson and O'Neil show that the first positive system is even more strongly quenched by oxygen, with

$$\frac{p'_{1P}(\text{Air})}{p'_{1P}(N_2)} \approx 0.06 \qquad (2.48)$$

Thus the first positive system does not contribute significantly to high pressure fluorescence, and the yield from air at atmospheric pressure within the range of sensitivity of S-11 photocathodes is less than 1% of the 2P and 1N yield (32).

The Meinel band system of N_2^+, another system in the far red, has been well studied in the course of auroral research. Sheridan, Oldenburg and Carleton (70), working in low pressure nitrogen, found a half-life for the strong (2,0) Meinel band at 7874 Å of about 3×10^{-6} seconds and a pressure constant of $p' \approx 7.7$ μ Hg, which combine to yield a collisional deactivation cross section $\sigma_{nn}(\text{Meinel}) \approx 2\times10^{-14}$ cm^2.

The Gaydon Green band system has been observed in both low pressure and high pressure nitrogen with excitation by low energy electrons (35,94). The fluorescent efficiency of the

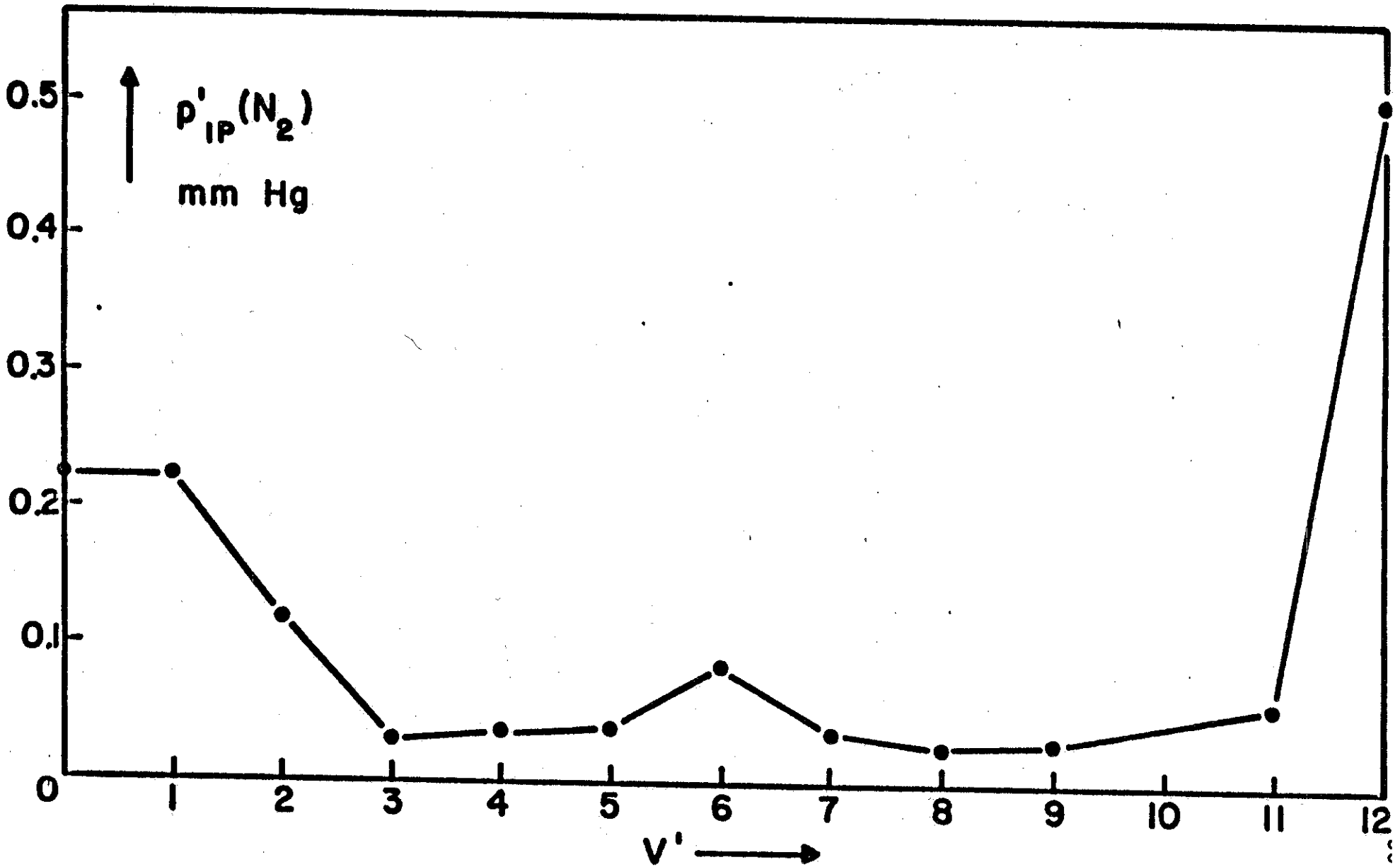

Figure 2.10 Pressure Parameters for First Positive System

strongest band, the (0,1) transition at 5815 Å, has been measured by Davidson and O'Neil (32) in 600 mm Hg nitrogen as 4.6×10^{-4}%. Anton (83) has measured the radiative lifetime for this system, finding $\tau_o = 2.86 \pm 0.3 \times 10^{-8}$ seconds, and has estimated $p'(N_2) = 150 \pm 10$ mm Hg. Accepting these values, the deactivation cross section in nitrogen is $\sigma_{nn}(GG) \approx 1 \times 10^{-16}$ cm^2. However, a small addition of oxygen is sufficient to remove all traces of these bands, and it seems likely that $p'(Air) < 1.5$ mm Hg, implying a deactivation cross section with oxygen $\sigma_{no}(GG) > 5 \times 10^{-14}$ cm^2.

The Herman Infrared band system has been observed in high pressure nitrogen by Davidson and O'Neil (32) with a fluorescent efficiency of 7.7×10^{-4}% for the (0,0) band at 8058 Å. Low pressure spectra show a comparable intensity (95), indicating very little deactivation in nitrogen. However, this band system is also not observed in air, apparently due to an efficient quenching by oxygen.

The forbidden triplet-singlet intercombination transition, $A\,{}^3\Sigma_u^+ \rightarrow X\,{}^1\Sigma_g^+$, which leads to the ultraviolet Vegard-Kaplan bands, has a radiative lifetime variously reported from 1 to 30 seconds (66,72). In very pure nitrogen these bands remain intense up to atmospheric pressure (71), indicating a deactivation cross section $\sigma_{nn}(VK) \lesssim 10^{-23}$ cm^2, but small amounts of impurities efficiently quench the state and the bands are not observed in high pressure air, and are probably even influenced by deactivation at auroral altitudes (52).

General Remarks on Quenching -

The mechanism of quenching is not well understood. In general, a strong, long-range interaction, such as that between an ion and a molecule, leads to a higher deactivation cross section than that which results from collisions between identical neutral molecules such as N_2—N_2, where the interaction is weaker and short range.

Quenching cross sections appear to be generally higher for higher vibrational excitation, although the results for the first positive system (Table 2.7) provide a notable exception. It may be that the strength of the quenching depends on an overlap integral (see page 27) of the wavefunctions of the excited molecule and the possible vibrational levels of the ground state of the target gas molecule.

Molecular oxygen is a very efficient quencher for two reasons: (i) Having an unpaired electron, the oxygen molecule has a permanent dipole moment and a triplet (S=1) ground state, unlike most diatomic molecules (34), and (ii) the oxygen molecule has many low-lying energy levels to which excitation energy may be transferred in a collision.

It is interesting to compare these measured quenching results with the predictions of gas kinetic theory. Using the tabulated "molecular radius" of 1.90×10^{-8} cm for nitrogen, gas kinetic theory indicates a value of $p'(N_2) \approx 10$ mm Hg. Therefore observed values of $p'(N_2)$ which are much larger than this, such as for the 2P, $v' = 0$ state and for the $A\ ^3\Sigma_u^+$ state in pure nitrogen, might be interpreted as due to an

effective excitation transfer mechanism, whereby a degree of excitation is transferred without radiation from molecule to molecule through successive elastic collisions, yielding a small apparent deactivation cross section.

Recombination -

It is of interest to calculate the contribution of recombination and cascading processes to the observed fluorescence at high pressure. This can be done most easily by comparing various competing reactions. First of all, the charge exchange reaction

$$N_2^+ + O_2 \longrightarrow O_2^+ + N_2 \qquad (2.49)$$

has a rate constant of 10^{-10} cm^3/sec (73) and thus dominates by at least a factor of 10^3 over other reactions in the lower atmosphere such as

$$N_2^+ + e \longrightarrow N + N^* \qquad (2.50)$$

or

$$N_2^+ + N_2 + e \longrightarrow N_2 + N_2 \qquad (2.51)$$

in the removal of N_2^+ ions. The reaction (2.49), which occurs in about 10^{-9} sec in air at atmospheric pressure, must lead to some production of the second positive system upper state $N_2(C\,^3\Pi_u)$, but the failure of Grun (33) and Bunner (30) to observe a p^2-dependent contribution to the second positive yield in air indicates that such production is less than 1% of the primary production of $N_2(C\,^3\Pi_u)$ excited states. Also, for excited N_2, the reaction

$$N_2^+ + O_2 \longrightarrow O^+ + O + N_2 \qquad (2.52)$$

becomes possible, which may have an even higher rate constant than (2.49) because of the increased phase space available to the three-body decay. The contribution of atomic oxygen lines to the air fluorescence spectrum has been measured at high pressure and is about 0.4% of the total fluorescent yield within 3000 Å → 10,000 Å (32).

Free electrons in air, after having fallen to a few electron volts, are most quickly absorbed by the electron attachment process

$$O_2 + e \longrightarrow O_2^- \qquad (2.53)$$

which has a rate constant of about 2×10^{-11} cm^3/sec (53) and thus removes electrons about 10^4 times more efficiently than reactions such as

$$e + N_2^+ \longrightarrow N_2 \qquad (2.54)$$

or

$$e + O_2^+ \longrightarrow O_2 \qquad (2.55)$$

or

$$e + N_2^+ + O_2 \longrightarrow N_2 + O_2 \,. \qquad (2.56)$$

There are no known excited states which can lead to production of the 2P system upper state N_2 ($C\,^3\Pi_u$) by cascading, nor are there any known N_2^+ states which can produce first negative, second negative, or Meinel bands by cascading. However, at very low pressures, high-lying excited states which are normally rapidly de-excited by collision may live to decay by radiation to form the $B\,^2\Sigma_u^+$ or $C\,^3\Pi_u$ states.

Evidence of such cascading has been reported for both the 1N and 2P band systems by Jeunehomme (84), who studied the decay of the fluorescence from pure nitrogen, obtaining results which could only be interpreted as a superposition of two or three different decay modes. At a pressure of 7 microns Hg, Jeunehomme found

$$\text{Yield (1N)} \propto 88\, e^{-\tau/66\text{ns}} + 15\, e^{-\tau/375\text{ns}} \qquad (2.57)$$

$$\text{Yield (2P)} \propto 100\, e^{-\tau/79\text{ns}} + 12\, e^{-\tau/1.22\,\mu\text{s}} + 10\, e^{-\tau/13.7\mu\text{s}} \qquad (2.58)$$

The shortest decays are prominent and are assumed to be the true decays of the N_2^+ ($B\ ^2\Sigma_u^+$) and N_2 ($C\ ^3\Pi_u$) states. The other decays may be interpreted as the result of cascading from long-lived higher states, possibly following recombination in the case of the 2P system.

It is well-known, on the other hand, that the N_2 first positive system is generated by cascading, and in fact every 2P radiation yields a 1P excitation. However, since $C\ ^3\Pi_u$ levels having $v' > 2$ are effectively quenched in high pressure air and since 2P transition probabilities for $\Delta v > 2$ are small, only $B\ ^3\Pi_g$ levels with small v' are produced, which lead to very long wavelength 1P emissions ($\lambda > 7000$ Å).

Thus we are justified in claiming that air is a very fast scintillator, the decay time of the fluorescence being less than 2×10^{-9} seconds at atmospheric pressure, as compared with $\sim 8\times10^{-9}$ seconds typical of plastic scintillators, or 10^{-6} to 10^{-5} seconds for activated ionic crystal scintillators.

Also, air is a very linear scintillator, the light output being linearly proportional to the energy deposited over many orders of magnitude, the final limitation being the generation of heavy concentrations of N_2^+ ions under extremely high dosage conditions, leading to re-absorption of the 3914 Å emission. This has been observed in the atmosphere following high altitude hydrogen bomb explosions, where the dosage was as high as 10^{13} N_2^+ ions per cm^3 (77).

The Effect of Argon

An enhancement of the fluorescent efficiency of nitrogen on the addition of argon has been noted by many experimenters (45,74,75) and in fact forms the basis of the inert gas scintillation counter. Since the atmosphere contains about 1% argon it is of interest to calculate the effect this has on the atmosphere as a cosmic ray scintillator.

The effect appears to be due to a high cross section for the excitation reaction

$$e + A \longrightarrow A^* \qquad (2.59)$$

followed by the excitation exchange reaction

$$A^* + N_2 \longrightarrow A + N_2^* (C\,^3\Pi_u) . \qquad (2.60)$$

Since the excited states of argon lie above the N_2 $(C\,^3\Pi_u)$ level, the nitrogen acts both as a quencher and as a wavelength shifter. Since the argon lines themselves lie far in the ultraviolet, the highest fluorescent efficiency for ordinary phototubes occurs for some mixture of argon and nitrogen.

The detailed mechanism of the excitation is complicated, probably proceeding via excitation transfer in argon - argon collisions resulting in an overpopulation of the $^3P_2$ metastable level in argon (26)

$$A^* + A \longrightarrow A + A^* (^3P_2) \qquad (2.61)$$

in which case the observed 2P yield will behave as

$$Y(2P) \sim \frac{p_A}{1+k_1 p_A + k_2 p_N} \cdot \frac{p_N}{1+k_3 p_A + k_4 p_N} \cdot \frac{1}{1+k_5 p_A + k_6 p_N} \qquad (2.62)$$

where p_A and p_N represent the partial pressures of argon and nitrogen and the k's are the various collision constants involved. Experiments on argon-nitrogen mixtures (45,74) have verified that for small argon concentrations the enhancement is small, and in the case of air, impurities further quench the exchange mechanism (75). Thus the argon contribution to the second positive emission from air is expected to be less than 1%.

Temperature Variations -

We have noted earlier that the quenching constants listed in Table 2.2 refer to laboratory conditions ($T \approx 300^\circ K$) and we have seen (equation 2.21) that the pressure constant p' varies as the root of the absolute temperature and inversely as the deactivation cross section σ, which is a function of temperature. This has two effects on the yield of atmospheric fluorescence: (a) day-to-day or seasonal variations; (b) a

variation with altitude in addition to the pressure variation. Both of these effects are worth estimating.

The temperature dependence of σ for air is not well known, but there is some evidence from deactivation measurements in other gases that it is not strong (38). Let us assume that the deactivation cross sections are independent of temperature.

Assuming a mean temperature of about 290°K, and night-to-night variations of ~ 5%, the fluorescent efficiency varies only on the order of 1%. Between summer and winter, however, the sea level temperature falls on the average 20°K and the fluorescent efficiency (optical output per unit energy loss) goes down 4%, while the fluorescent yield per unit path length goes up 4%.

To a first approximation, the temperature of the atmosphere decreases linearly with temperature (78) according to

$$T(z) = T_o - az \qquad (2.63)$$

where T_o = temperature at sea level

z = altitude in km

a = 6°K/km.

Therefore at an altitude of 10 km the temperature has dropped by 60°K; the efficiency is then lower by 11%, while the ionization rate is higher by 22%, so that the fluorescent yield per unit path length is higher by 11%.

The Transmission of the Atmosphere -

Perhaps the most serious limitation on the use of the atmosphere as a scintillator, after the low conversion efficiency of the fluorescence process itself, comes from the absorption and scattering of the light in the atmosphere. Between 3500 Å and 4500 Å the dominant effects for very clear air at sea level, in order of importance, are Rayleigh scattering, scattering by dust and water vapor, and absorption by ozone (10,76). At longer wavelengths, scattering by dust becomes the dominant attenuation mechanism. At shorter wavelengths, the small amount of ozone carried into the lower atmosphere from higher altitudes usually dominates.

A worrisome problem arises from the variability of this attenuation. Baum and Dunkelman (76) have measured the transmission of the atmosphere over long horizontal paths near sea level and have shown that Rayleigh (molecular) scattering falls far short of accounting for the total attenuation under normal conditions. It seems necessary to invoke scattering by small particles (Mie scattering) to explain the degree and variability of their measured attenuation. Since the attenuation by Mie scattering depends strongly on particle size distribution and density, day-to-day variations are not unexpected.

The extinction of a beam of light is best described by the exponential attenuation coefficient k, defined by

$$I = I_o e^{-kx} \qquad (2.64)$$

where I/I_o is the fraction of the intensity transmitted through a distance x, and the coefficient k may be considered a sum of individual coefficients for molecular scattering, particle scattering and absorption, and is of course a function of wavelength.

Figure 2.11 shows Baum and Dunkelman's results for the total attenuation coefficient k in $(km)^{-1}$ for several different days at Pasadena, California, under visibility conditions ranging from hazy to very clear, to illustrate the severe variability. The contribution of Rayleigh scattering, k_R, is drawn for 0^oC and 760 mm Hg:

$$k_R = 1.32 \times 10^{20} \frac{(n_o - 1)^2}{\lambda^4} \quad km^{-1} \qquad (2.65)$$

where λ = wavelength in Å

n_o = refractive index of standard air at 4000 Å.

It is therefore important for the calculation of absolute intensities of sources of light in the atmosphere that the attenuation be known at the time an event occurs, either by directly measuring the transmission over a fixed path at frequent intervals, or at the very least by visual estimates of visibility. Baum and Dunkelman arrived at a purely empirical approximate formula for the attenuation coefficient in terms of the visibility V used by meteorologists, valid for hazy air in the absence of pollutants such as smoke or sulphur dioxide.

$$k = \frac{5380 - \lambda}{280\ V} + \left(\frac{800}{\lambda - 1800}\right)^3 \quad km^{-1} \qquad (2.66)$$

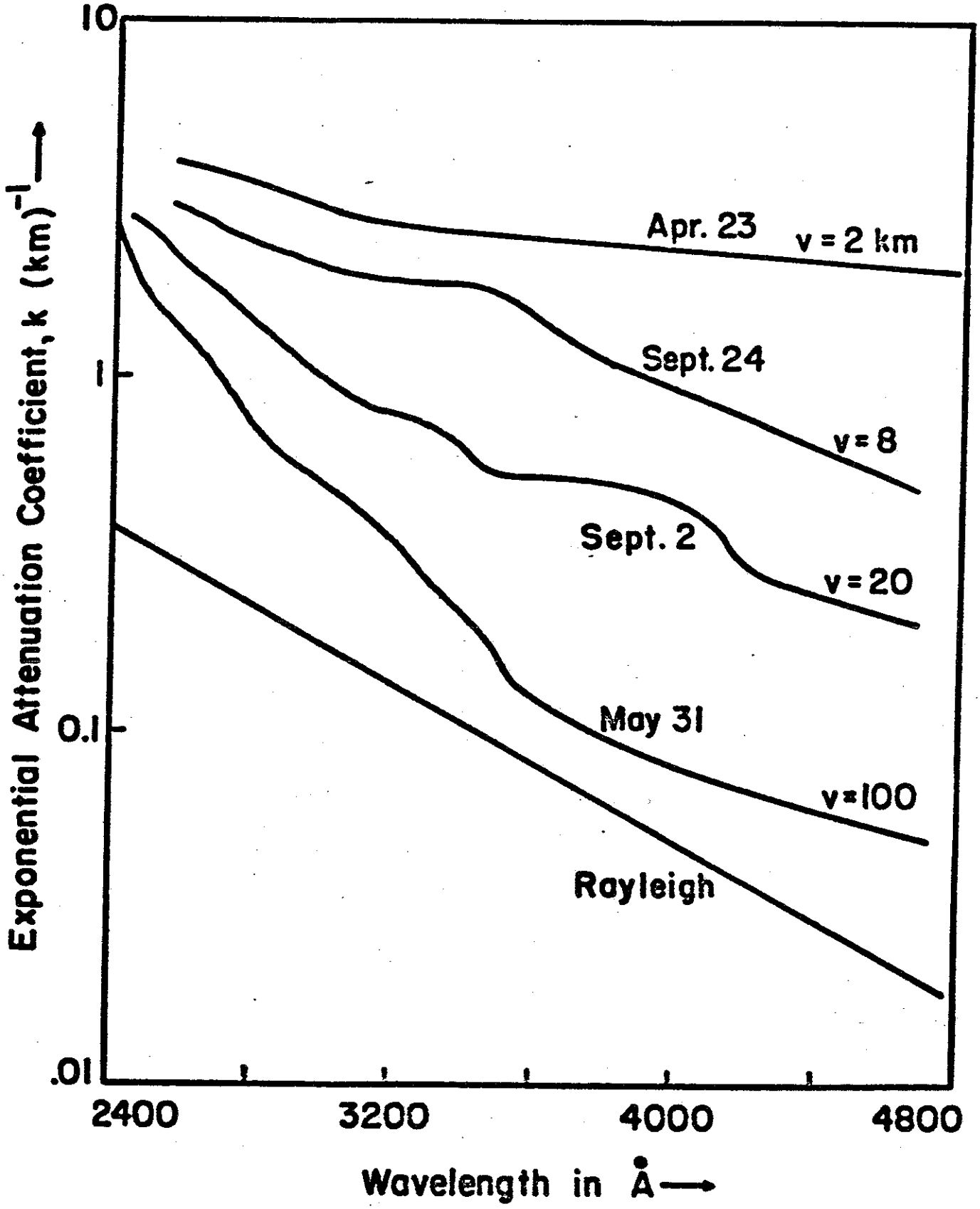
10
1
0.1
.01
Exponential Attenuation Coefficient, k (km)⁻¹
Apr. 23
v = 2 km
Sept. 24
v = 8
Sept. 2
v = 20
May 31
v = 100
Rayleigh
2400
3200
4000
4800
Wavelength in Å

Figure 2.11

where λ is in Angstroms and V is the horizontal visual range in km.

Baum and Dunkelman's results apply for the loss from a direct beam of light measured within an angle of 2 minutes of arc. However, a large fraction of the loss occurs in the form of small angle scattering so that a detector of wide angular resolution may actually receive more light than is indicated by the above discussion, with negligible time delay.

Predictions for Cosmic Ray Air Showers -

Consider a cosmic ray-generated air shower of initial total energy E_o passing down through the atmosphere at an angle ζ with the zenith. When the shower is at an altitude z above sea level the path traversed will be

$$t = \frac{1}{\cos\zeta} \int_z^\infty \rho(z)\,dz \qquad gm/cm^2 \qquad (2.67)$$

where $\rho(z)$ is the density as a function of altitude for the atmosphere in gm/cm^3. The number of secondary particles in the shower at this point we call $N(E_o,t)$. Assuming that these particles can all be considered minimum ionizing, we then have a dissipation of $q\rho(z)$ Mev/cm per particle along the shower path, where $q \approx 2.2$ Mev/(gm/cm^2) (1). Writing the conversion efficiency for the fluorescence process as $E(z)$ we then have a fluorescence yield, isotropically emitted, of

$$Y = N(E_o,t)\ q\rho(z)\ E(z) \quad Mev/cm. \qquad (2.68)$$

Taking the temperature profile of the atmosphere into account to first order, we have seen (equation 2.63) that

$$E(z) = \sum_i \frac{E(\lambda_i)}{1 + \frac{p(z)}{p_i'(T_o)}\left(1 - \frac{az}{T_o}\right)^{-1/2}} , \qquad (2.69)$$

assuming the deactivation cross sections are independent of temperature. The pressure profile can be calculated from the perfect gas law and is given by (78)

$$\ln \frac{p(z)}{p_o} = \frac{gM}{aR} \ln \left(1 - \frac{az}{T_o}\right) \qquad (2.70)$$

or,

$$p(z) = p_o \left(1 - \frac{az}{T_o}\right)^{\frac{gM}{aR}} \qquad (2.71)$$

where p_o = sea level pressure

g = acceleration of gravity

M = molecular weight of air = 29.0

R = gas constant

and for $a = 6^oK/km$, the quantity $\frac{gM}{aR} = 5.67$. Therefore $p(z) = p_o(1 - \frac{az}{T_o})^{5.67}$, accurate up to about 10 km altitude.

Therefore

$$E(z) = \sum_i \frac{E(\lambda_i)}{1 + \frac{p_o}{p_i'(T_o)}\left(1 - \frac{az}{T_o}\right)^{5.17}} \qquad (2.72)$$

and

$$\rho(z) = \frac{M\,p(z)}{R\,T(z)} = \frac{Mp_o}{RT_o}\left(1 - \frac{az}{T_o}\right)^{4.67} \qquad (2.73)$$

Finally, if we approximate $p(z) \gg p_i'$, valid below 10 km for most of the fluorescence light, we arrive at a fluorescence

yield of

$$Y = N(E_o,t)\,\frac{qM}{RT_o\left(1-\frac{az}{T_o}\right)^{1/2}}\sum_i p_i'(T_o)E(\lambda_i) \quad \text{Mev/cm}, \qquad (2.74)$$

or

$$Y = N(E_o,t)\,\frac{qM}{RT_o\left(1-\frac{az}{T_o}\right)^{1/2}}\sum_i \frac{\lambda_i}{.0124}\,p_i'(T_o)E(\lambda_i) \text{ photons/cm} \qquad (2.75)$$

for λ in Angstroms.

Table 2.8, drawn from Tables 2.2 and 2.6, presents a summary of the predicted fluorescent efficiency for high energy electrons in the lower atmosphere. These figures imply that for a wavelength range of 3400 Å to 4500 Å, for example, the total fluorescent efficiency is

$$\frac{.44}{1+p/1.0}+\frac{.092}{1+p/15}+\frac{.076}{1+p/6.5}+\frac{.027}{1+p/4.6}+\frac{.017}{1+p/2.5}\ \%, \qquad (2.76)$$

or for a wavelength range of 2800 Å to 4500 Å, the efficiency is

$$\frac{.44}{1+p/1.0}+\frac{.174}{1+p/15}+\frac{.130}{1+p/6.5}+\frac{.074}{1+p/4.6}+\frac{.062}{1+p/2.5}\ \%, \qquad (2.77)$$

with pressures measured in mm Hg.

For purposes of equation 2.74, the sum $\sum_i p_i'(T_o)E(\lambda_i) = 2.48$ for the interval 3400 Å to 4500 Å, or, $\sum_i p_i'(T_o)E(\lambda_i) = 3.52$ for 2800 Å to 4500 Å.

This is equal to 2.85 photons in the range 3400 Å to 4500 Å per meter, or 4.77 photons in the range 2800 Å to 4500 Å per

Table 2.8

Predictions for Cosmic Ray Fluorescence in Lower Atmosphere

Band	λ, Å	$E(\lambda_i)$ %	p' (mm)	Sea Level Efficiency $\times 10^{-4}$ %	Sea Level Efficiency Photons/Mev
1N 0-0	3914	.33	1.0	4.33	1.37
0-1	4278	.11		1.44	.50
0-2	4709	.020		.26	.10
0-3	5228	.003		.039	.07
2P 0-0	3371	.0820	15	15.9	4.32
0-1	3577	.0615		11.9	3.44
0-2	3805	.0213		4.12	1.27
0-3	4059	.0067		1.30	.48
0-4	4344	.0019		.37	.13
0-5	4667	.0004		.077	.03
1-0	3159	.050	6.5	4.3	1.09
1-1	3339	.0041		.35	.094
1-2	3537	.0290		2.48	.71
1-3	3756	.0271		2.31	.73
1-4	3998	.0160		1.36	.44
1-5	4270	.0035		.30	.10
1-6	4574	.0016		.14	.064
1-7	4917	.0004		.034	.014
2-0	2977	.016	4.6	.96	.23
2-1	3136	.029		1.74	.44
2-2	3309	.0020		.12	.032
2-3	3500	.0040		.24	.068
2-4	3711	.0100		.60	.18
2-5	3943	.0064		.38	.12
2-6	4201	.0046		.28	.094
2-7	4490	.0015		.09	.033
2-8	4815	.0008		.05	.02
3-0	2820	.011	2.5	.36	.08
3-1	2962	.014		.46	.11
3-2	3117	.005		.16	.04
3-3	3285	.0154		.50	.13
3-4	3469	.0063		.21	.06
3-5	3672	.0046		.15	.045
3-6	3894	.003		.10	.03
3-7	4141	.0017		.056	.02
3-8	4416	.0007		.023	.08

meter of path length, for each minimum ionizing electron near sea level. The light emission in units of photons in 3400 Å to 4500 Å per meter as a function of altitude z above sea level as calculated from equation (2.75) is shown in Figure 2.12. The positive slope of this curve is due primarily to the decrease of temperature with altitude.

We have mentioned earlier that the lateral extent of the air shower is on the order of tens to hundreds of meters for a giant shower. We thus have a diffuse source of light moving at velocity c across the sky. The time between the arrival at an observer O of the first light (from infinity) and the light from any point P (see Figure 2.13) is given by

$$t(\theta) = \frac{R}{c \sin\theta} - \frac{R}{c \tan\theta} = \frac{R}{c} \tan \frac{\theta}{2} \qquad (2.78)$$

where θ is the angle between the line of sight and the shower axis, and R is the distance of closest approach of the shower axis to the observer, or "impact parameter".

Differentiation yields

$$\frac{d\theta}{dt} = \frac{c}{R} (1 + \cos\theta) \qquad (2.79)$$

for the angular velocity of the source to an observer O, and since

$$R = r \sin\theta, \qquad (2.80)$$

the observer sees the source approaching or receding at a rate

$$\frac{dr}{dt} = -c \frac{\cos\theta}{1 - \cos\theta} \; . \qquad (2.81)$$

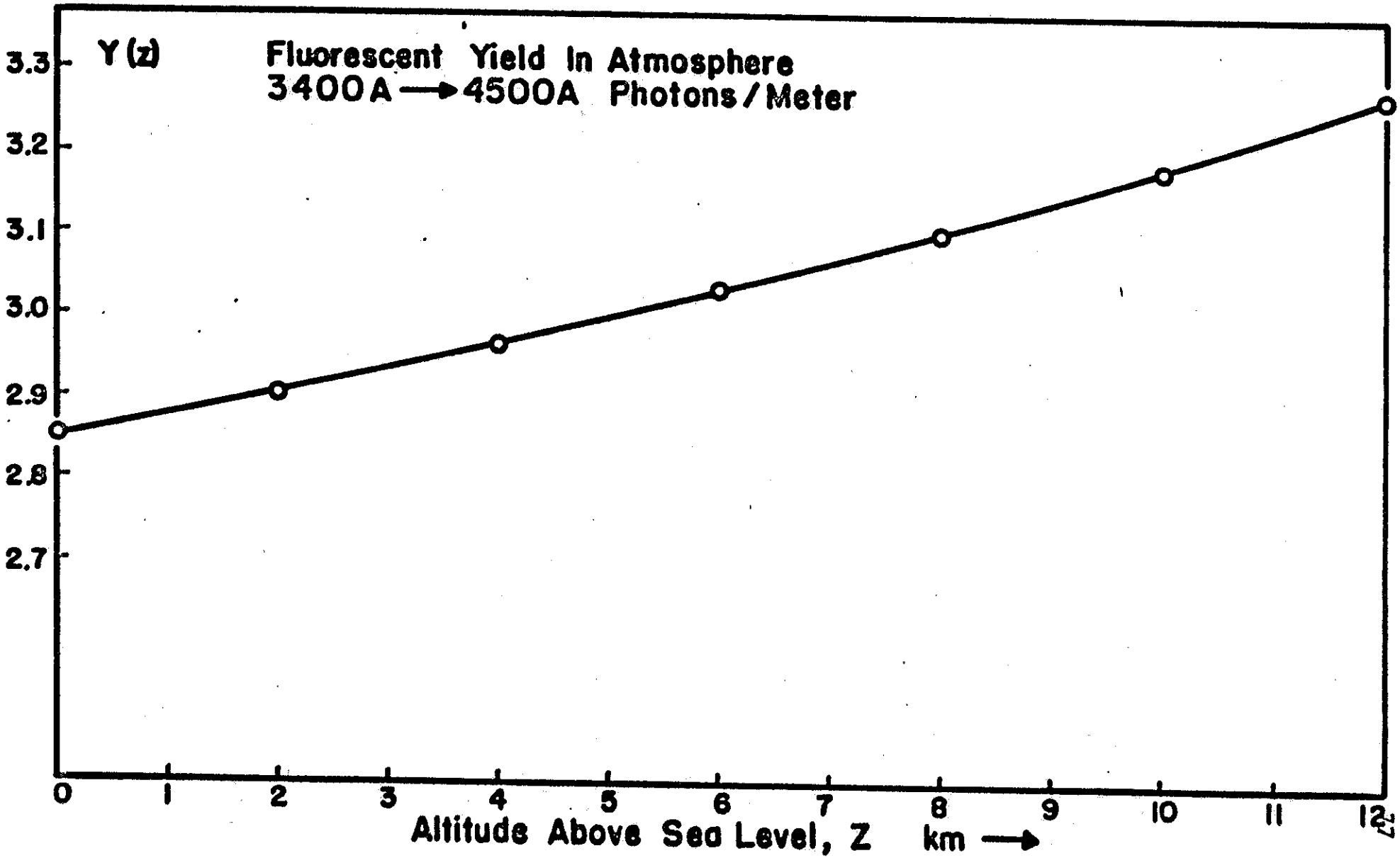
Y(z)
Fluorescent Yield In Atmosphere
3400A → 4500A Photons / Meter
3.3
3.2
3.1
3.0
2.9
2.8
2.7
0
1
2
3
4
5
6
7
8
9
10
11
12
Altitude Above Sea Level, Z km →

Figure 2.12

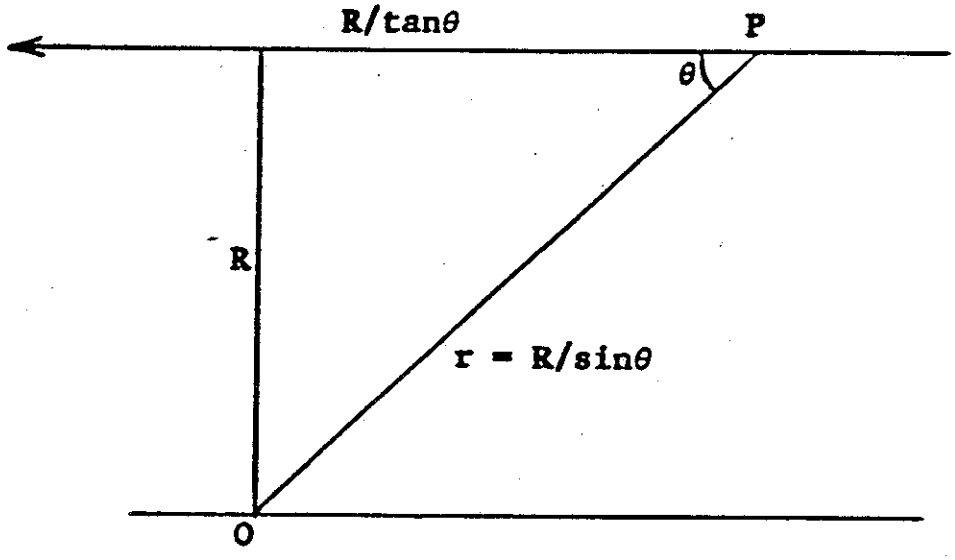

Figure 2.13

Figure 2.14 shows the time variation of $\frac{d\theta}{dt}$ and θ, where the time is shown in units of $\frac{R}{c}$ with t = 1 at closest apprcach. It is clear that for a shower approaching the observer the radiation is compressed into a shorter time span, while the radiation from a receding shower is stretched out in time. The total length of time, Δt, during which radiation is received is given by

$$c\Delta t = x + \sqrt{x^2-R^2} \qquad (2.82)$$

for a "receding" shower, one with the shower plane passing the observer before the shower arrives at ground level, where x is the distance from the observer to the point of arrival of the shower at ground level, or

$$c\Delta t = x - \sqrt{x^2-R^2} \qquad (2.83)$$

for an "approaching" shower, when the shower plane passes the observer after the shower reaches ground level, the case

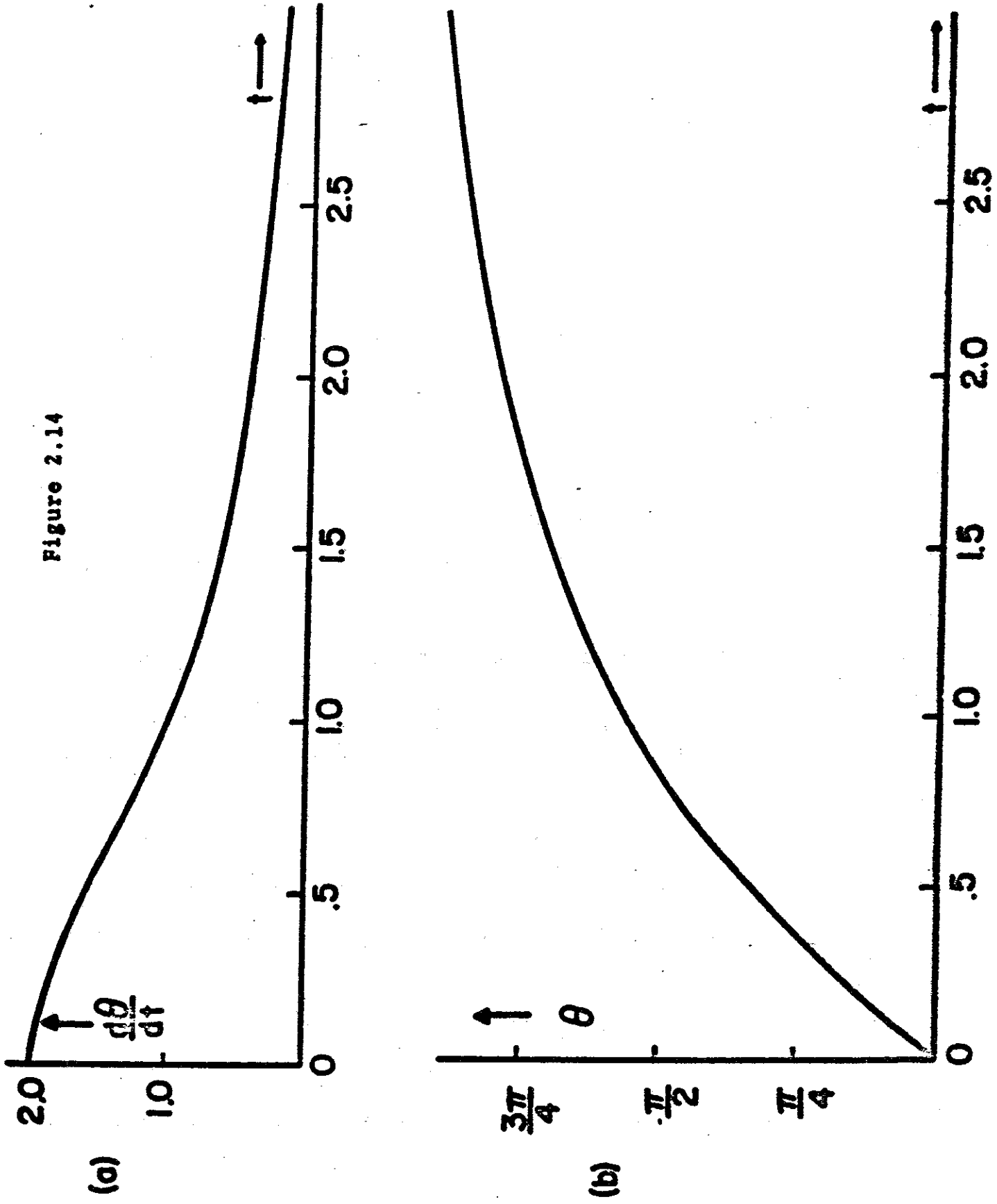
(a)
2.0
1.0
$\frac{d\theta}{dt}$
0
.5
1.0
1.5
2.0
2.5
t
(b)
$\frac{3\pi}{4}$
$\frac{\pi}{2}$
$\frac{\pi}{4}$
θ
0
.5
1.0
1.5
2.0
2.5
t

Figure 2.14

illustrated in Figure 2.15. There is, of course, no Doppler shift to the radiation itself, which is emitted by more or less stationary molecules.

In a time dt the source as seen by the observer moves $d\left(\frac{R}{\tan\theta}\right) = -R \csc^2\theta d\theta$, so that the light flux reaching the observer is

$$F(z,\theta) = \frac{Y(z) \cdot R \csc^2\theta}{4\pi r^2} \frac{d\theta}{dt} \quad \frac{\text{photons}}{\text{cm}^2 \text{ sec}} \qquad (2.84)$$

in the absence of atmospheric absorption, or making use of equation (2.64),

$$F(z,\theta) = \frac{Y(z)\ R \csc^2\theta\ e^{-kr}}{4\pi r^2} \quad \frac{d\theta}{dt} \qquad (2.85)$$

where k represents the mean free path for absorption of the fluorescence light in the atmosphere. Using equations (2.79) and (2.80), the total light received from the shower per unit time is

$$F(z,\theta) = \frac{c\ Y(z)\ (1 + \cos\theta) e^{\frac{-kR}{\sin\theta}}}{4\pi R^2} \quad \frac{\text{photons}}{\text{cm}^2 \text{ sec}} . \qquad (2.86)$$

Solving equation (2.78) for $\cos\theta$, and letting

$$\tau = \frac{c^2 t^2}{R^2} , \qquad (2.87)$$

we find

$$\cos\theta = \frac{1 - \tau}{1 + \tau} \qquad (2.88)$$

and

$$1 + \cos\theta = 2 \cos^2 \frac{\theta}{2} = \frac{2}{1+\tau} = \frac{2}{1 + \frac{c^2 t^2}{R^2}} . \qquad (2.89)$$

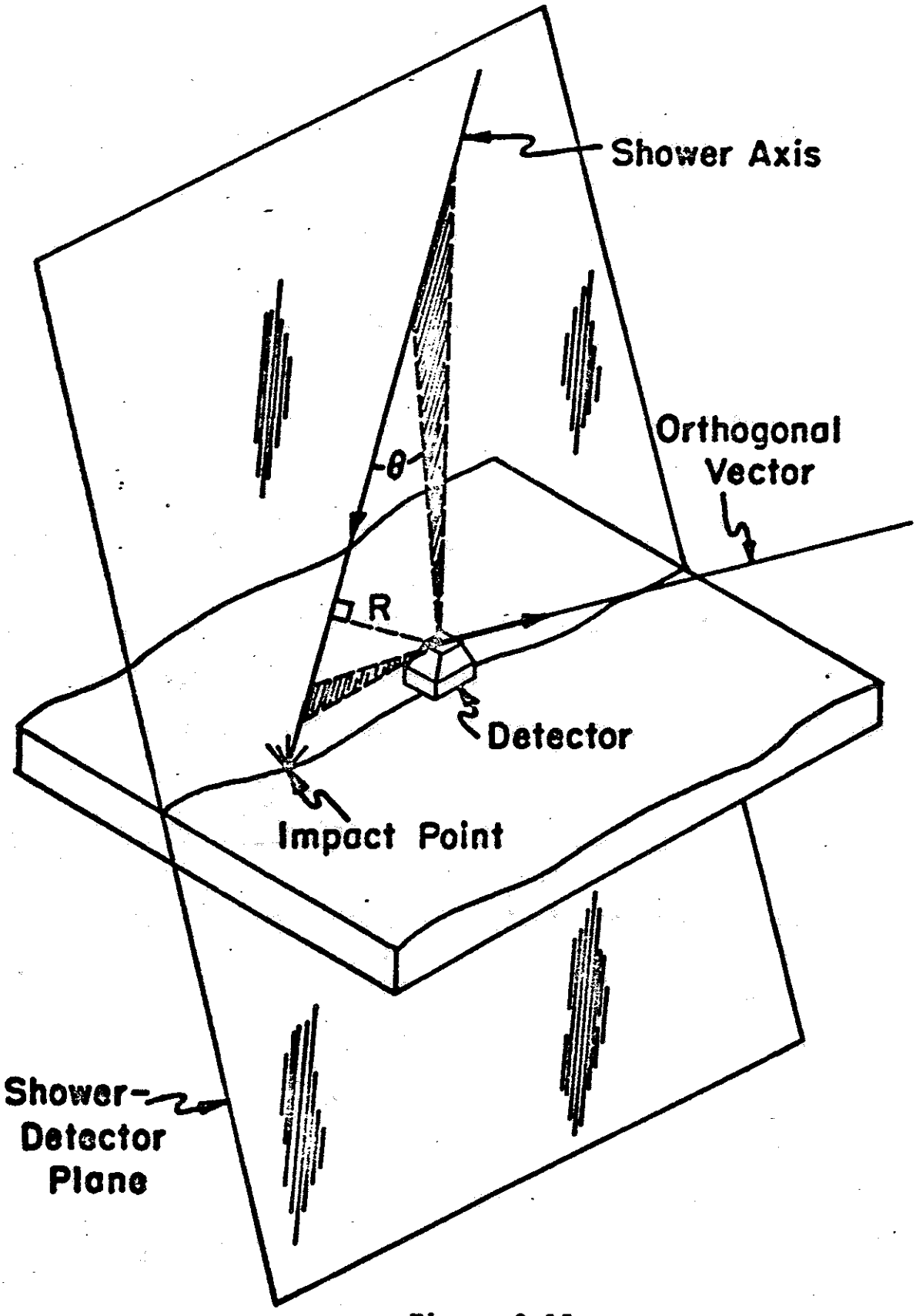
Shower Axis
θ
Orthogonal Vector
R
Detector
Impact Point
Shower-Detector Plane

Figure 2.15

Therefore, the time variation of the signal received, from (2.86), is given by

$$F(t) = \frac{cY(z)}{2\pi R^2 \left(1 + \frac{c^2t^2}{R^2}\right)} \qquad (2.90)$$

in the absence of atmospheric absorption, where the fluorescent yield Y is understood to be a function of time. Thus the expected signal pulse shapes may be visualized as a product of the shower growth curve (Figure 2.1) and the $\frac{d\theta}{dt}$ curve (Figure 2.14a), with a truncation at some value of t corresponding to impact with the ground. For "approaching" showers, this impact occurs for $\tau \leq 1$; for "receding" showers, impact occurs for $\tau > 1$.

Examples of such pulse shapes as they would be seen in the experiment to be described in the next chapters are shown in Figure 5.3.

Including the effect of atmospheric absorption, since

$$\sin\theta = \frac{2\sqrt{\tau}}{1+\tau} = \frac{2\frac{ct}{R}}{1 + \frac{c^2t^2}{R^2}} , \qquad (2.91)$$

we have

$$F(t) = \frac{cY(z)\ \exp\left[-\frac{kR^2}{2ct}\left(1 + \frac{c^2t^2}{R^2}\right)\right]}{2\pi R^2 \left(1 + \frac{c^2t^2}{R^2}\right)} . \qquad (2.92)$$

Chapter 3

DETECTION SCHEMES

The basic requirements of a detection system to utilize the fluorescence radiation are a sensitivity to very low levels of light flux, the ability to discriminate favorably towards the spectral region of the fluorescence light, the ability to trigger on a signal having the appropriate time characteristics, and the capacity to reject to some extent spurious sources of light pulses, such as generally slow-rising man-made disturbances or distant lightning flashes. The design should also provide for coverage of as much as possible of the sky and the available time to maximize the counting rate of the desired type of events.

Many schemes can be considered which satisfy these requirements in different ways. In general, for optical detectors, the limitation on the accuracy with which a very weak signal can be measured will come from the noise which results from the fluctuations in the emission of photoelectrons. For example, a photomultiplier having area A and a sensitivity leading to the arrival at the first dynode of $s(\lambda)$ photoelectrons per incident photon of wavelength λ, will respond to a flux of $F(\lambda)d\lambda$ photons/cm^2-sec with an average current of photoelectrons $\bar{I}$, given by

$$\bar{I} = e A \int_0^\infty F(\lambda)s(\lambda)d\lambda \qquad (3.1)$$

The emission of photoelectrons is a statistical effect, governed by the Poisson distribution, and therefore superimposed on the average photoelectron current will be a noise current having an RMS amplitude equal to

$$\sqrt{2e\,\bar{I}\,\Delta f} \quad , \tag{3.2}$$

where Δf is the frequency band width of the detection system (26,80). For very low levels of light flux there will also be a dark current contribution, i_d, yielding a total noise current at the first dynode of

$$\sqrt{2e(\bar{I} + \bar{I}_d)\Delta f} \quad , \tag{3.3}$$

where the dark current

$$\bar{I}_d = c\, e\, AT^2 \exp \frac{-\phi e}{kT} \tag{3.4}$$

where T is the absolute temperature, e the electronic charge, k Boltzmann's constant, and c and ϕ are characteristic of the cathode material. If in addition we assume a Poisson distribution for the number of secondary electrons from each photomultiplier dynode, each of gain k, the anode noise current is enhanced approximately by the factor $\left(\frac{k}{k-1}\right)^{1/2}$, (26), yielding an RMS current at the anode of

$$\left(2\, eg\, \Delta f \left(\frac{k}{k-1}\right)\bar{I}_a\right)^{1/2} \tag{3.5}$$

where g is the overall photomultiplier gain and $\bar{I}_a = g\bar{I}$ is the average anode current.

With these factors in mind, the signal-to-noise ratio can be predicted for a variety of optical detection schemes. For

a thorough discussion of signal-to-noise questions, the reader is referred to Lawson and Uhlenbeck (81).

Detection by Integrated Image -

It has been suggested by S. Ozaki that an air shower might be photographed in its own fluorescence light by means of a detector with high spatial resolution such as an image intensifier. This scheme has the advantage of seeing the projection of the shower on an image screen in geometrical detail, but if turned on for the entire history of the event, will integrate the background light at every point over a time longer than the image takes to pass that point. If the resolution of the system is $\Delta\omega$ steradians and if the source is β radians wide as seen by the detector, ($\Delta\omega < \beta^2$), then the signal light collected in a small area is proportional to the flux of source photons emitted within the resolved region $\Delta\omega$ times the time the source takes to pass through this region. Also, if an air shower has a diameter b, assumed constant,

$$b = \beta r = \frac{\beta R}{\sin\theta}$$

and therefore the apparent angular size of the source, β, is

$$\beta = \frac{b}{R} \sin\theta \,, \qquad (3.6)$$

then, from (2.75) and (2.81),

$$\text{Signal} \propto \frac{Y(1 + \cos\theta)}{R^2} \frac{\Delta\omega}{\beta(d\theta/dt)}$$

$$\propto \frac{Y(1 + \cos\theta)}{R^2} \cdot \frac{\Delta\omega}{\beta(1 + \cos\theta)} = \frac{Y\Delta\omega \csc\theta}{b} \qquad (3.7)$$

independent of R, apart from the effect of atmospheric absorption. The $\csc\theta$ factor is the familiar limb brightening of optically thin sources.

The shower history has a typical duration, from (2.82), of $\Delta t \approx \frac{R}{c}$. If the integrating time of the detector is fixed so as to compose images over a time comparable with the duration of the most distant events expected, $(\Delta t)_{max} \approx \frac{R_{max}}{c}$, and during this time the light received from a background flux of B photons/cm^2-ster-sec is proportional to

$$B\ \Delta\omega\ (\Delta t)_{max} \approx \frac{B\ R_{max}\ \Delta\omega}{c} \qquad (3.8)$$

Therefore the signal-to-background ratio in this case behaves as

$$S/B \propto \frac{Y}{B\ R\ R_{max}\ \beta} = \frac{2Y}{B\ b\ R_{max}\ \sin 2\theta} \quad , \qquad (3.9)$$

provided the resolution is finer than the image size.

If the resolution is not high enough to resolve the angular width of the source, but is less than the angular length of a shower, the light collected is proportional to $\frac{Y}{R}\sqrt{\Delta\omega}$, and

$$S/B \propto \frac{Y}{B\ R\ R_{max}\ \sqrt{\Delta\omega}} \quad . \qquad (3.10)$$

However, the imaging technique offers the advantage of displaying a pattern in the recorded signal. Let us accept, as a rule of thumb, that the readability or quality, Q, of the picture as a whole is proportional to $\overline{S/B}\ \sqrt{n}$, where n is the number of independently resolved areas along the track and $\overline{S/B}$

is the average signal-to-background ratio. The angular extent of the complete trail of light, from Figure 5.1, ignoring the finite thickness of the atmosphere, is

$$\Delta\phi \simeq \pi - \sin^{-1}\left(\frac{R}{x}\right) = \pi - \psi ,$$

where ψ is the angle between the line from the observer to the impact point and the shower axis. The number of resolvable cells along the complete shower path is then given by

$$n = \frac{\pi - \psi}{\sqrt{\Delta\omega}} . \qquad (3.11)$$

Therefore

$$Q \propto \frac{Y\,(\pi - \psi)^{1/2}}{B\,b\,R_{max}\,(\Delta\omega)^{1/4}} \qquad (3.12)$$

for the resolved image case, or

$$Q \propto \frac{Y\,(\pi - \psi)^{1/2}}{B\,R\,R_{max}\,(\Delta\omega)^{3/4}} \qquad (3.13)$$

for an unresolved image.

A basic disadvantage of a system lacking time resolution is the difficulty of imposing a satisfactory triggering requirement. No decision can be made on whether to record the information collected in a time interval T except on the basis of the total light received in that time; in other words, it is difficult to take advantage of the spatial resolution for triggering purposes. One solution might be to integrate blindly over successive fixed intervals T, where T is roughly equal to duration of the longest expected shower event, recording the picture only if some external triggering condition is met.

However, in this case the probability of recording at least 3/4 of an event of duration T arriving at a random time is only about 60%, and the probability of recording a truncated event, which may lead to error in geometrical analysis, is high.

Wide Angle System -

A system may also be considered which is the exact opposite to the integrated image system, namely, one which resolves the event in time but not in space. Such a method might be, for example, to monitor the entire night sky with a single photomultiplier which is prepared to record a signal current as a detailed function of time. In this case we obtain a set of signal measurements made against a background of noise due to fluctuations in the photoelectron current, measured over the relatively short time $1/\Delta f$ (the response time of the photomultiplier system).

If i_s is the signal current, understood to be a function of time, and i_b is the current due to the background night sky light plus dark current, then, from equation (3.2), the signal-to-noise ratio is

$$S/N = \frac{i_s}{\sqrt{2e(I_s+I_b)\Delta f}} \quad , \qquad (3.14)$$

which may be limited by the background or by the signal itself, whichever is larger. Assuming the system sees the entire event, the number of independent readings which may be

made is approximately

$$\left(\frac{R}{c}\right)\Big/\left(\frac{1}{\Delta f}\right) \quad , \tag{3.15}$$

and therefore the readability factor is

$$Q = i_s \sqrt{\frac{R}{2ec(\bar{I}_s + \bar{I}_b)}} \quad , \tag{3.16}$$

independent of the detector bandwidth, provided Δf is large enough to follow the changes in the signal $i_s(t)$.

Ignoring dark current, the background current is given by

$$\bar{I}_b = e\, A\, \Delta\omega \int_0^\infty B(\lambda)s(\lambda)d\lambda \tag{3.17}$$

where $B(\lambda)d\lambda$ is the flux of night sky light photons of wavelength λ per cm^2-steradian-second, A is again the area receiving photons, and $\Delta\omega$ is the effective solid angle of acceptance of the system. Both S/N and Q are proportional to $(A)^{1/2}$. It is clear that it is important to maximize the ratio

$$\frac{\int_0^\infty F(\lambda)s(\lambda)d\lambda}{\left(\int_0^\infty B(\lambda)s(\lambda)d\lambda\right)^{1/2}} \quad ,$$

or in other words to match the spectral response of the detector to the source spectrum. This might be accomplished for example by narrow band filters which admit the relatively narrow spectral bands produced by molecular fluorescence.

A wide angle system utilizing interference filters has been proposed by Hoerlin and Westervelt (77) for the detection of atmospheric fluorescence produced by the X-rays from nuclear explosions in space. Since an entire hemisphere of the earth's

atmosphere may be illuminated by X-rays, there is no requirement for spatial resolution. However, the use of narrow band interference filters centered at the very narrow and very efficient 3914 Å band makes it possible to obtain a reasonable S/N ratio over the duration of the event even under daylight background conditions. In our case, however, the use of collimating lenses would so reduce the effective light collecting area that there would be no net gain in S/N.

Spatial Plus Temporal Resolution -

There are several ways in which time resolution and spatial resolution can be combined to yield more information. Perhaps the most obvious schemes would be either to cover the sky with $\frac{2\pi}{\Delta\omega}$ time dependent signal detectors, where $\Delta\omega$ is the finest angular resolution desired, or to produce an imaging system which could collect enough light to record a picture every Δt seconds, where Δt is the finest time resolution desired. However, both are clearly prohibitively expensive and the latter not only would require an aperture for light collection larger than seems feasible, but also suffers from the aforementioned triggering difficulty.

A compromise with good time resolution but only partial space resolution would be effected with a limited number of wide angle detectors, each viewing a sector $\Delta\omega$ of the sky and recording the light signal as a function of time. This is the basic scheme proposed by K. Greisen in 1962 for the Cornell University air scintillation detection experiment

discussed in detail in the following chapter. We assume such a system is background noise limited. Then we have a signal in each channel, from equation (2.86) corresponding to the number

$$\frac{c(1+\cos\theta)}{4\pi R^2} A \cos\phi \, \Delta t \int_0^\infty Y(\lambda)s(\lambda)d\lambda \quad \text{photoelectrons} \tag{3.18}$$

in a small time Δt, where $A \cos\phi$ is the effective area of a detector receiving light at an angle of incidence ϕ, and atmospheric attenuation is for the moment ignored.

The background photocurrent collected in the same time is $A \, \Delta\omega \, \Delta t \int_0^\infty B(\lambda)s(\lambda)d\lambda$. We may abbreviate our notation with the following definitions:

Let

$$\int_0^\infty Y(\lambda)s(\lambda)d\lambda = \Lambda_s \, Y(\lambda_o)s(\lambda_o) \tag{3.19}$$

$$\int_0^\infty B(\lambda)s(\lambda)d\lambda = \Lambda_b \, B(\lambda_o)s(\lambda_o) \tag{3.20}$$

where Λ_s and Λ_b represent the equivalent optical bandwidths (in units of wavelength) of the signal light spectrum and the background spectrum respectively, $s(\lambda)$ is considered to be the overall sensitivity of the optical system in photoelectrons per incident photon, including the transmission of optical filters, and λ_o is the wavelength where $s(\lambda)$ is a maximum.

Then the signal-to-noise ratio for each channel, a function of time, is given by

$$S/N = \frac{(1+\cos\theta)}{4\pi R^2} \cos\phi \Lambda_s Y(\lambda_o) \sqrt{\frac{A s(\lambda_o) \Delta t}{\Lambda_b B(\lambda_o) \Delta\omega}} . \qquad (3.21)$$

This illustrates the advantage in making Δt sufficiently long to effectively smooth out the noise, provided Δt is not longer than the time in which $Y(1+\cos\theta)$ changes significantly.

The night sky brightness $B(\lambda)$ for clear air in photons/cm^2-sec-ster-Å is tabled below (10):

Table 3.1

λ(Å)	3200	3600	4000	4500	5000	5500
$B(\lambda)$	2.3×10^4	2.0×10^4	2.6×10^4	4.5×10^4	5.0×10^4	8.3×10^4

This is a relatively flat spectrum and for an S-11 photocathode with no optical filter corresponds to an equivalent optical bandwidth of about $\Lambda_b = 3000$ Å. (By comparison, the equivalent optical bandwidth of the sea level air scintillation spectrum, which consists of bands typically 10 Å wide, with an S-11 photocathode, has been calculated and is $\Lambda_s \approx 40$ Å.)

The total number of independent signal measurements is approximately $\frac{R\Delta f}{c\pi}$, which may be spread, with some overlapping, over several channels.

The closest spacing at which uncorrelated readings may be made, and thus the most information extracted, is here considered to be $\Delta t = 1/\pi\Delta f$. This is an approximation since the output of a detector of bandwidth Δf at any instant t_o is

an exponentially weighted average of the signal received over all past time, the weighting function decaying away in past time as

$$e^{-2\pi(t_o-t)\Delta f} \quad . \tag{3.22}$$

Accepting $\Delta t = 1/\pi\Delta f$, the figure of merit for the overall event becomes

$$Q = \frac{(1+\cos\theta)}{4\pi R^{3/2}} \cos\phi \quad \Lambda_s \, Y(\lambda_o)\sqrt{\frac{A\, s(\lambda_o)}{c\,\Lambda_b B(\lambda_o)\Delta\omega}} \quad . \tag{3.23}$$

This quantity is calculated for the specific conditions of the Cornell University air scintillation detector in Chapter 5.

Leaning in the opposite direction, a design can be considered with good spatial resolution but limited time resolution, which is signal noise limited. Such a design could be a mosaic of small phototubes which cover the sky with an angular resolution as fine, say, as a typical air shower width (about one degree at $r \approx 10$ km) and within which a linear sequence of delta function pulses records the passage of a shower through the sky.

If the signal exceeds the background light collected and the time of passage of the light source through the angular aperture $\Delta\omega$ of an individual channel is longer than $1/\Delta f$, then from equations (3.14) and (3.18), for each channel,

$$S/N = \left(\frac{c(1+\cos\theta)A\,\Lambda_s Y(\lambda_o)s(\lambda_o)}{8\pi R^2\,\Delta f}\right)^{1/2} , \tag{3.24}$$

as usual increasing with the square root of the collection area A, and

$$Q \approx \left(\frac{(1 + \cos\theta) A \Lambda_s Y(\lambda_o) s(\lambda_o)}{8\pi R} \right)^{1/2} , \qquad (3.25)$$

independent of both Δf and $\Delta\omega$ under the above assumptions.

The relative merit of these two suggested "compromise" schemes depends on the particular values of many parameters, but it is clear that the narrow angle system reduces the noise to a minimum in each channel by reducing the area of the sky that each channel sees without reducing the signal strength, provided the resolution is not finer than the source width. A potential danger in this design is that the number of photoelectrons produced in each channel by the light signal may be too small for a statistically significant result, or in other words, that the signal noise limitation itself may be severe. However, this limitation is no more severe here than in the scheme previously discussed if the effective collecting area A is kept large, for example by the use of lens optics.

This scheme is now being developed at Cornell University using 18-inch diameter Fresnel lenses and 2-inch photomultiplier tubes, each of which observes $\Delta\omega = .01$ steradian. It should be noted that the lenses in a design of this type do not need to be of high quality, since the incident light need be focused only into discrete cells of angular size $\Delta\omega$.

Optical Filters -

We have discussed the advantage of matching the spectral response of the detector to the air fluorescence spectrum for optimizing the signal-to-noise ratio. If a particular

photocathode must be chosen for other reasons such as cost or availability it is still possible to optimize S/N by the use of optical filters, matching the filter transmission to the product of the cathode sensitivity function and the fluorescence spectrum. In general, a narrow band (interference) filter is to be preferred if the expected photon flux in one emission band is great enough to produce good photon statistics and if the maximum angle of incidence can be kept small. Interference filters are available, both of the transmission and reflection variety, with bandwidths as narrow as a few angstroms at normal incidence.

Roughly speaking, the bandwidth $\Delta\lambda$ of an interference filter to light incident with an angular spread of $\Delta\theta$ is limited by

$$\Delta\lambda \gtrsim \lambda_o(1 - \cos\frac{\Delta\theta}{2}) , \qquad (3.26)$$

so that, for example, a design requiring a bandwidth of 20 Å near 4000 Å can collect light with an effective aperture no greater than 0.03 steradians. Therefore the use of interference filters severely restricts the light gathering power of a detector. On the other hand, a chemical absorption filter can be used, having a passband typically several hundred or several thousand angstroms wide which decreases with increasing angle of incidence, in contrast to an interference filter.

In the Cornell wide angle system the choice of an S-11 photocathode was dictated by its availability in a large area ($A = 1060$ cm^2) and the use of interference filters was precluded

for both of the reasons mentioned in the preceding paragraph. A chemical absorption filter was then found, Corning Glass No. 5970, which could be manufactured in a convenient size and which decreased the equivalent optical bandwidth of the night sky spectrum (equation 3.20) from 3000 Å to 590 Å while only changing the equivalent bandwidth of the sea level air scintillation spectrum from 40 Å to 24 Å, thus enhancing the signal-to-noise ratio by about 1.35, as well as greatly reducing the additional background of artificial light produced by filament lamps which is strongest to the red of the filter passband. The response of this filter is discussed further in Chapter 4.

Clearly, in a highly resolved system such as we discussed in the last section, the use of optical filters is unnecessary if S/N is truly limited by the signal noise itself.

It is interesting to note from the results of Chapter 2 that if the fluorescence light flux were great enough to allow the use of narrow band interference filters with statistically accurate results, an additional dimension could be added to the information extracted from an event by simultaneously recording two wavelengths resulting from transitions having different p' parameters, such as the strong 3914 Å 1N(0,0) and 3577 Å 2P(0,1) bands. However this technique would only be of value in determining altitudes above 8 km, early in the shower history, and it is unlikely that any feasible means can be found for collecting a sufficient flux of photons from this early in an air shower.

Cerenkov Light Contribution -

It has been shown (85) that cosmic ray air showers produce Cerenkov light with an efficiency comparable to that of the air fluorescence. The intensity and spectral composition of the Cerenkov emission are given as a function of frequency ν by

$$Y_c(\nu)d\nu = \frac{2\pi\alpha N}{c}\left(1 - \frac{1}{\beta^2 n^2}\right)d\nu \quad \text{photons in } (\nu,\nu+d\nu)/\text{cm} \qquad (3.24)$$

where α = fine structure constant = 1/137

N = number of secondary particles in the shower

β = secondary particle velocity

n = index of refraction of air.

In an air shower the secondary particles have a range of values for β. Writing $N(E)dE$ for the number of particles in the energy range $(E, E+dE)$ and noting

$$1 - \frac{1}{\beta^2 n^2} \approx 1 - \left(\frac{E_T}{E}\right)^2 , \qquad (3.25)$$

where E_T = Cerenkov threshold energy, = 21 Mev at sea level, we have

$$Y_c(\nu)d\nu = \frac{2\pi\alpha}{c}\int_{E_T}^{\infty} N(E)\left[1 - \left(\frac{E_T}{E}\right)^2\right]dE\,d\nu \quad \frac{\text{photons in } (\nu,\ \nu+d\nu)}{\text{cm}} . \qquad (3.26)$$

The Cerenkov light is intense only along the shower axis, owing to the fact that the emission occurs at an angle $\cos^{-1}\frac{1}{\beta n}$ to the path of the radiating particle, where β and n are both very close to 1. For impact parameters greater than 2 km, even for the largest air showers, the only Cerenkov light seen

by an observer is that produced by widely scattered electrons, and the fluorescence radiation dominates. Moreover, the Cerenkov radiation near the axis arrives with the shower front in a very short time, typically less than 1/10 microsecond, and therefore can hardly present confusion with the pulses from fluorescent light, which are sought with widths of typically 10 to 40 microseconds. The analysis of the Cerenkov contribution to showers is discussed in more detail in Chapter 5.

As far as the relative merit in utilizing the fluorescence light for the study of air showers is concerned, although considerable success has come from experiments observing the Cerenkov emission (86,87,88), the isotropic property makes the fluorescence radiation visible from as far away as atmospheric transmission and the inverse square law allow, and even visible from receding showers. Furthermore, the time structure of the fluorescent radiation yields important information concerning the history of the shower which is absent in the Cerenkov radiation.

Chapter 4

THE CORNELL WIDE ANGLE SYSTEM

While an initial study of the efficiency and spectral distribution of air fluorescence was being carried out by the author (30), plans were made by K. Greisen and S. Ozaki for a wide angle time dependent detector that would satisfy the requirements that are discussed in Chapter 3.

The purpose of this detector was to serve as a pilot device for a study of the feasibility of detecting air showers by the fluorescence technique, with the view in mind of applying the method on a larger scale at a better location if the scheme should prove fruitful.

During the first part of 1964 a first detector station was constructed and put into operation by S. Ozaki and the author. Later in 1964 Dr. G. Tanahashi joined the experiment and supervised the construction of a second and third detector which began operation during 1965 and 1966. During this time Mr. E. Jenkins pursued a computer study of the simulation of cosmic ray air showers and the techniques of data analysis as applied to these detectors.

Optical Design Considerations -

In order to calculate the direction of a light source at any instant of time from the signals received, a minimum of four phototubes pointing in different directions to cover the

sky (for example in a tetrahedron arrangement) are necessary. Furthermore, it is necessary that the response of the detector as a function of angle of incidence be a monatonic function with non-vanishing derivative, in order that there be a unique solution for the direction of the light source from the ratio of the signals received in two channels. (For example a set of detectors which respond equally to light from all directions would yield no information concerning the location of the source.) A flat photosurface which presents an effective area A $\cos\phi$, where ϕ is the angle of incidence, satisfies this condition.

However, to introduce an element of redundancy, to provide a more Cartesian set of pointing directions and to place less emphasis on the response of the detectors at large angles of incidence, a five-channel system with flat-surfaced detectors was chosen with photomultipliers in a hexahedron arrangement pointing north, south, east, west and upwards. The four horizontal tubes were tilted upwards 30^{o} to avoid pointing uselessly below the horizon and also to reduce again the dependence on the detector sensitivity at large angles of incidence. This geometry is shown in Figure 4.1. The net result is a system in which different parts of the sky are viewed by 5, 4, 3 or 2 tubes, where measurements from 3 channels are necessary to fix any point source in the sky. Figure 4.2 shows a schematic map of the sky in a polar projection representation with letters illustrating the channels which view each sector, drawing the borders of a sector where the

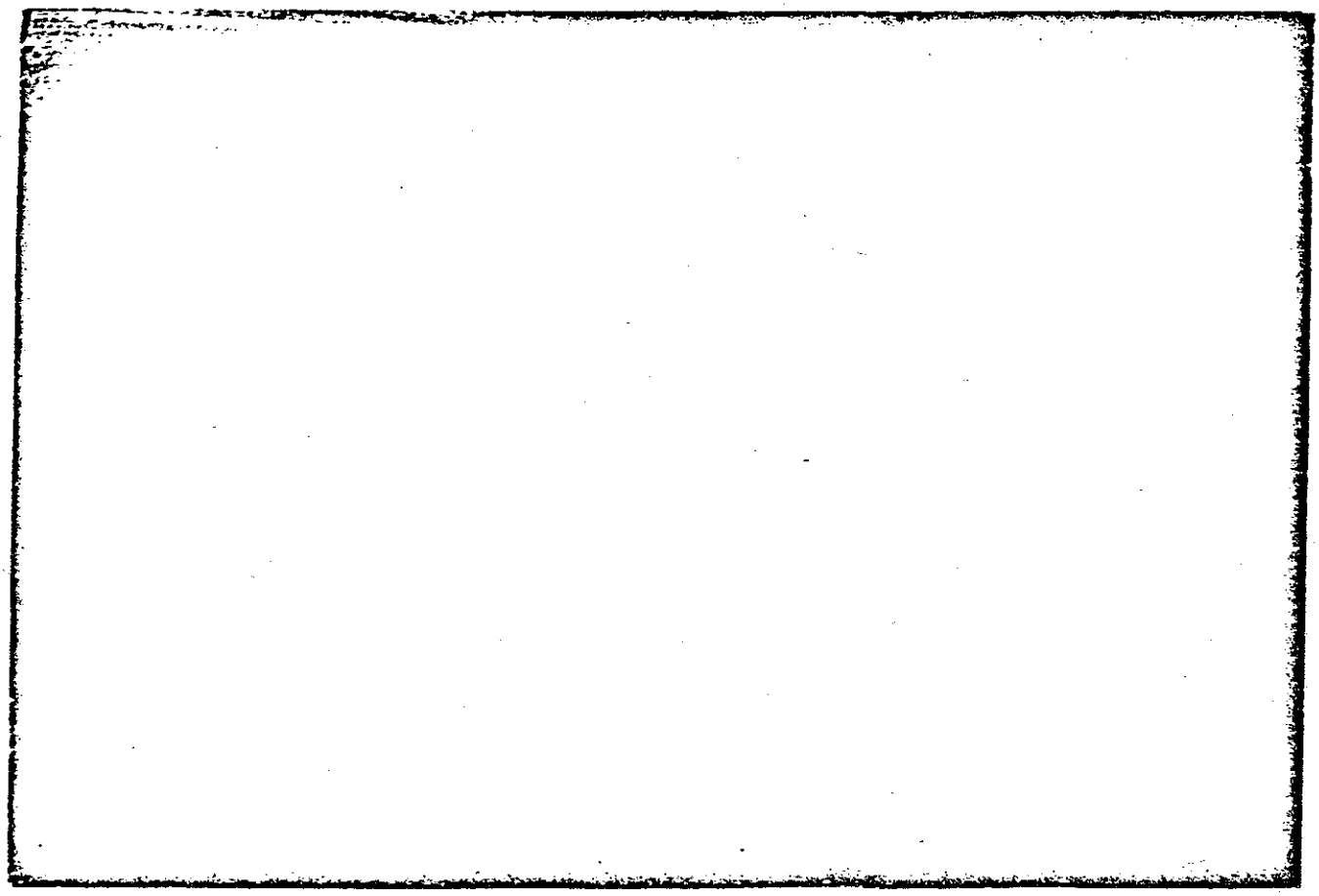

Figure 4.1 One of the Field Stations of the 5 Tube Array Near Ithaca

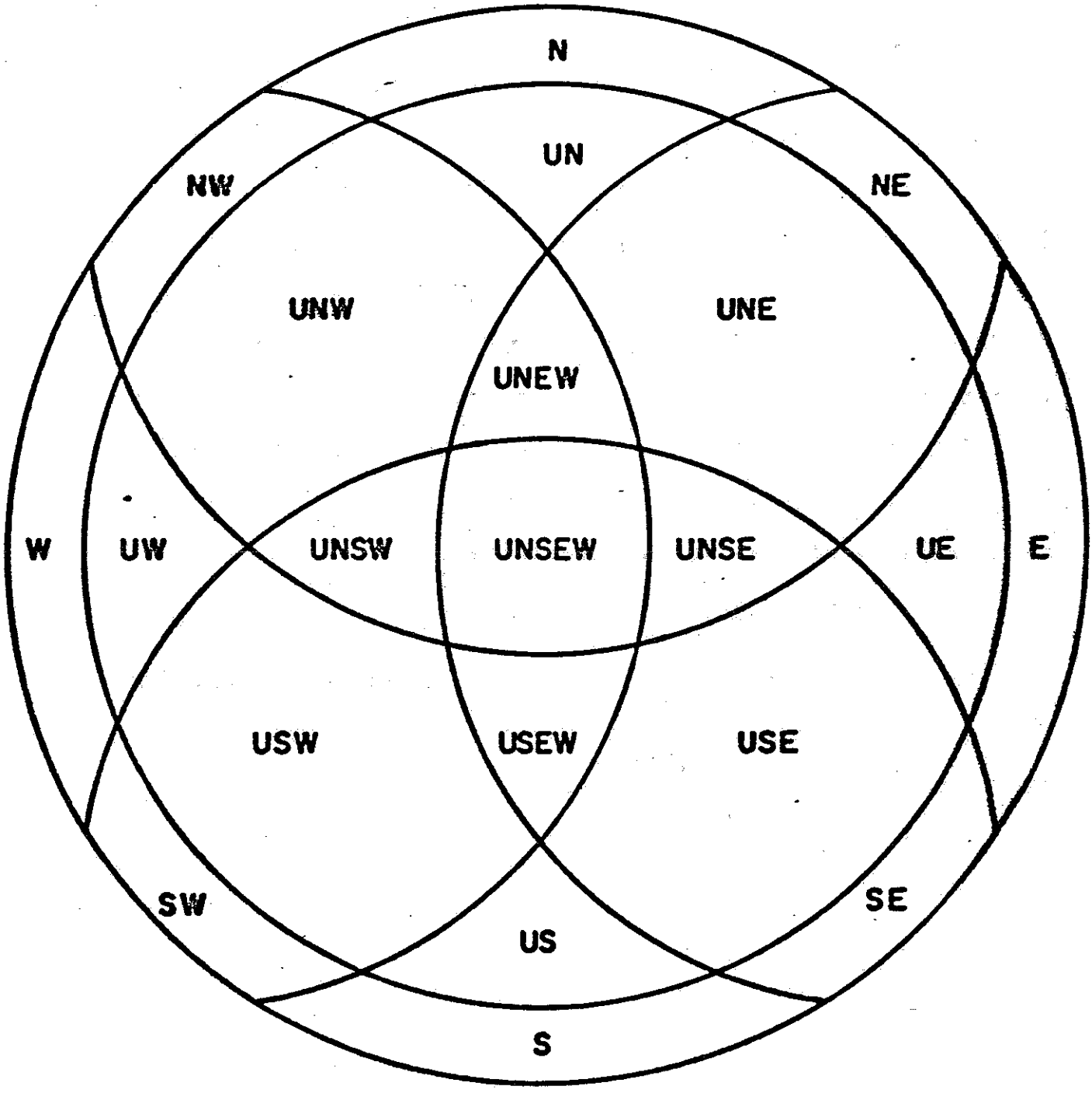
N
NW
NE
UN
UNW
UNE
UNEW
W
UW
UNSW
UNSEW
UNSE
UE
E
USW
USEW
USE
SW
SE
US
S

Figure 4.2

sensitivity of a detector falls to 10% of normal incidence sensitivity.

On the Use of Lenses -

Consideration was given to the suggestion that hemispherical condensing lenses of large size be mounted directly in front of each photocathode. This "immersion lens" system has the obvious advantage of increasing the effective area of the detector without reducing its angular field of view. If the lens has a radius r and index of refraction 1.5 and a photomultiplier of diameter r is placed immediately behind the center of the lens, as shown in Figure 4.3, then the effective area of the detector to light incident at an angle ϕ to the axis is approximately

$$A(\phi) = \frac{\pi r^2}{4} (1 + \cos\phi) \cos\phi \qquad (4.1)$$

The area of lens presented to the source is approximately $\frac{\pi r^2}{4} (1 + \cos\phi)$, and the efficiency of focussing the light on the photocathode is approximately $\cos\phi$.

Since the effective area of the phototube alone is $\frac{\pi r^2}{4} \cos\phi$, the gain is

$$\frac{\frac{\pi r^2}{4} (1 + \cos\phi) \cos\phi}{\frac{\pi r^2}{4} \cos\phi} = (1 + \cos\phi) \qquad (4.2)$$

and the increase in S/N ratio is $\sqrt{1+\cos\phi}$, on the average about a 30% improvement. For r(lens) << r(tube) the improvement in light collection is simply n^2 for normal incidence,

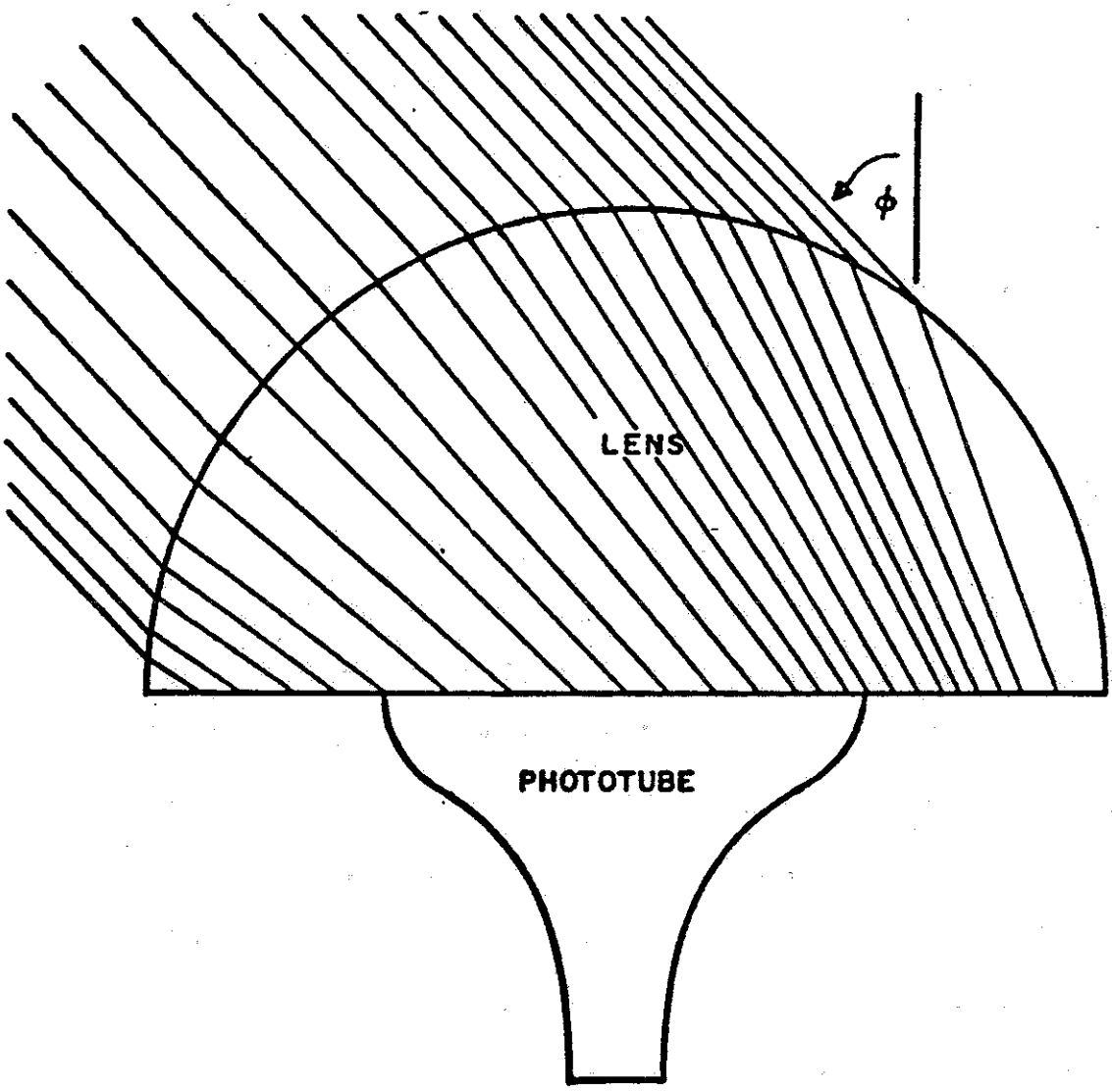

Figure 4.3 Geometry of Hemispherical Lens

which is never much better than a factor of two for ordinary materials, the same factor gained by doubling the phototube area. For large phototubes, increasing the tube size is the cheaper alternative. Moreover, such a lens, used in conjunction with a large photomultiplier, implies a long path length for radiation to reach the photocathode through the lens material. Since the signal light is in the near ultraviolet region, absorption losses partly cancel the geometrical improvement factor. Hence this idea was abandoned for the fluorescence detection experiment.

Wavelength Shifters -

Another suggestion studied for the improvement of signal-to-noise ratio in a wide angle system was to apply a fluorescent chemical* known as a "wavelength shifter" and trap the re-emitted light by internal reflection in an optical system that channels incoming light collected over a large are to a comparatively small photocathode area.

A fundamental theorem of statistical mechanics, known as Liouville's theorem, is frequently applied to optics to show that the product (solid angle) x (effective area) for light entering an optical system can be no greater than the same product for the light leaving the optical system. This

---

*We are here using the term "fluorescent" in its proper sense, signifying the property of absorbing light of one wavelength and emitting light of a longer wavelength.

implies, for example, that there is no optical arrangement that allows the area of a light sensor to be reduced without at the same time reducing the volume of sky viewed by the sensor.

The use of a wavelength shifter offers in principle an escape from this restriction. Liouville's theorem applies only to situations where the mapping between source and image is conformal, such as in geometrical optics with lenses and mirrors. However, the direction of light emitted in the fluorescence process is independent of the incident light and is, in fact, isotropic. Hence a detection system can be envisioned, such as that illustrated below, in which light

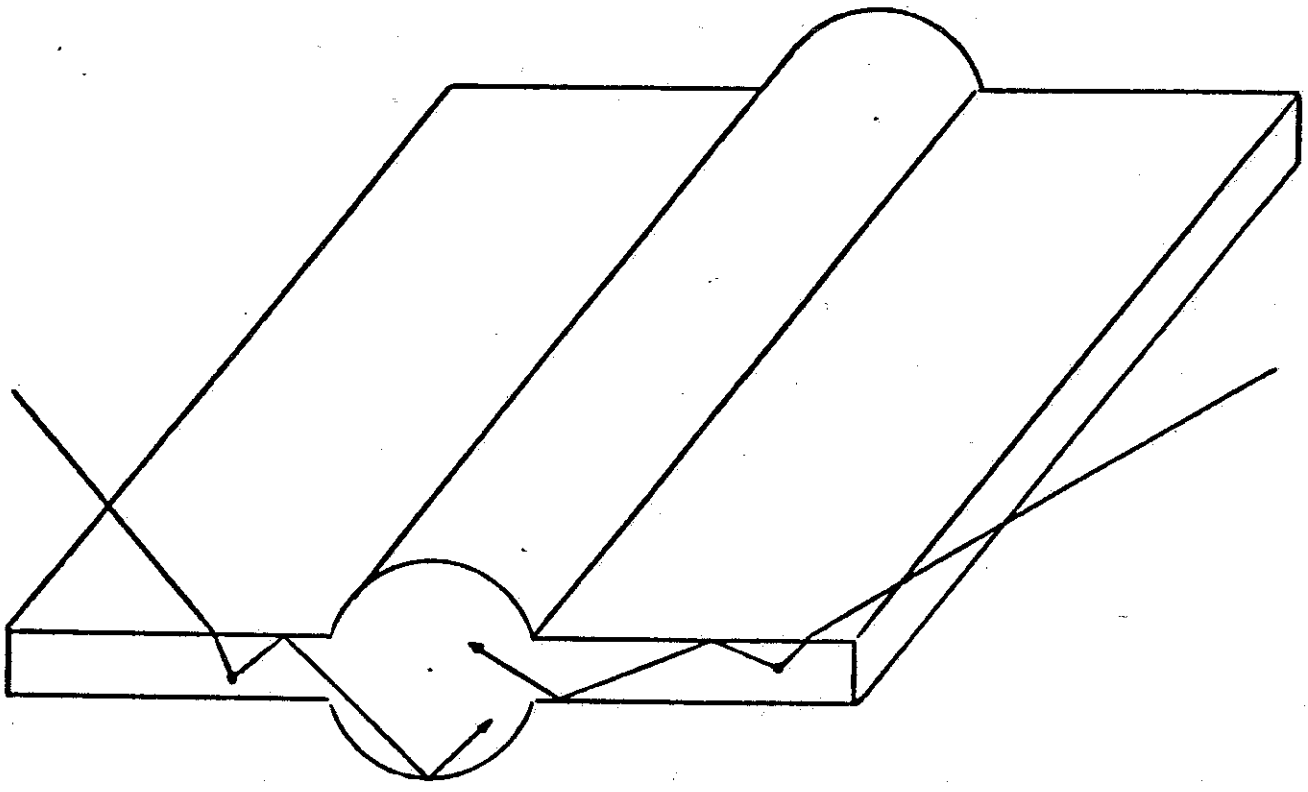

Figure 4.4

incident on a sheet of indefinite area interacts inside the sheet with a molecule of the wavelength converting material, re-emitting a photon which has an average probability given by $(1 - \frac{1}{n^2})^{1/2} = 0.75$ for $n = 1.5$ of being internally reflected at a surface of the sheet and thereafter trapped within the sheet. An obvious condition that must be met is that the material be opaque to the incident radiation but transparent to the secondary radiation; hence the need for a wavelength change. A material which allowed resonance absorption would continue to re-absorb, and eventually lose, its own secondary radiation.

The sheet could then be traversed by cylindrical channels of transparent material of index n which would serve to collect the secondary radiation from the sheet and carry it by successive internal reflections down the channels to photomultiplier tubes at the ends.

The effective area of such a device would then, in principle, be given by $A\cos\phi$, where A is the area of the surface containing the wavelength shifter and ϕ is the angle of incidence. Five such sheets of large area facing north, south, east, west and up would thus provide excellent wide angle coverage of the sky. An additional advantage is that such a wavelength shifter often serves to convert ultraviolet radiation, to which a photomultiplier is insensitive, to visible radiation, thereby matching more closely the photomultiplier spectral response.

The disadvantages of this scheme are technical ones. For most fluorescent compounds known having the appropriate properties of fluorescent efficiency, decay time and solubility there is some degree of overlap between the absorption spectrum and the emission spectrum (26), that is, the material is not completely transparent to its own secondary radiation. Moreover, the material cannot be made completely opaque to a desired spectrum of incident radiation, since consideration of losses at the edges of a light-collecting sheet require that the sheet be thin.

The efficiency of such a detector may be loosely written as

$$\eta = \iint P_e(\lambda)\ P_f(\lambda')\ F\ P_c\ d\lambda d\lambda' \qquad (4.3)$$

where $P_e(\lambda)d\lambda$ = the probability that an incident photon of wavelength λ excites a state capable of fluorescing,

$P_f(\lambda')d\lambda'$ = the probability that the state undergoes radiative decay with the emission of a secondary photon in $(\lambda', \lambda' + d\lambda')$,

F = the fraction of secondary photons trapped within the light collector,

P_c = the probability that a trapped secondary photon is collected at a phototube.

Wavelength shifting chemicals are available for which the probability of an incident photon interacting with a molecule of the wavelength shifter is high, but the probability of an

excitation to a suitable level may be of the order of 0.1 (26). Re-emission in a solid material then competes with internal quenching processes, whereby the excitation energy is transferred from one electronic state to another at a point where the potential energy curves of the two states are close enough to be strongly coupled. P_f may vary from 0.5 to 10^{-2} (26). The probability that a secondary photon reaches a photomultiplier, P_c, depends largely on absorption and scattering losses and may be written as

$$P_c \propto e^{-x/a} \qquad (4.4)$$

where x is the total path length traversed in the material and a is the mean free path of a secondary photon. Laboratory tests conducted on models of this type using p-terphenyl and POPOP* in polystyrene and POPOP in mineral oil showed that the mean free path, a, is on the order of 1 meter or less and is partly determined by impurities and microscopic scratches in the material, especially at the surfaces. In addition there is about a 10% loss for each reflection at the edges of the sheet. Taking a median angle of incidence for internal reflections of 60° and an average of 2 edge reflections, the total path length traversed by a typical light ray in reaching a photomultiplier from an actual distance of 1 meter is approximately 2.3 meters.

---

* "POPOP" = 2,2'-p-phenylene-bis-(5-phenyloxazole).

Therefore the efficiency at an actual distance of 1 meter from the photomultiplier is approximately

$$\eta \leq 0.1 \times 0.5 \times 0.75 \times e^{-2.3} = .0038 .$$

This low efficiency makes it necessary to position about one photomultiplier per 2 m^2 of light collector, and the effective area of the system in this case is approximately .01 m^2 per photomultiplier. This is a factor of 4 gain over a 25 cm^2 photomultiplier alone, but this improvement is not considered sufficient to warrant the cost and difficulties of applying the wavelength shifter technique. Furthermore, it has been found that protection of the device from weathering under outdoor conditions presents a serious problem, since microscopic scratching of the surface by dust particles and thermal strain spoils the internal reflection properties. Also, radiation damage of the light-collecting material by sunlight may act to reduce the transmission to the re-emitted light.

Therefore it was decided to employ large phototubes without either lenses or wavelength shifters.

Spectral Sensitivity -

The desire for the largest possible photocathode area led to the choice of the DuMont K-1328 photomultiplier tube, with a photocathode diameter of 37 cm and sensitive area of 1060 cm^2. This tube has a cesium-antimony cathode and a 5 mm thick lime soda glass window. Manufacturer's specifications describe the spectral response as S-11, with a

maximum cathode efficiency of 11% (photoelectrons per incident photon) at 4200 Å. The S-11 spectral sensitivity is shown in Table 4.1 for a selection of wavelengths both in terms of radiant sensitivity $s(\lambda)$ (amperes/watt of incident radiation) and quantum efficiency $\varepsilon(\lambda)$ (photoelectrons/incident photon), in both cases normalized to 1 at maximum.

The optical filter chosen to enhance the S/N ratio by spectral matching, mentioned in Chapter 3, is of dimensions 13" x 13" by 3.0 mm thick. Placed directly in front of the photomultiplier face, this reduces the useful sensitive area to 1000 cm^2. The transmission of this filter as a function of wavelength is shown in the first column of Table 4.2, for normal incidence, as measured by an absorption spectrophotometer.

In addition, to protect the photocathode surface from direct sunlight, a shutter was arranged to automatically draw an opaque screen over the phototube in the daytime, and replace this screen with a thin (.003") transparent mylar sheet during the nighttime observing period.

Finally, to provide optical matching (to minimize surface reflection losses) between the convex phototube surface and the surfaces of the mylar sheet and optical filter, these optical elements are surrounded by a bath of mineral oil (index n = 1.50). It was considered simplest to enclose the phototube, filter, tube base with voltage divider and pre-amplifier, all in a weatherproof container of galvanized iron with a transparent 1/2-inch ultraviolet transmitting plexiglas

Table 4.1

Nominal S-11 Spectral Response

λ, Å	Radiant Sensitivity s(λ)	Quantum Efficiency ε(λ)
3000	0	0
3136	.020	.028
3159	.029	.041
3285	.120	.158
3339	.185	.240
3371	.250	.321
3469	.527	.657
3500	.600	.741
3537	.678	.829
3577	.725	.877
3672	.819	.965
3711	.844	.984
3756	.852	.981
3805	.869	.988
3914	.899	.993
4059	.921	.981
4201	.972	1.000
4278	.980	.991
4344	1.000	.996
4574	.981	.927
4709	.953	.875
5000	.861	.745
5228	.727	.601
5500	.57	.448
6000	.195	.141
6500	.020	.013

Table 4.2

	Filter Transmission	Plastic-Oil Transmission	t(λ) Net Transmission	ε(λ)t(λ)
2800		<.003		
2900	<.005	.046		
2962	.0059	.165	.00097	
3000	.020	.231	.0047	0
3136	.237	.431	.102	.0029
3159	.296	.456	.135	.0055
3285	.627	.597	.374	.0591
3339	.743	.660	.490	.118
3371	.798	.694	.554	.178
3469	.903	.779	.703	.462
3500	.926	.806	.746	.553
3537	.949	.828	.785	.651
3672	.975	.907	.884	.853
3711	.975	.913	.890	.876
3756	.966	.929	.898	.881
3805	.921	.944	.869	.859
3914	.792	.968	.767	.762
4059	.298	.986	.294	.289
4201	.245	.998	.245	.245
4278	.0039	1.000	.0039	.0038
4344	.00086	↓	.00086	.0008
4574	.00002	↓	.00002	.00002
4709	<.00002	↓	<.00002	<.00002
5000	<.00002	↓	<.00002	<.00002
5228	<.00002	↓	<.00002	<.00001
5500	<.00002	↓	<.00002	<.00001
6000	.0001	↓	.0001	.00001
6500	<.00002	1.000	<.00002	<.00002

face plate, filling the entire unit with mineral oil to satisfy the optical matching requirement. Figure 4.5 presents a cross section view of the top of one such unit, showing the path a typical light ray must travel to reach the photocathode.

Column 2 of Table 4.2 shows the measured transmission of the plexiglas, mylar and mineral oil, which has an average thickness of 2.1 cm. The net transmission of the system is tabled in column 3, and column 4 lists the overall optical efficiency, the product of the system transmission $t(\lambda)$ and the photocathode efficiency $\varepsilon(\lambda)$. These functions are illustrated in Figure 4.6, which shows also the atmospheric transmission for one atmosphere ($\approx$ 8 kilometers) at sea level under very clear conditions. The phototube unit sensitivity in this diagram is the combined photocathode efficiency and plexiglas-oil transmission.

The manufacturer's specifications for cathode sensitivity were tested by laboratory measurements for one particular K-1328 phototube, yielding a maximum quantum efficiency of $0.13 \pm .04$ and a spectral distribution between 3100 Å and 4100 Å which agreed with the manufacturer's S-11 specifications to within the accuracy of the measurements. While the spectral sensitivity above 3700 Å is determined completely by the cesium-antimony photocathode surface, the short wavelength response and in particular the 3000 Å cut-off, is determined by absorption in the lime sode glass face of the phototube.

All of the transmission functions discussed above refer to normal incidence conditions. When the light is incident at an

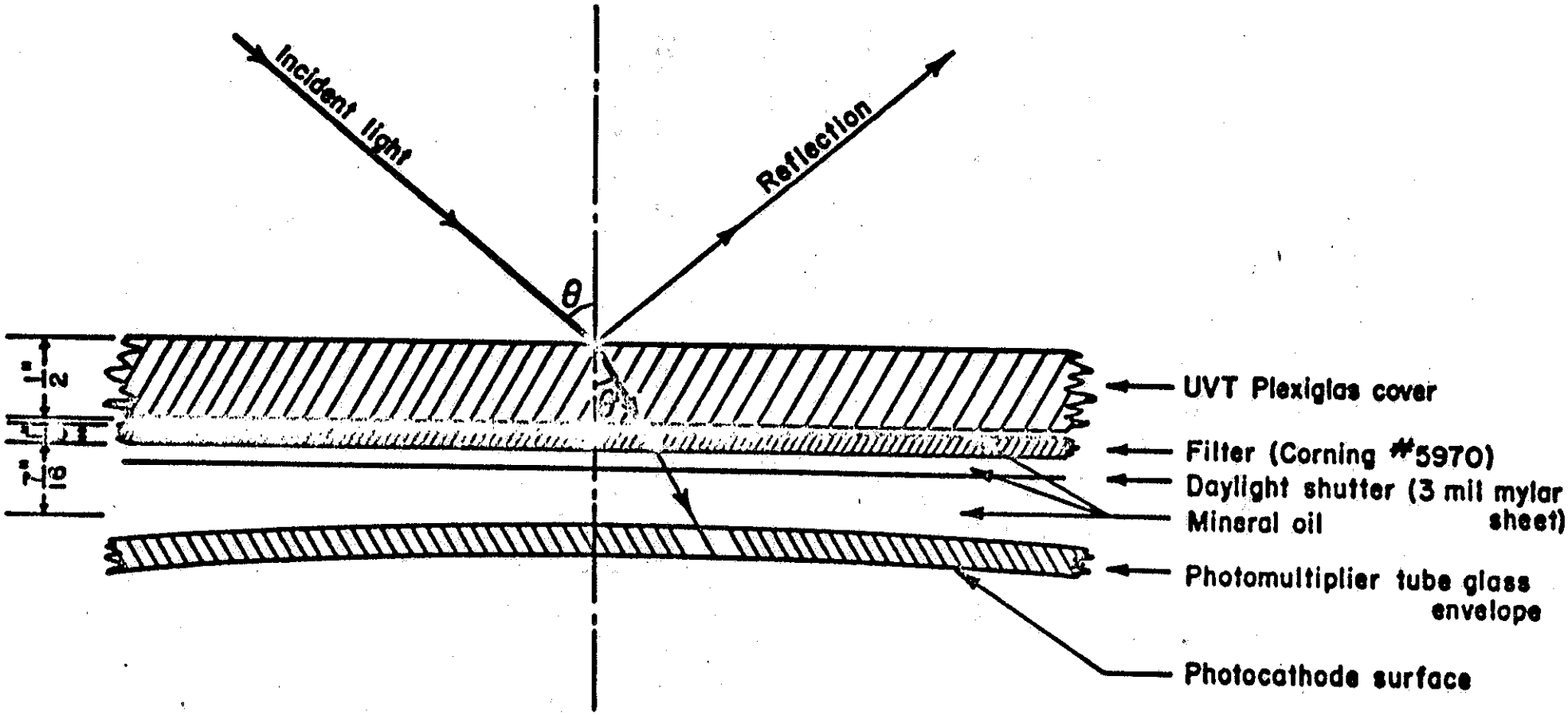

Figure 4.5 Cross Section of Top Face of a Photomultiplier Unit

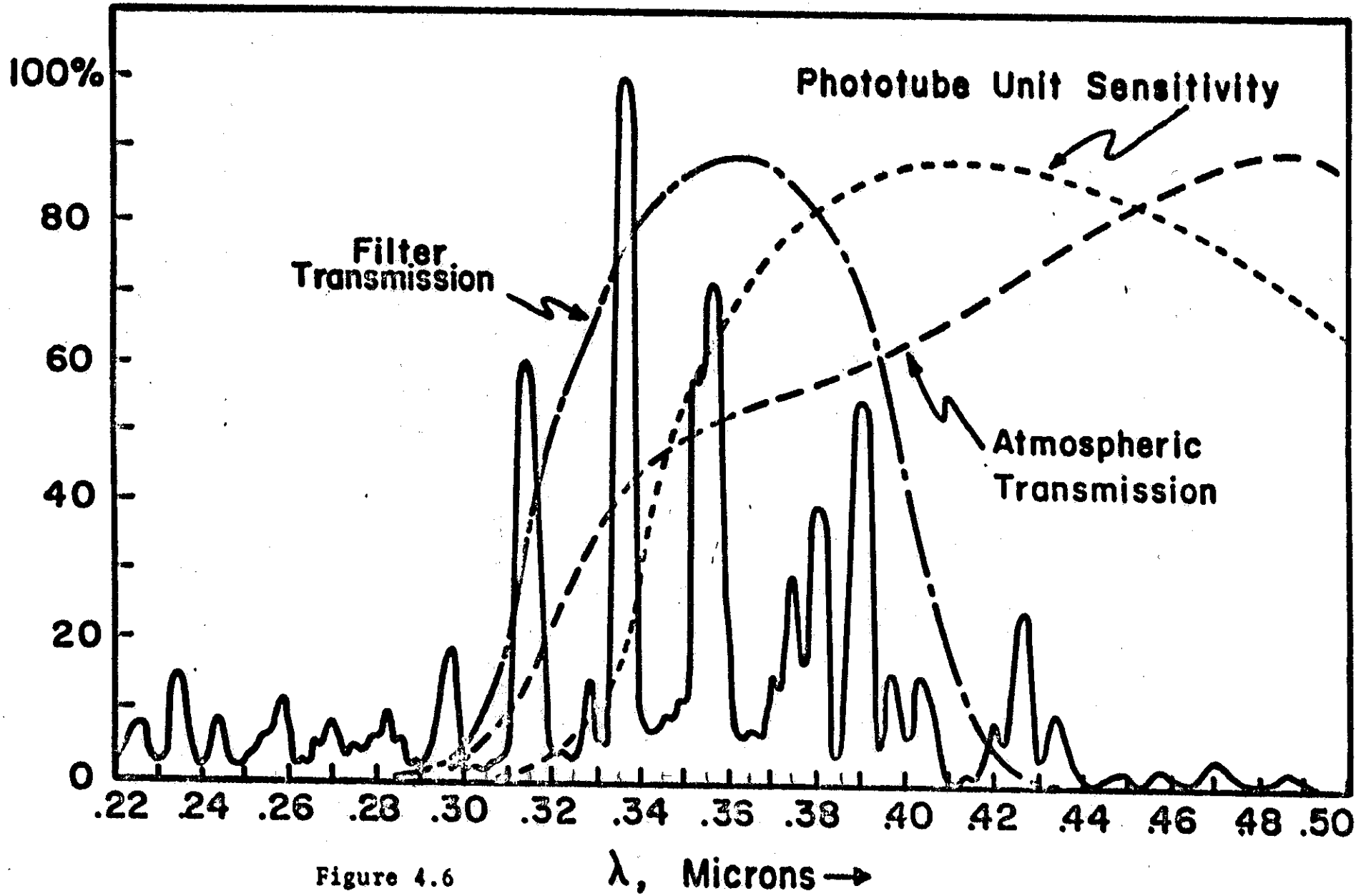
100%
80
60
40
20
0
Phototube Unit Sensitivity
Filter
Transmission
Atmospheric
Transmission
.22 .24 .26 .28 .30 .32 .34 .36 .38 .40 .42 .44 .46 .48 .50
λ, Microns →

Figure 4.6

angle θ the optical path length in the absorbing media is longer by a factor $\left(1 - \frac{\sin^2\theta}{n^2}\right)^{-1/2}$ and the light reaching the photocathode is further reduced by reflection losses.

Since absorption follows an exponential law, the transmission becomes

$$t(\lambda,\theta) = [t(\lambda)]^{\left(1 - \frac{\sin^2\theta}{n^2}\right)^{-1/2}} \tag{4.5}$$

where $t(\lambda)$ is the normal incidence transmission. This has the effect of somewhat narrowing the absorption filter bandwidth at large angles of incidence, with a maximum effect for very oblique incidence of

$$t(\lambda, \tfrac{\pi}{2}) = [t(\lambda)]^{1.35} \tag{4.6}$$

for $n = 1.5$.

The fraction of incident light $f(\theta)$ crossing the air-plexiglas boundary after reflection losses can be calculated from electromagnetic theory and is given by

$$f(\theta) = 1 - \frac{\tan^2(\theta-\theta')}{2\tan^2(\theta+\theta')} + \frac{\sin^2(\theta-\theta')}{2\sin^2(\theta+\theta')} \tag{4.7}$$

where

$$\frac{\sin\theta}{\sin\theta'} = n \quad (89). \tag{4.8}$$

The variation of the index of refraction n with wavelength between 3000 Å and 5000 Å is very small and can be neglected.

The response of the detector as a function of angle of incidence is then given by the product

$$\varepsilon(\lambda)\ t(\lambda,\theta)\ f(\theta)\ \cos\theta \quad , \tag{4.9}$$

and the angular response function for the fluorescence spectrum $F(\lambda)$ specifically can be calculated by the integral

$$\int_0^\infty F(\lambda)\ \varepsilon(\lambda)\ t(\lambda,\theta)\ f(\theta)\ \cos\theta\ d\lambda \tag{4.10}$$

E. Jenkins, in his thesis (90), has calculated this function numerically as a function of angle of incidence θ, and has shown that to a very close approximation the angular response is proportional to a power law

$$(\cos\theta)^p \tag{4.11}$$

with $p = 1.265$.

Figure 4.7 shows the result of Jenkins' numerical calculations of the integral (4.10) for the sea level air fluorescence spectrum (solid line). The function

$$(\cos\theta)^{1.265}$$

is shown in this figure by the broken line. The small circles show the function $\cos\theta$ for comparison.

For experimental verification of the above approximation, Figure 4.8 shows a comparison of Jenkins' calculations (solid lines) and experimentally measured points (small triangles) for two specific wavelengths, where α and s are the normal incidence absorption factors for the plexiglas-oil-filter combination and the glass face of the phototube respectively, defined by

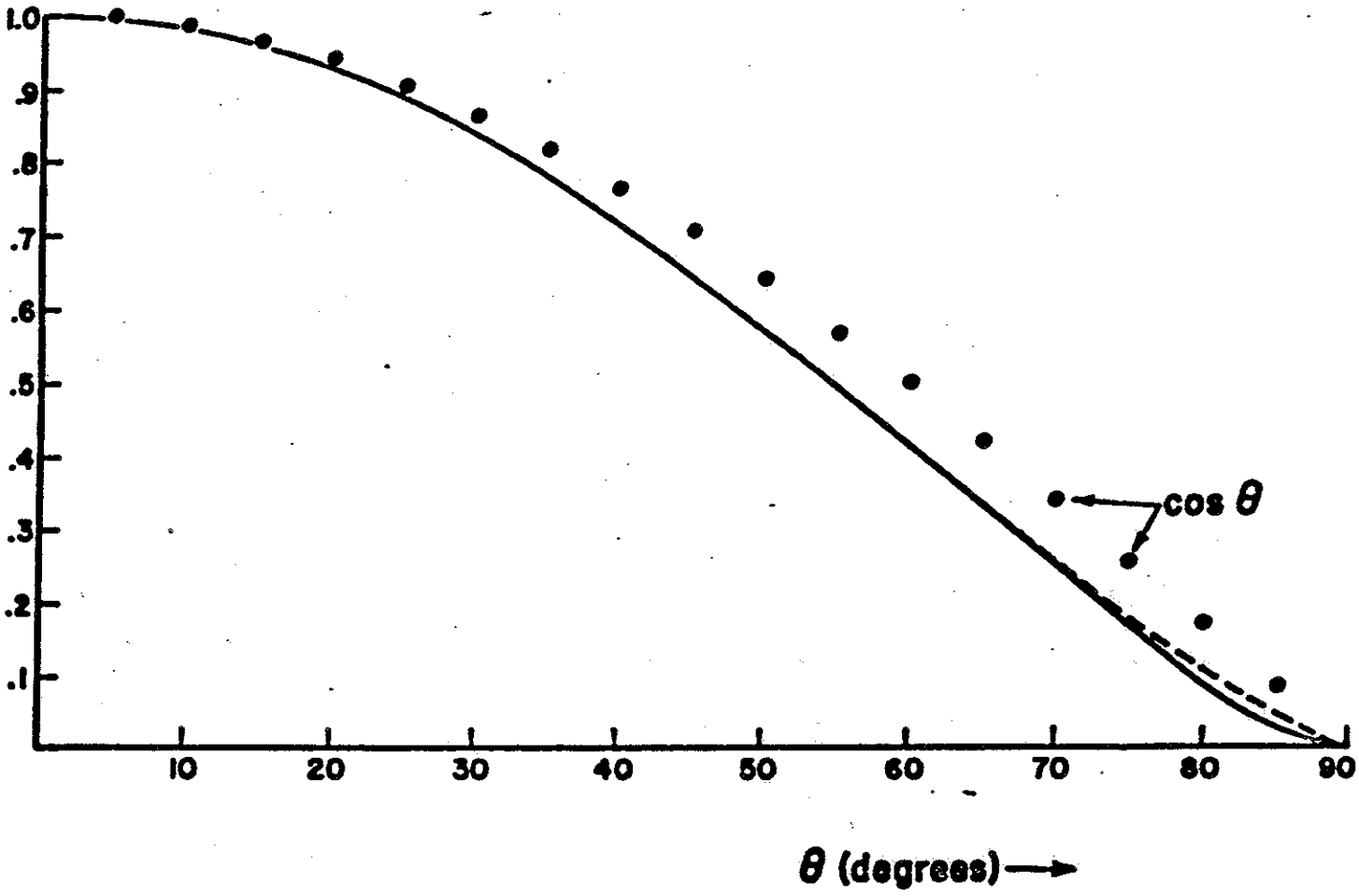

Figure 4.7 Angular Response of Photomultiplier Unit

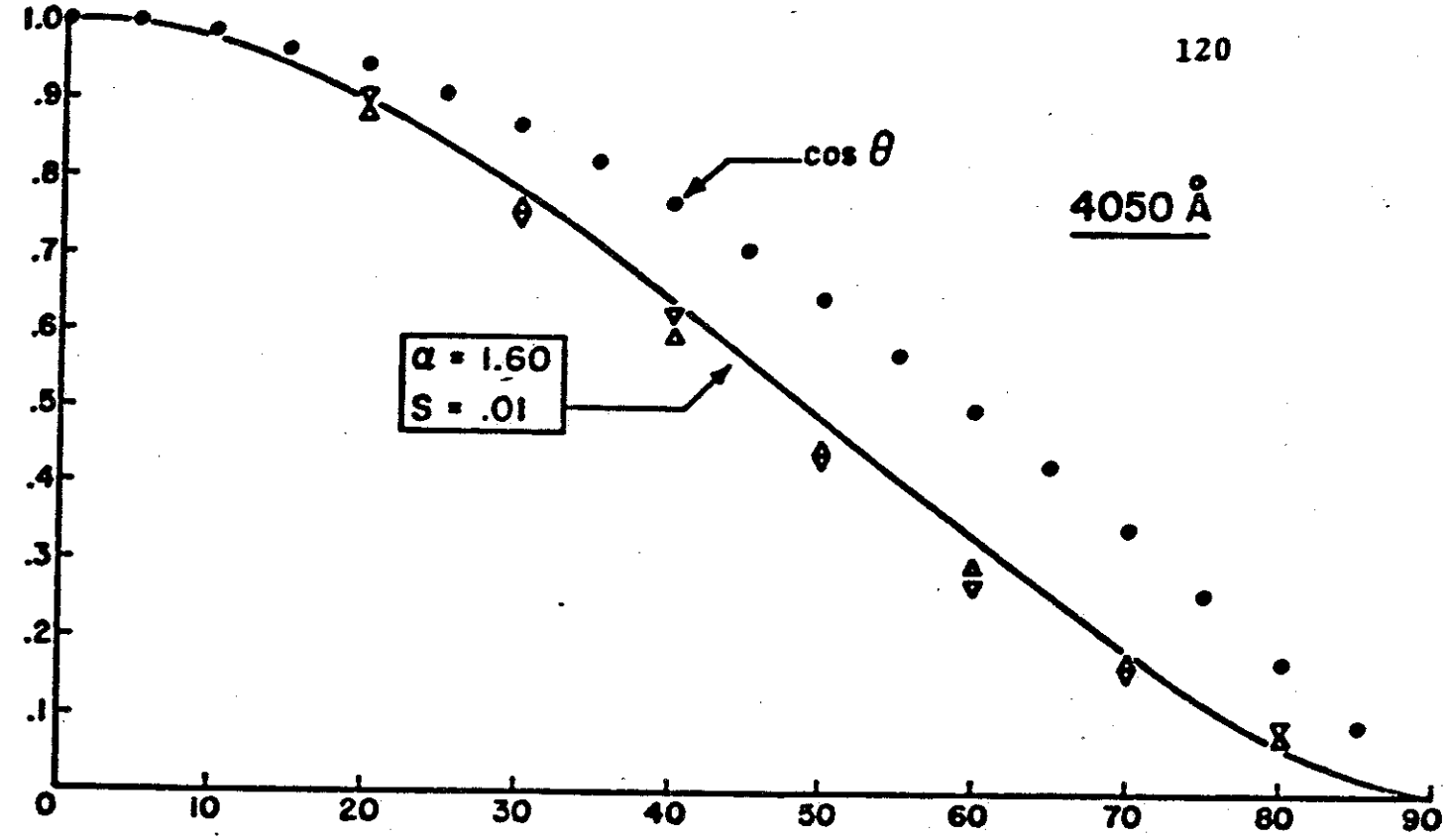
1.0
.9
.8
.7
.6
.5
.4
.3
.2
.1
0
10
20
30
40
50
60
70
80
90
cos θ
4050 Å
α = 1.60
S = .01

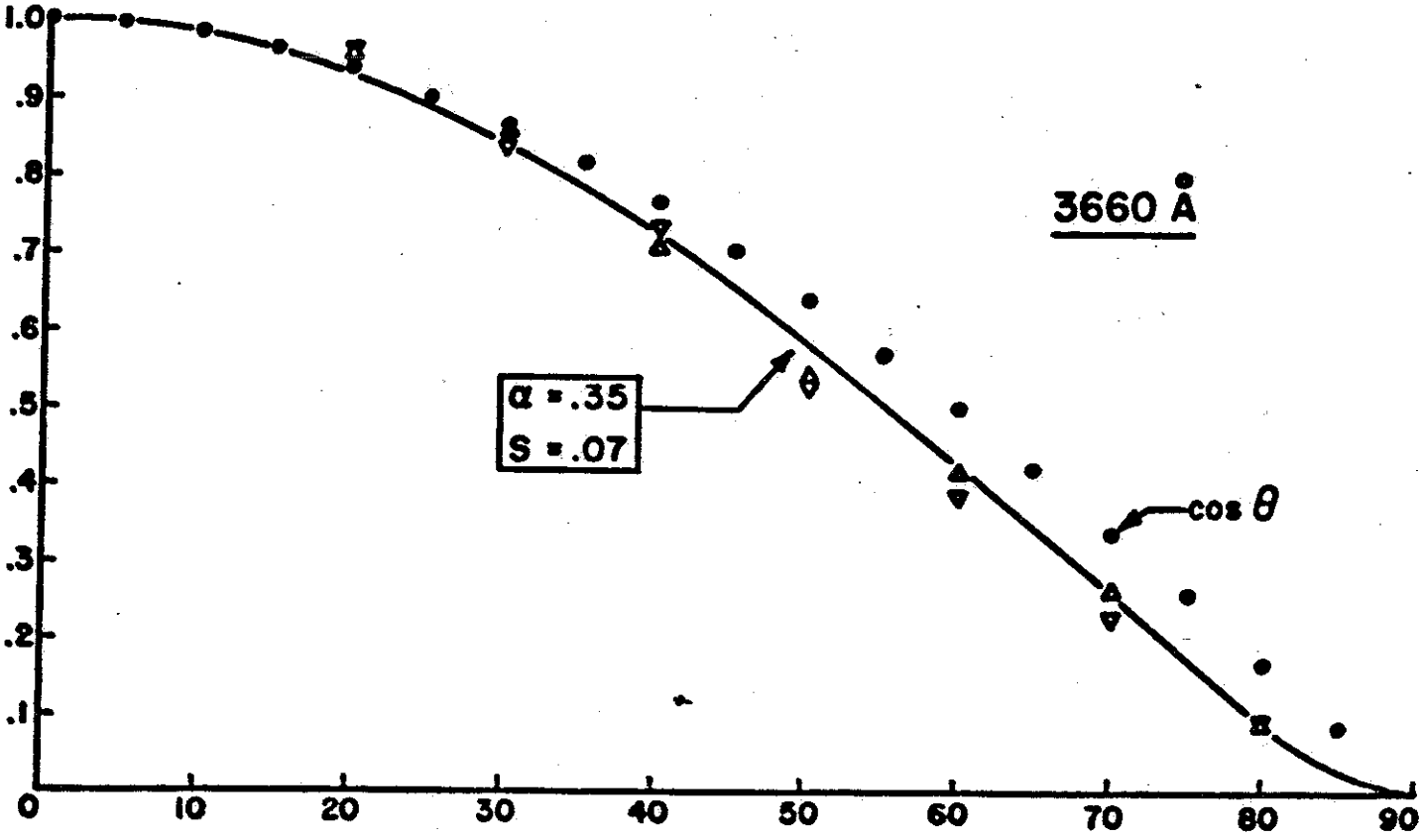
1.0
.9
.8
.7
.6
.5
.4
.3
.2
.1
0
10
20
30
40
50
60
70
80
90
3660 Å
α = .35
S = .07
cos θ

Figure 4.8

$$t(\lambda) = e^{-\alpha(\lambda)} \times e^{-s(\lambda)} \quad . \qquad (4.12)$$

Choice of Site -

Several requirements are desirable in the selection of an experimental location for the detection of atmospheric fluorescence, notably:

1. An area offering clear sky visibility a large percentage of the time,
2. Freedom from background light such as scattered light from populated areas,
3. An unobstructed field of view down to within say 2^{o} of the horizon,
4. Line-of-sight visibility between stations requiring optical communication for purposes of fast coincidence timing or atmospheric transmission measurements, and
5. Optimum altitude for the size of air shower anticipated.

We have seen in Chapter 3 that although the fluorescent efficiency increases with altitude due to a moderation of quenching reactions, the number of excitations per unit path length decreases due to the lower air density. The net effect, shown in Figure 2.12, is a very slowly increasing yield with altitude. However, for air showers in the energy range 10^{19} ev to 10^{21} ev, the shower maximum occurs on the average close to sea level, and furthermore the measurement of total energy in a shower by fluorescence light collection is facilitated by seeing well beyond the shower maximum. For these reasons the

lowest possible altitude still satisfying the first four conditions is optimal for these very high energy showers.

For the pilot experiment described here, requirement No. 1 was compromised by the desire to build an experimental facility with quick access to the Cornell University campus, and requirements 2, 3, and 4 overruled altitude considerations when it was found that several bare hilltops in the Ithaca, N.Y., area satisfied the visibility conditions nicely. The map on page 123 shows the geographical location of the detector stations chosen for this experiment.

Electrical Design Considerations -

The characteristic property of the pulse of light from a cosmic ray air shower is the duration and shape of the pulse as seen by the different optical channels. An effective way to analyze these pulses is to display them directly on cathode ray tubes and to photograph simultaneously the signals seen in each channel, along with appropriate calibration markers.

Since these pulses are not expected to last longer than about 60 microseconds, nor to change in amplitude appreciably in a time shorter than 1 microsecond, the associated amplifiers need not respond to frequencies lower than about 100 cps nor higher than 10^6 cps to preserve the signal shape. A response to higher frequencies introduces noise which is due only to the quantum fluctuations in the photoelectron current and not to the progress of the air shower.

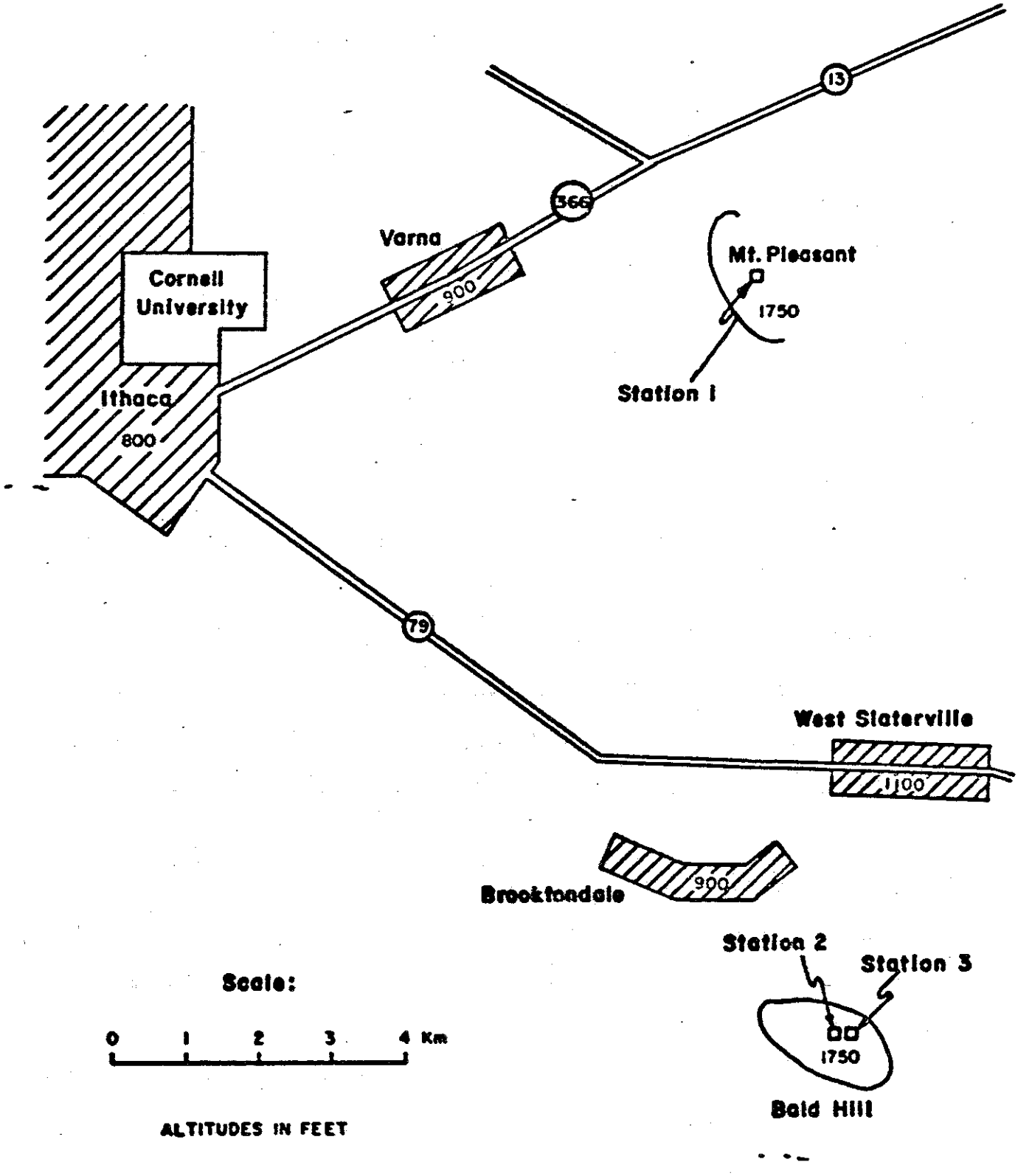

Figure 4.9 Map of the Ithaca Area Showing the Location of the Detector Stations

Triggering of the cathode ray tubes and camera servo-mechanism is suitably accomplished by integrating the signals received over a time comparable with the duration of an average air shower fluorescence pulse and thus demanding that a combination of the amplitude and the duration of a pulse fulfill a pre-set condition. Further discrimination against noise is easily effected by demanding a coincidence between at least two of the five channels in a single detecting station. The use of delay lines with sampling taps at regular intervals provides at the same time for the above-mentioned integration and for storage of the signals while a triggering decision is being made.

Amplifiers -

Positioned close to the base of each photomultiplier tube is a voltage divider for the photomultiplier dynodes and two stages of gain 1 preamplifier. The geometry of a phototube unit is shown in Figure 4.10. The photomultipliers are operated at moderate voltages ranging from 800 to 1200 volts, depending on the individual tube characteristics, to provide a dynode gain of approximately 10^5. This low gain is necessary to avoid exceeding the maximum anode current rating of the tubes when they are exposed to the scattered light from nearby communities, which is present under overcast or haze conditions. Such scattered light frequently raises the background light intensity by a factor of 10. The clear night sky light (see

Cross Section of
a Phototube Unit

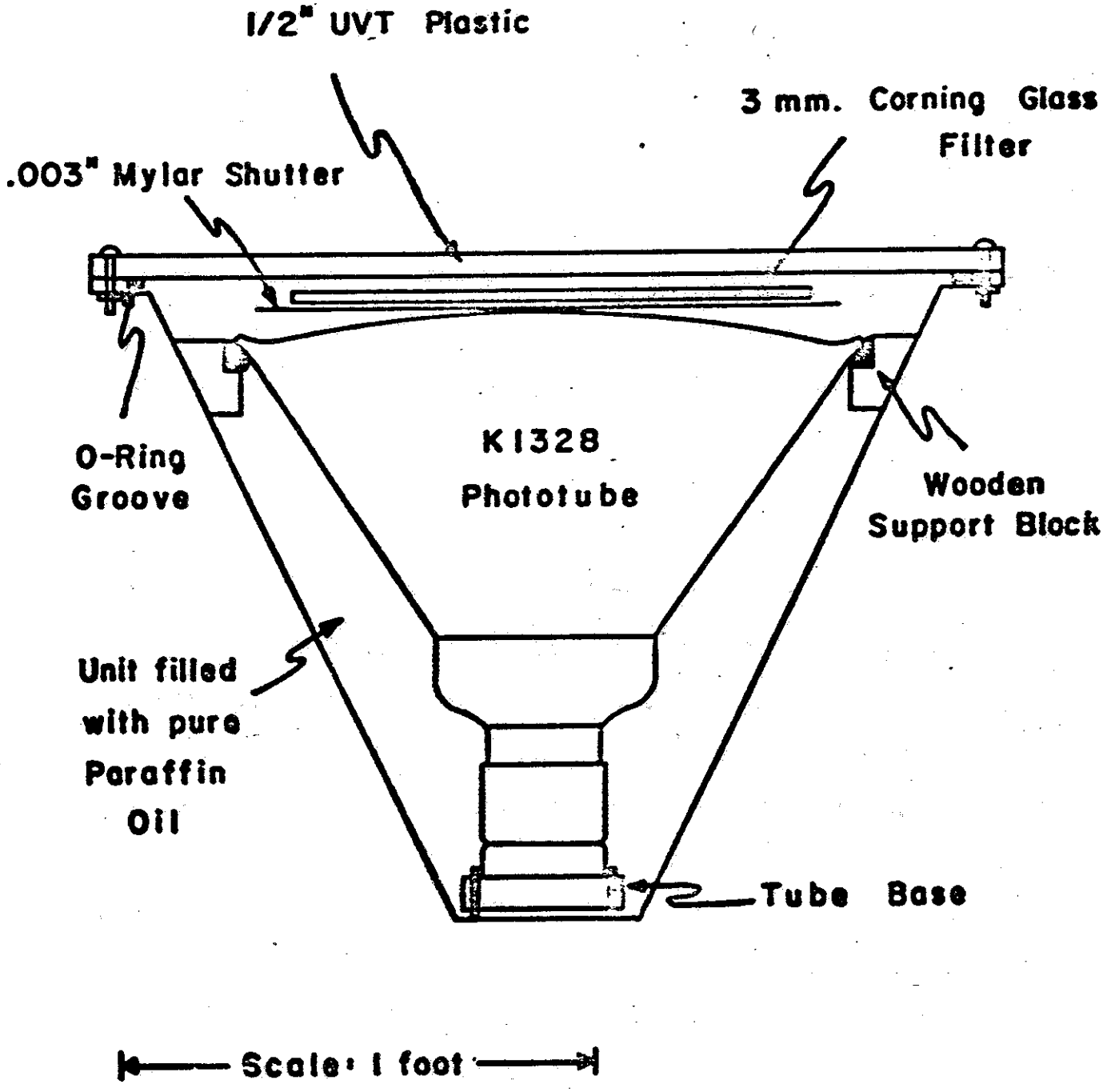

Figure 4.10

Table 3.1) seen through the optical filter leads to a photocurrent at the first dynode of about 5×10^{-10} amperes.

The voltage divider and preamplifier are shown in Figure 4.11. The potential between cathode and first dynode is kept above 220 volts to insure adequate collection of photoelectrons at the first dynode. A high value resistor (10^8 ohms) is placed between the cathode and the high voltage supply as a safety feature to decrease the accelerating voltage in the event that a sudden intense flux of light floods the photomultiplier tube.

Stray capacitance in the pre-amplifier limits the frequency response to about 2 mc/s. With this cut-off frequency, the RMS fluctuation current at the anode due to the night sky light is approximately 2×10^{-6} amperes, and the RMS voltage fed to the succeeding amplifiers is approximately 6.2×10^{-3} volts. The amplifiers are A-C coupled, blocking frequencies below about 5 cps.

Following the preamplifier, the signals pass in succession through a variable attenuator, to adjust for differences in amplifier gain between channels, a wideband voltage amplifier of gain 10, a narrow band filter set to eliminate the 120-cps component of noise introduced by artificial light sources, a logarithmic amplifier, a length of HH-1600 delay line which delays signals by 14 microseconds without appreciable distortion for frequencies between 5 cps and 1 mc/s, and finally two stages of gain 10 wide-band voltage amplifier which drive the

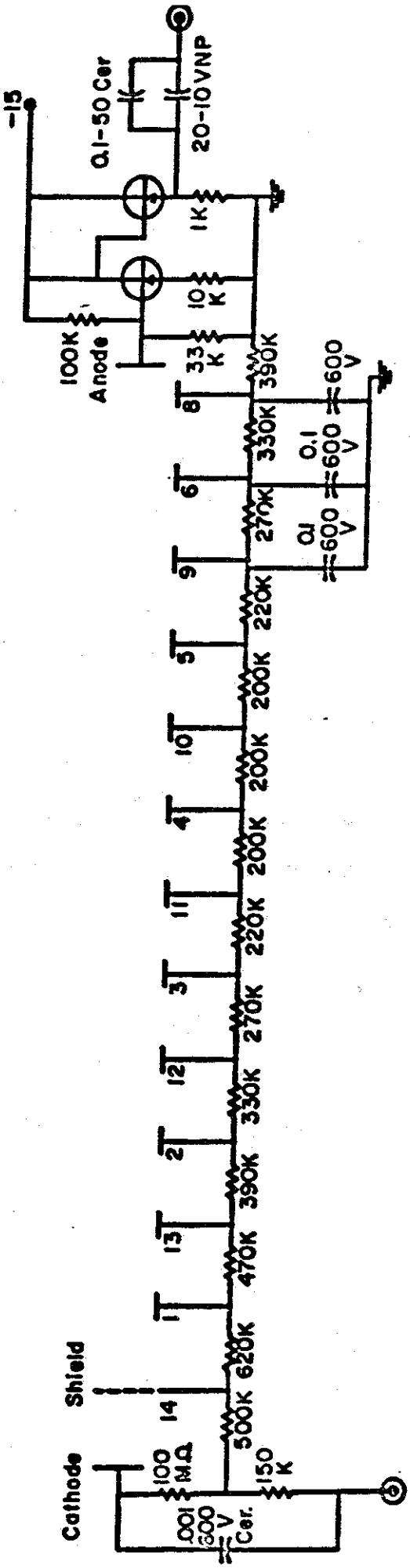

Figure 4.11 K-1328 Phototube Base

vertical deflection plates of a 5YP11 five-inch diameter cathode-ray tube. These stages are shown in Figures 4.12 and 4.13. The overall rise time of the amplifier system is $\approx$ 1.5 μsec.

The need for a selective electrical filter to prevent amplification of 120 cps signals became evident after a strong modulation of the night sky light at this frequency was observed, even on quite clear nights. This was attributed to scattered light from incandescent lamps and mercury arc lamps in the Ithaca area. Since the duration of the cathode-ray tube sweep (60 μsec) is much shorter than 1/120 second, this modulation had the effect of shifting up and down the baseline from which the amplitudes of short pulses must be measured.

The 120-cps filter is a parellel combination of a high-pass and a low-pass R-C filter, both selected for $1/4\pi RC$ = 120 cps. A compensating circuit after the filter corrects for the small negative slope which the filter introduces into long square pulses because of the attenuation of low frequency components.

The use of a logarithmic amplifier arose from the wish to display on a single cathode-ray screen both the amplitude of the normal background noise and the amplitudes of the largest cosmic ray pulses. The circuit is modelled after a design by Ophir and Galil (91) and uses the logarithmic current-voltage characteristic of a Zener diode. The diode chosen is the 1N761 which has a reverse breakdown characteristic

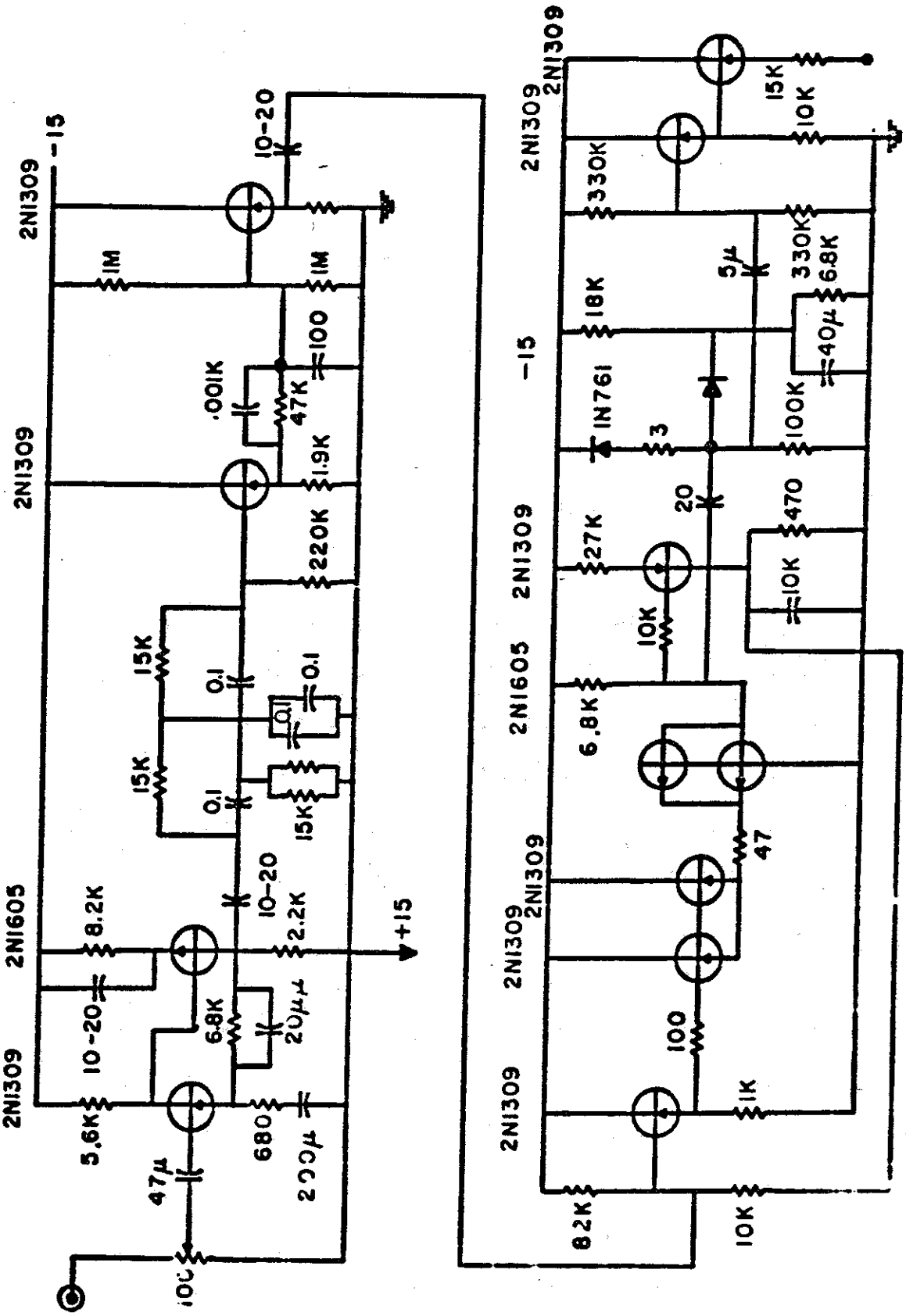

Figure 4.12 Pre-Amplifier, 120-cycle Filter, and Logarithmic Amplifier

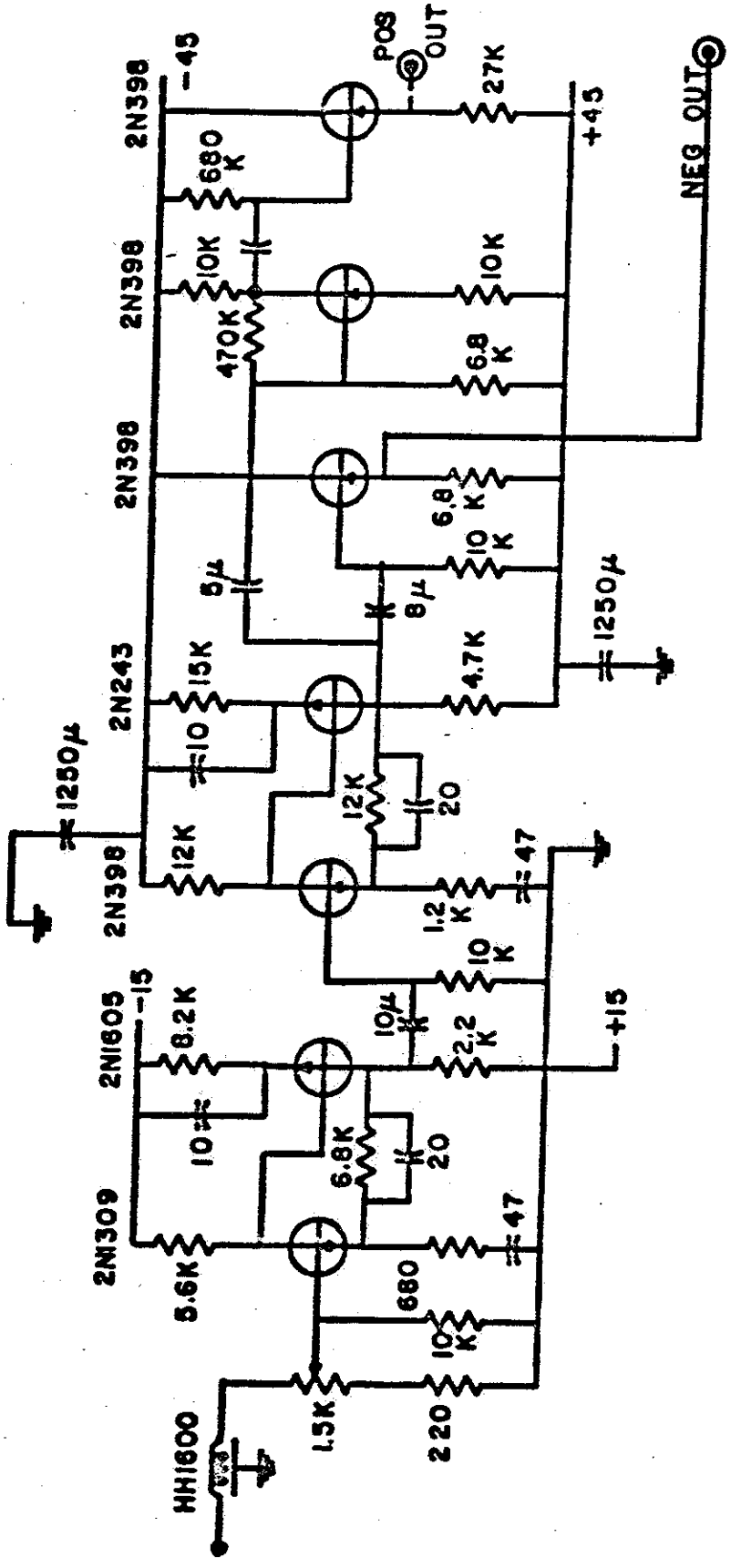

Figure 4.13 Main Amplifier

approximately obeying

$$V = k \ln (I-I_o) \qquad (4.13)$$

where k is a constant and I_o is the quiescent current in the diode, approximately 100 μamps in this circuit. A small resistance (approx. 3 ohms) in series with the Zener diode improves the logarithmic characteristic for large signals. The amplifier is logarithmic over 3 decades, compressing input signal amplitudes of .05 volt to 5 volts into an output amplitude range of 0.7 volt to 2.3 volts.

The final amplifier stage drives the two vertical deflecting plates of the 5YP11 cathode-ray tube with symmetrical pulses of opposite polarity. Each plate contributes a deflection factor of 11 volts per cm. The driver amplifier is designed to produce pulses up to an amplitude of 35 volts, to produce a maximum total deflection of 6.4 cm.

Figure 4.14 shows the net amplifier response as found for one particular channel. S is the pulse amplitude in volts at the input to the first linear amplifier and x is the pulse amplitude in cm. resulting on the cathode-ray tube screen. Experimental curves were plotted for each channel using 10 μsec square pulses, and although the characteristic curves of the five channels differed somewhat, it was found that they could all be closely fitted, for purposes of analysis, by a function of the form

$$(S+S_o) = C_o + C_1 x + C_2 x^2 + C_3 x^3 + C_4 x^4 \qquad (4.14)$$

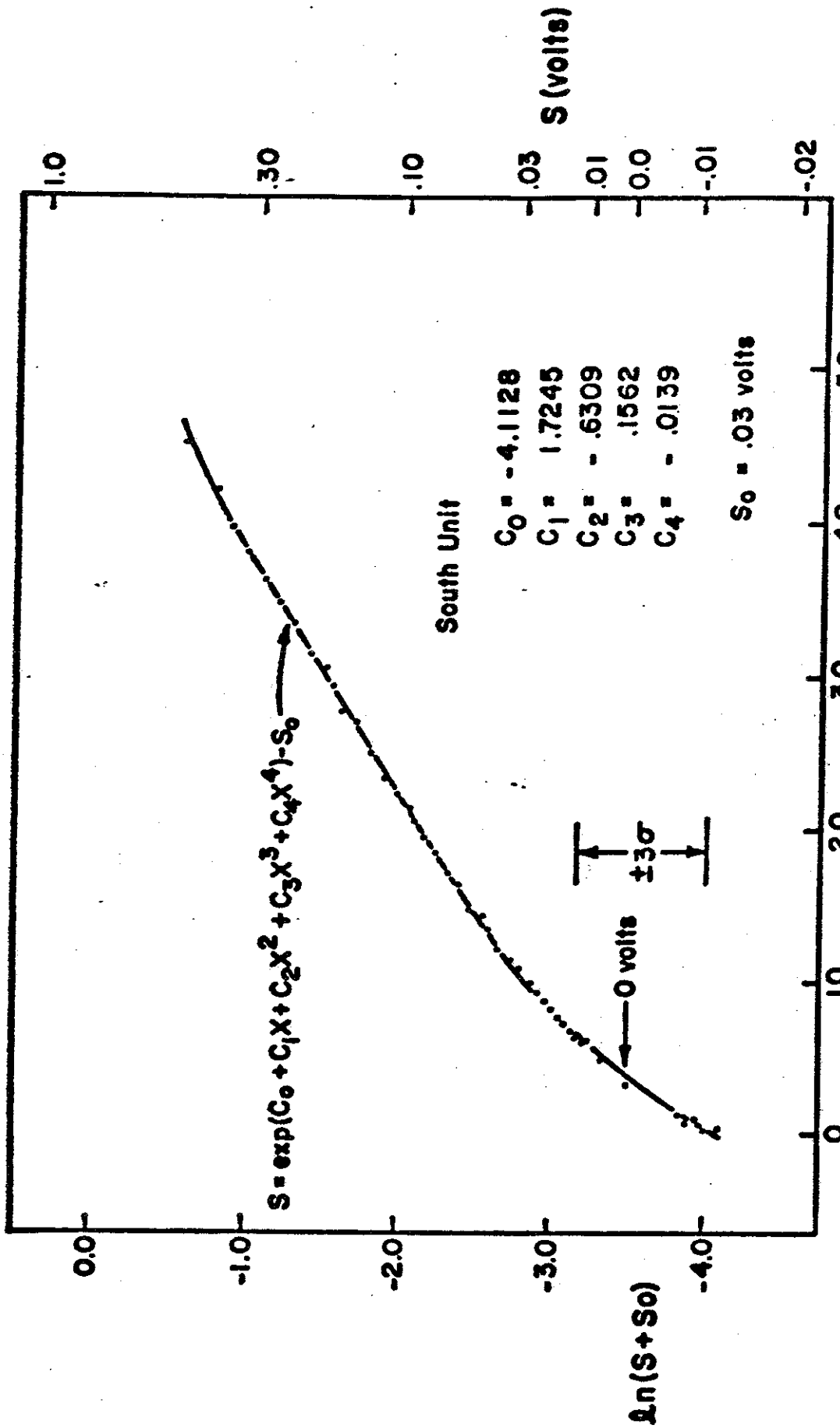

Figure 4.14 A Typical Amplifier Response Curve

where S_o, C_o ... C_4 are constants for a particular channel. A troublesome problem concerns the variation of these characteristic curves with time. It was found that the response function depends somewhat on the amplifier supply voltages, and also that increased temperature has the effect of shifting the curve of Figure 4.14 upwards. For these reasons frequent amplifier calibrations were performed during the course of the experiment to minimize calibration errors.

As may be seen in Figure 4.14, the amplifiers respond to both positive and negative signals. This is necessary since the instantaneous voltage fed to the amplifiers from the photomultiplier anode may be either higher or lower than the average voltage due to the night sky light, which corresponds to S = 0.

Also in Figure 4.14 is shown the signal amplitude representing three standard deviations of noise for this particular channel, illustrating the approximate full amplitude of the noise distribution from the background night sky light.

For the measurement of pulse amplitudes a reference baseline is produced by following each cathode-ray tube sweep by another sweep (within 200 microseconds) during which the final amplifier is driven into negative saturation.

Pulse Discrimination -

In order to effectively sense the arrival of a pulse of fluorescence light from an air shower over the distribution of background noise, a number of requirements are imposed which

make accidental triggering on background noise rather improbable. These requirements are illustrated in Figure 4.15. The signal from each photomultiplier passes through a delay line and is sampled by high impedance taps at intervals of 0.8 μsec, slightly less than the response time $1/\Delta f$ of the amplifiers. The taps are arranged into two groups of five, separated by a gap of 1.6 μsec, and added to form two new signals, one approximately proportional to the integral of the primary signal over 3.2 μsec and one proportional to the integral of the primary signal over 8 μsec. A diode coincidence circuit adds the requirement that the integrated signal be non-zero from both groups of 5 delay line taps; that is, the signal must be above the noise for at least 1.6 μsec, the length of the gap in the addition. This in general prevents triggering of the recording system on very narrow pulses such as are produced by the Cerenkov radiation from low energy cosmic ray showers in the air directly over the detector or by Cerenkov radiation from cosmic ray muons traversing the detector itself.

Two discriminators, which are referred to as "High" and "Low" and are adjustable in parallel, then produce output pulses whenever the signal, integrated over 8 μsec and 3.2 μsec respectively, is well above the average integrated noise.

The generation of a "Master" pulse, which triggers the recording system, requires that there be a "High" pulse in any channel and, within about 8 μsec, a "Low" pulse in at least two adjacent channels, where we define "adjacent" by the

Circuit Diagrams for Recorder Trigger Logic

A. For each photomultiplier

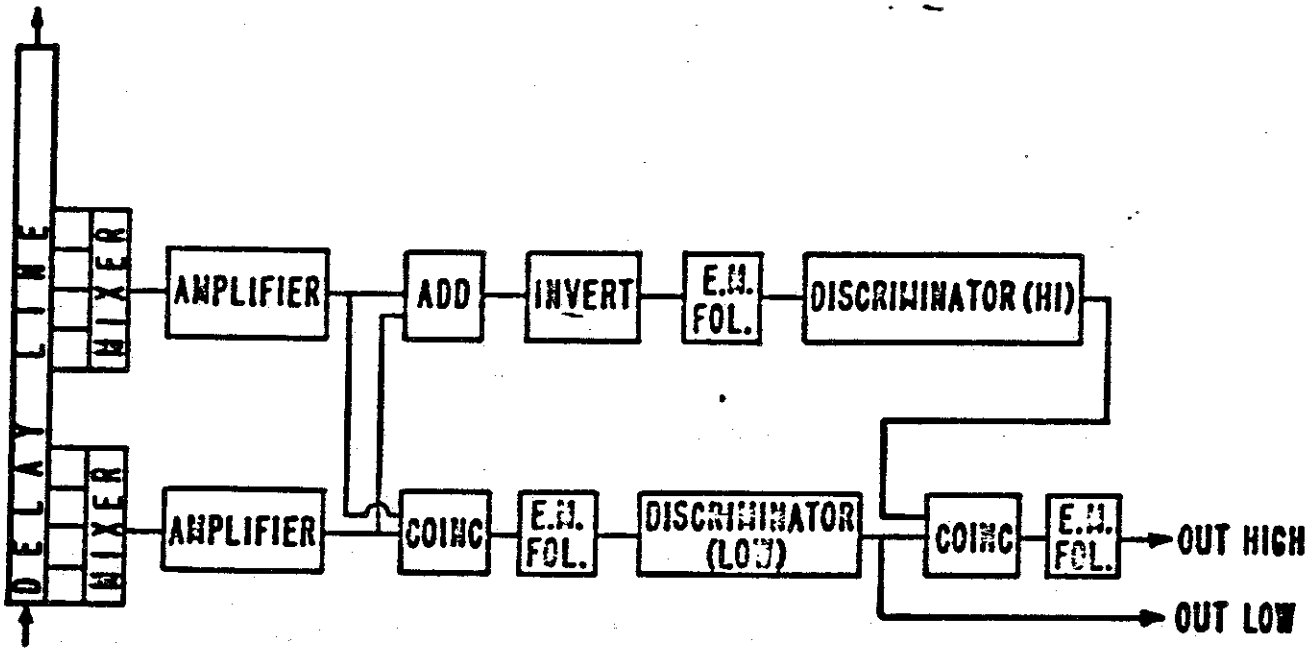

B. For all tubes

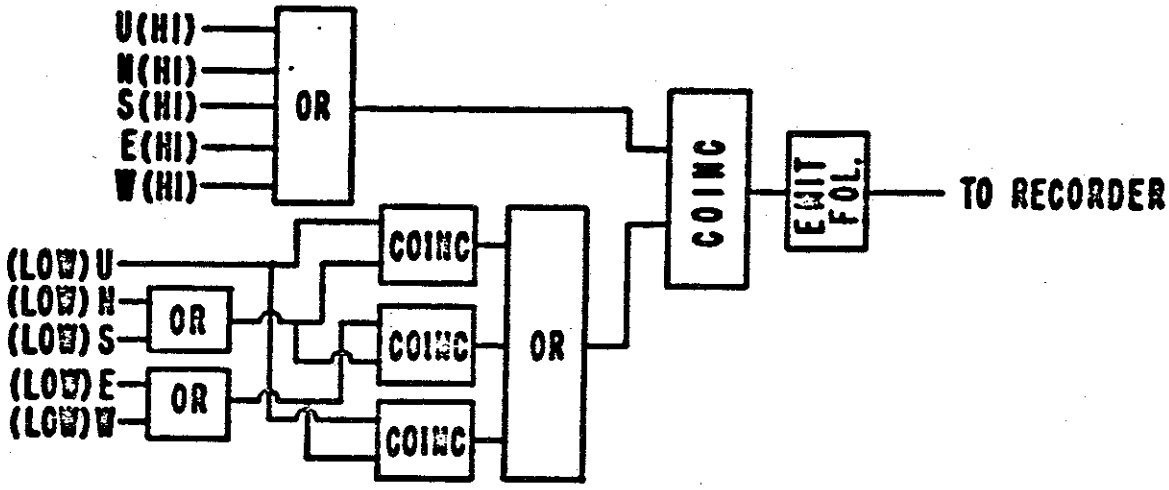

Figure 4.15

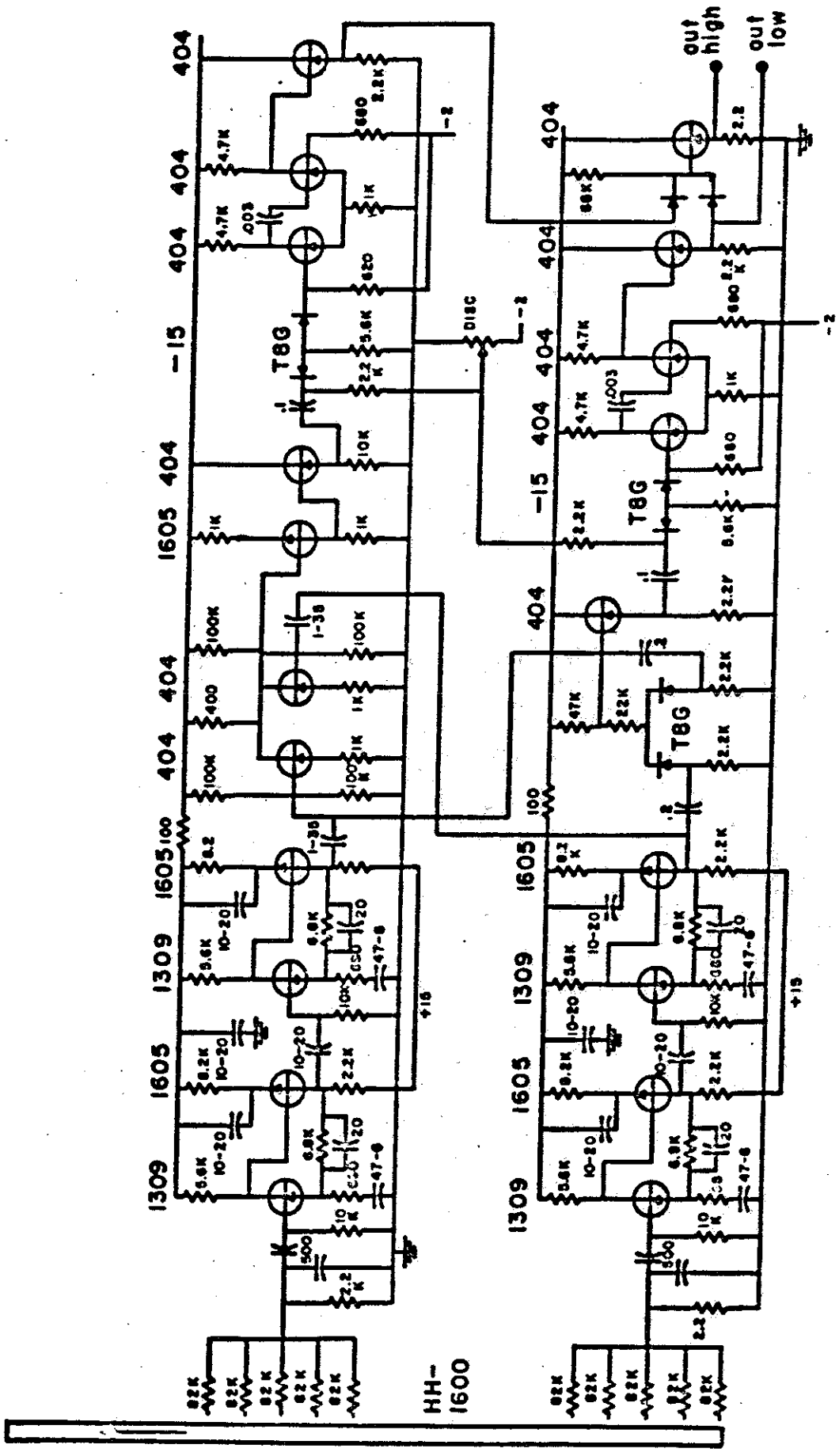

Figure 4.16 Discriminator Logic

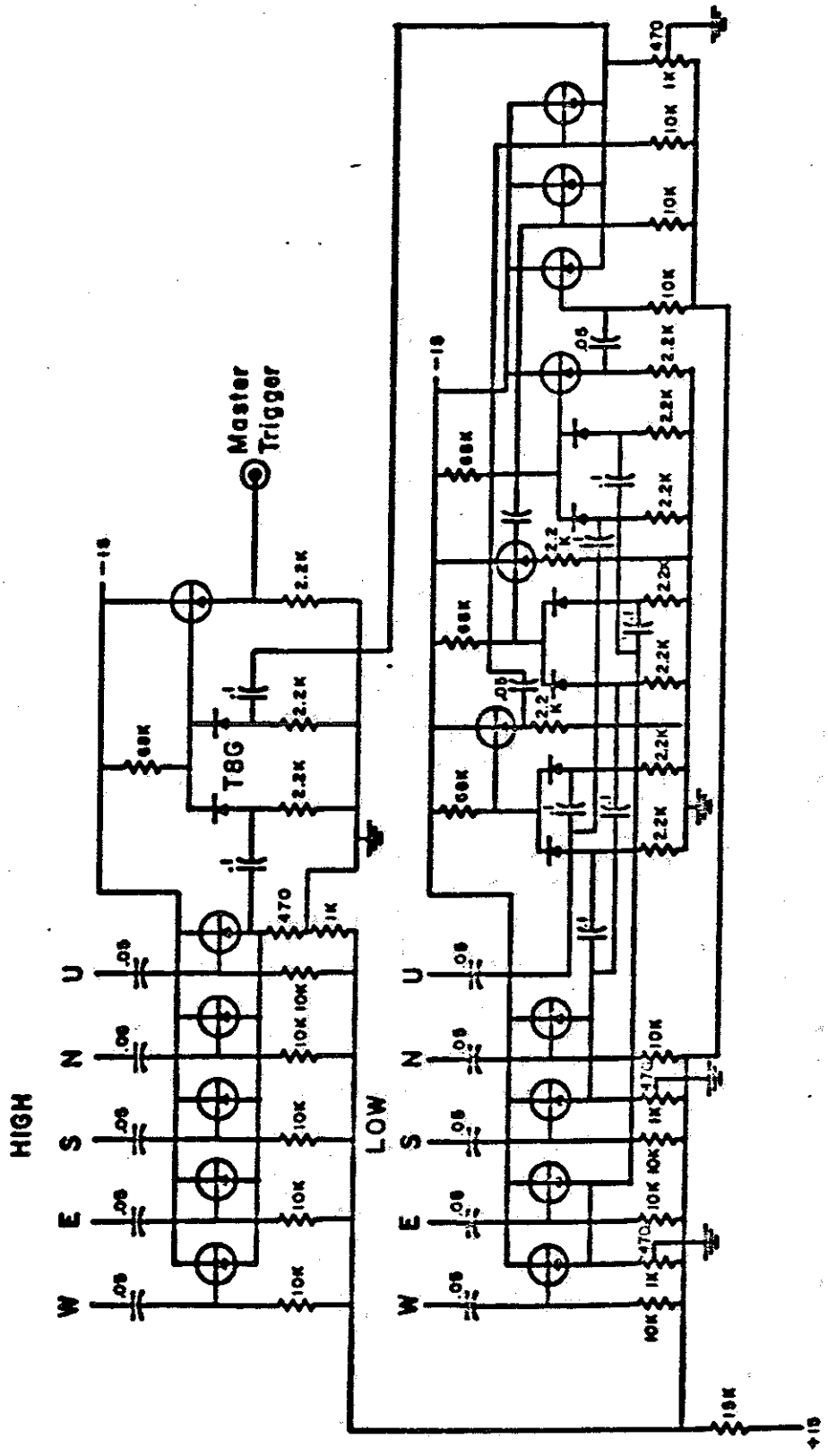

All Transistors 2N404

Figure 4.17 Coincidence Logic

chart below:

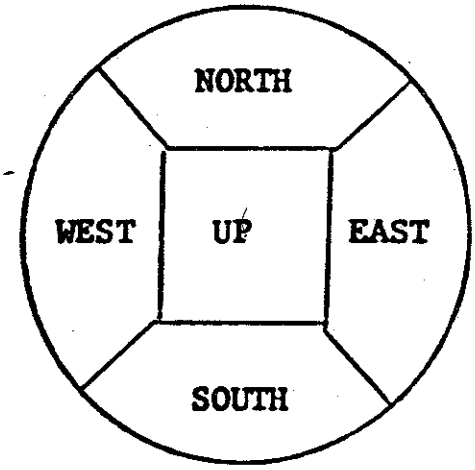

Figure 4.18

The counting rate of High, Low and Master pulses as a function of discriminator setting can be calculated from the following considerations: The mean number of photoelectrons generated by the night sky light in one photomultiplier within the response time $1/\Delta f$ of the amplifiers is approximately 2000, and since the emission of photoelectrons is a random process, the distribution of this number may be considered Gaussian with mean 2000 and standard deviation $\sqrt{2000} = 45$. The deviation from the Poisson distribution is less than 10% up to four standard deviations.

Assume then that the noise voltage v at any instant obeys a Gaussian distribution with mean 0 (since our amplifiers pass only the AC component) and standard deviation σ. The integrated noise voltage from five taps is therefore also Gaussian with mean 0 and standard deviation $\sqrt{5}\,\sigma$, assuming the five

samplings are uncorrelated, and the added noise from all ten taps follows a Gaussian distribution with standard deviation $\sqrt{10}\ \sigma$.

The first coincidence circuit is placed before the discriminator in order to first select pulses wider than 1.6 μsec without demanding large pulse amplitudes. In fact, the diode coincidence network in this case can be described to a good approximation for small signals as performing the algebraic operation

$$\begin{aligned} \frac{1}{v_o} &= k\left(\frac{1}{v_1}+\frac{1}{v_2}\right) \quad , \quad v_1, v_2 > 0 \\ v_o &= 0 \quad , \quad v_1, v_2 \leq 0 \end{aligned} \tag{4.15}$$

where v_o is the output signal voltage

v_1 and v_2 are the two input signals,

and k is a constant, approximately equal to 0.7 in the circuits described here.

Exact analysis of the pulse height distribution of the output signal v_o is complex, but to a first approximation, if v_1 and v_2 are Gaussian with the same standard deviation σ, and if we write $P(v > x)$ for the probability that the noise exceeds the level x within the resolving time of the associated amplifiers, then

$$P(v_o > x) \approx 2\left[P(v_1 > 2kx)\right]^2 \tag{4.16}$$

provided $x \gg \sigma$.

The probability that the integrated noise voltage from

five taps exceeds 2kx within the amplifier resolving time $1/\Delta f$ is

$$P = \int_{2kx}^{\infty} \frac{1}{\sqrt{5}\,\sigma\sqrt{2\pi}}\, e^{-\frac{1}{2}\left(\frac{v}{\sqrt{5}\,\sigma}\right)^2} dv \qquad (4.17)$$

$$\approx \frac{\sigma}{2kx}\sqrt{\frac{5}{2\pi}}\, e^{-\frac{1}{2}\left(\frac{2kx}{\sqrt{5}\,\sigma}\right)^2}, \text{ for } 2kx \gg \sqrt{5}\,\sigma. \qquad (4.18)$$

Therefore the rate at which the coincidence output triggers the low discriminator, when the discriminator is set to trigger at a voltage level x, is

$$R_L \approx \frac{5\sigma^2\Delta f}{4\pi k^2 x^2}\, e^{-\left(\frac{2kx}{\sqrt{5}\,\sigma}\right)^2}, \qquad (4.19)$$

provided the discrimination level is high enough to avoid saturation of the discriminator. The discriminator produces a standard 2 microsecond square pulse output regardless of the duration of the excess.

The trigger rate of the high discriminator is given by the rate at which the integrated noise from ten taps exceeds the level x

$$R_H = \int_{x}^{\infty} \frac{1}{\sqrt{10}\,\sigma\sqrt{2\pi}}\, e^{-\frac{1}{2}\left(\frac{v}{\sqrt{10}\,\sigma}\right)^2} dv \qquad (4.20)$$

$$\approx \sqrt{\frac{5}{\pi}}\,\frac{\sigma}{x}\, e^{-\frac{1}{2}\left(\frac{x}{\sqrt{10}\,\sigma}\right)^2}, \text{ if } x \gg \sqrt{10}\,\sigma. \qquad (4.21)$$

The final coincidence in Figure 4.15 ensures that every firing of the high discriminator is accompanied by a firing of the low discriminator, or, in other words, that a pulse which fulfills the amplitude requirement also fulfills the minimum length requirement.

The triggering of the recording system requires a "high" pulse from any one channel in coincidence with a "low" pulse from an adjacent channel. From Figure 4.15, it may be seen that there are 16 ways in which a "high" pulse and a "low" pulse can combine from adjacent channels. Therefore the rate of "master" trigger pulses is given by

$$R_M = 16\,\tau R_H R_L , \qquad (4.22)$$

where τ is the effective resolving time of the coincidence circuit. Although the actual resolving time of the diode coincidence circuit is about 2 μsec, the signals being fed to the discriminators are correlated over a longer period of time since they are generated by integrating the primary photomultiplier signal over 4 to 8 microseconds. The effective resolving time is approximately 8 μsec since pulses of minimum width in different channels can still register a coincidence when separated by this amount.

When the discriminators are set to trigger at a level equal to 4 standard deviations of noise at this point in the amplifier chain, $x/\sigma = 4$, and

$R_L \approx 60$ counts/sec

$R_H \approx .14$ counts/sec

and therefore $R_M \approx 10^{-4}$ counts/sec = 4 counts/hour. When the discriminators are raised to $x/\sigma = 5$,

$R_L \approx 0.9$ counts/sec

$R_H \approx 0.07$ counts/sec

and $R_M \approx 8 \times 10^{-6}$ counts/sec = 1 count every 35 hours. Clearly an optimum discriminator setting occurs somewhere between $x/\sigma = 4$ and 5.

This analysis illustrates how critically the accidental triggering rate depends on discriminator setting. The sensitivity of the system to signal pulses however does not depend strongly on discriminator setting, and therefore the discriminator triggering levels may be set to yield an accidental counting rate compatible with the time available for visual scanning of the film record.

The practice of integrating the incoming signal implies that the discrimination against noise is actually made on the basis of the area of an input pulse. In a hypothetical example, if a rectangular pulse of amplitude equal to n standard deviations of noise and length sufficient to overlap m sampling taps passes through the delay line, the mixer output will be a pulse of approximately triangular shape, of peak amplitude equal to $mn\sigma$, which will then trip the discriminator provided $mn\sigma > x$. For example, the RMS amplitude of the noise in the delay lines is typically 0.06 volts on a very dark night and the diode discriminators are then biased by about 0.25 volts

to yield a trigger level near $x/\sigma = 4$. In these circumstances a light signal corresponding in amplitude to only one standard deviation of noise will be sufficient to trigger the recording system provided its duration is greater than 4 microseconds in at least two adjacent channels.

In practice the brightness of the night sky may vary by as much as a factor of 4 from night to night, and the discrimination levels must then be adjusted by a factor of 2 to retain the same x/σ and hence the same accidental trigger rate. Furthermore, it has been found that even when the discrimination levels are set very conservatively ($x/\sigma = 5$ to 6), frequent pulses are recorded which are of sizeable amplitude but very narrow, having widths approximately equal to the amplifier response time. These fast pulses have been tentatively attributed to pulses of Cerenkov light, emitted either from small air showers in the atmosphere above the phototubes or from the cores of small air showers traversing the phototube units themselves, which have escaped the minimum pulse width requirement by virtue of their amplitude.

Another troublesome source of spurious triggers is lightning flashes in which the rise of the light intensity is fast enough to be amplified and fed to the discriminator logic. Fortunately these pulses leave a characteristic trace which is easily recognized, being typically much longer than the duration of the cathode ray tube sweeps. The question of interpreting such pulses is discussed further in Chapter 6.

A sixth amplifier channel, identical in all respects to the five phototube channels except for the photomultiplier itself, serves to signal the presence of spurious electrical pulses which may from time to time be fed into the amplifiers. Connected to this spare channel is a highly collimated photomultiplier (Dumont type 6364) which points along the horizon towards the Ithaca airport, an occasional source of fast-rising light pulses. These pulses are produced as part of an aircraft guidance system which, fortunately, is only operated in cloudy weather when the air fluorescence detector cannot be used. To ensure that such spurious pulses are not recorded, whenever the signal in this channel exceeds a discrimination level corresponding to several standard deviations of night sky noise, an anticoincidence circuit, shown in Figure 4.19, produces a gate approximately 100 milliseconds long which vetoes all master trigger pulses within this period.

The electronic discrimination system described here is of course only a partial answer to the problem of selecting probable cosmic ray fluorescence pulses. The film record must still be scanned carefully for events bearing the characteristics of a fluorescence pulse, such as a time displacement of the pulse as seen in different photomultipliers. Finally, pulses which satisfy certain criteria of likelihood are subjected to more thorough mathematical analysis.

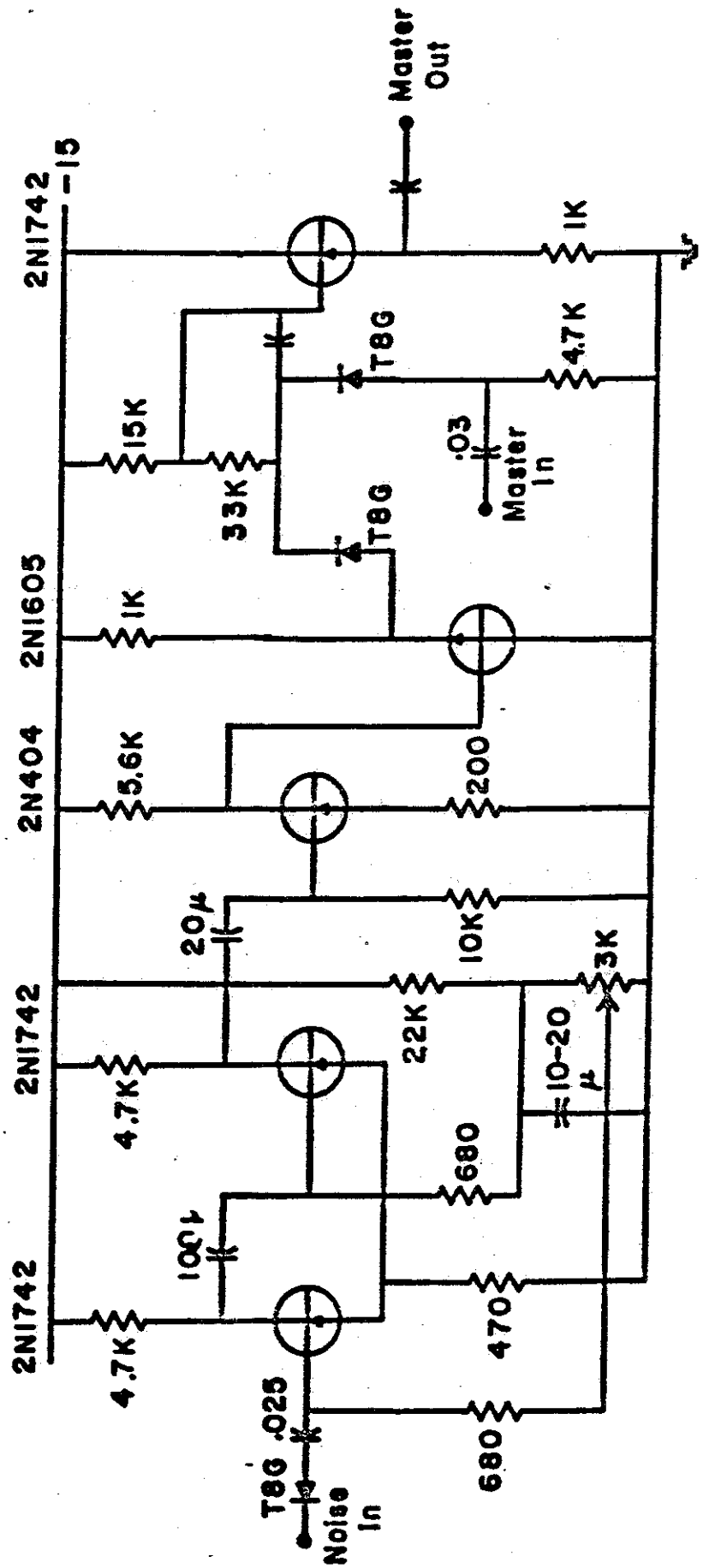

Figure 4.19 Noise Anticoincidence

Calibration -

In order to calculate the absolute intensity of a pulse of light from the recorded cathode ray deflection and hence the total energy of a cosmic ray air shower, it is necessary to know the overall sensitivity of the detector in terms of cathode ray deflection as a function of incident photon flux. This is accomplished by following each master trigger, after a delay of 100 μsec to allow the cathode ray sweep to be completed, with a light flash lasting 50 μsec from a pair of NE-51H neon lamps mounted symmetrically above the five phototube units. These lamps have been calibrated and produce a peak intensity of $6 \pm 3 \times 10^5$ photons per steradian-microsecond in the wavelength range to which the phototubes respond. This light is incident on the faces of the phototube units at an average angle of incidence of 58° and results in a pulse of photocurrent equal to 800 ± 400 photoelectrons per microsecond in the four horizontal photomultipliers, equivalent to about 6 standard deviations of night sky noise, and 1600 ± 800 photoelectrons per microsecond in the upwards-facing photomultiplier. This pulse passes through the amplifiers and is displayed on a second sweep of the cathode ray tube. After a further 100 μsec delay, a third cathode ray sweep occurs during which the amplifiers are driven into negative saturation, to provide a reference line for the measurement of pulse heights. Superimposed on this sweep are narrow positive pulses at regular 8 microsecond intervals which serve as time calibration markers.

It is important that these time markers are fed into all amplifier channels before the delay lines since small differences in the delay time of the different delay lines could otherwise spoil the time calibration between channels.

The three cathode ray tube sweeps are then recorded superimposed on the same frame of film by the camera, whose shutter remains open, before the film advances.

The univibrator circuits which perform the above tasks are shown in Figures 4.20 to 4.23. The complete sequence of events following the occurrence of a master trigger pulse, as outlined schematically in Figure 4.20, is then as follows:

In order that slow-rising pulses which trigger the discriminators late in their history still be fully recorded on film, the signals pass through a 6 μsec storage period in all channels as well as the 8 μsec delay in which the triggering decision is made. Therefore a fast pulse, which triggers the logic as it passes the 1.6 μsec coincidence gap, will appear on the cathode ray screen approximately 9 μsec after the initiation of the sweep, which occurs at the time of the master trigger. The cathode ray sweeps are 60 μsec long, which allows for the longest cosmic ray events anticipated to be fully displayed, along with segments of the normal night sky noise.

The neon calibration lamps flash 100 μsec after the master trigger, and after a further 20 μsec delay to allow the signals from this flash to pass through the delay lines, the cathode

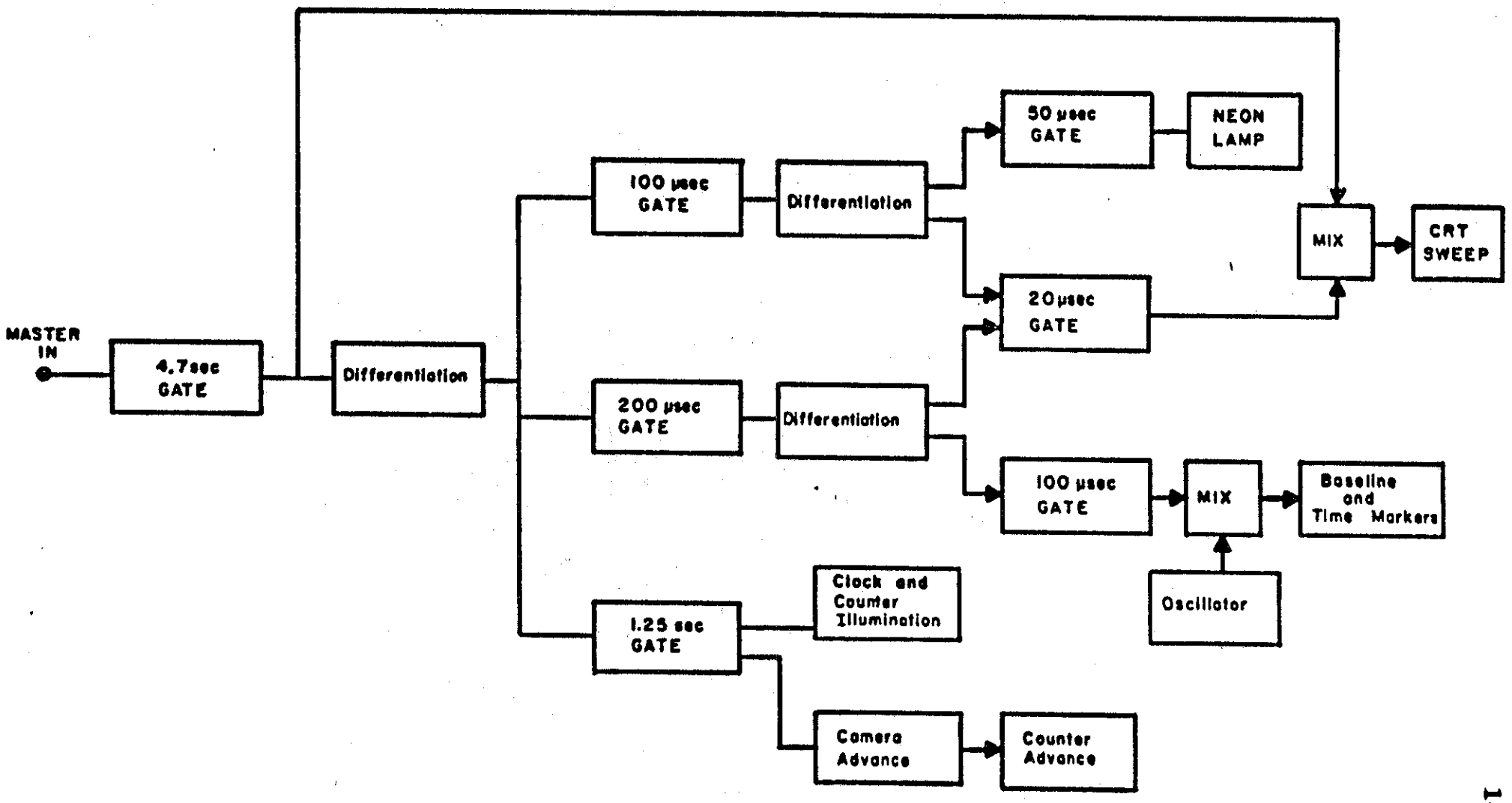

Figure 4.20 Block Diagram of Univibrator Circuits

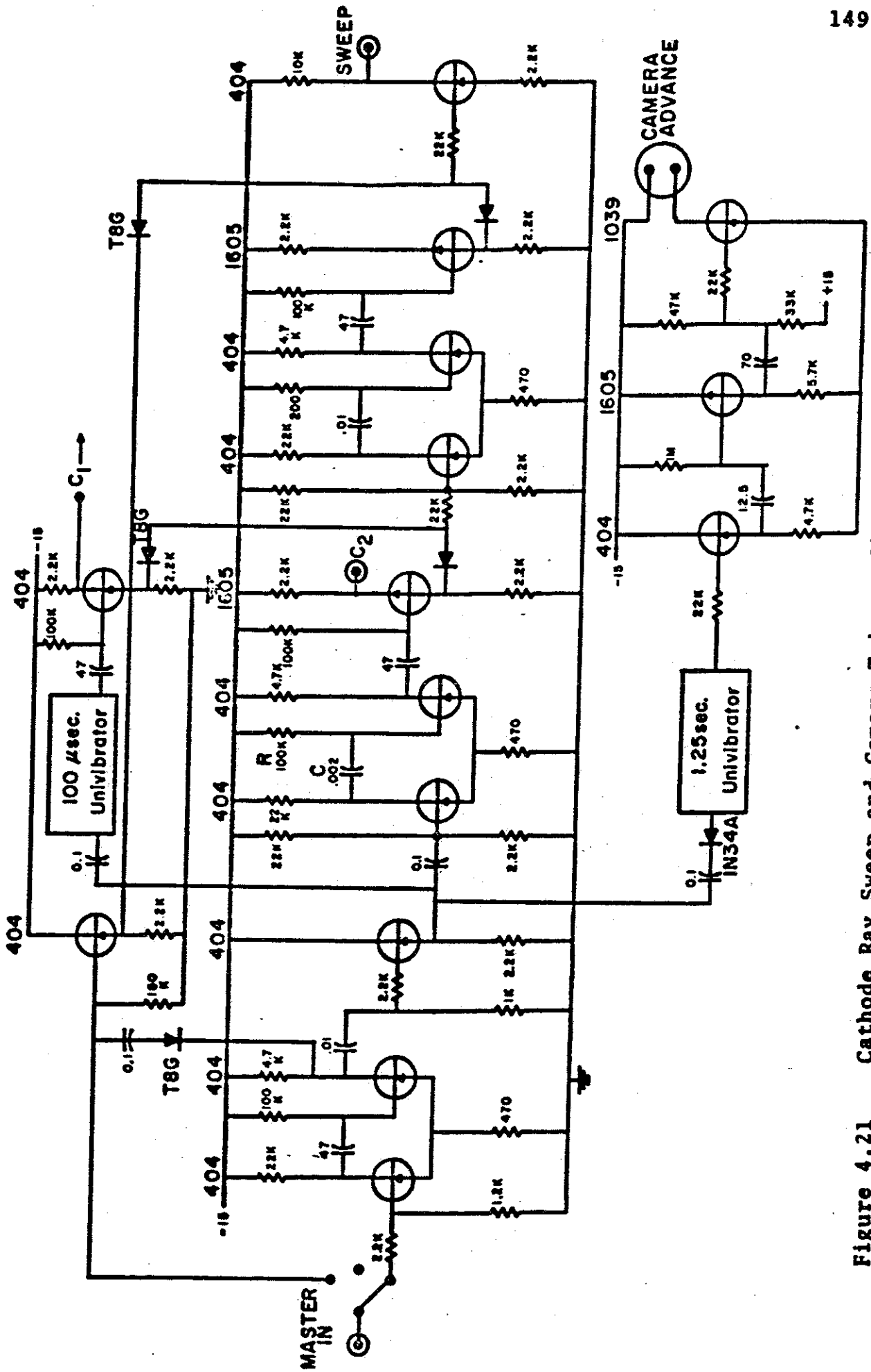

Figure 4.21 Cathode Ray Sweep and Camera Trigger Circuits

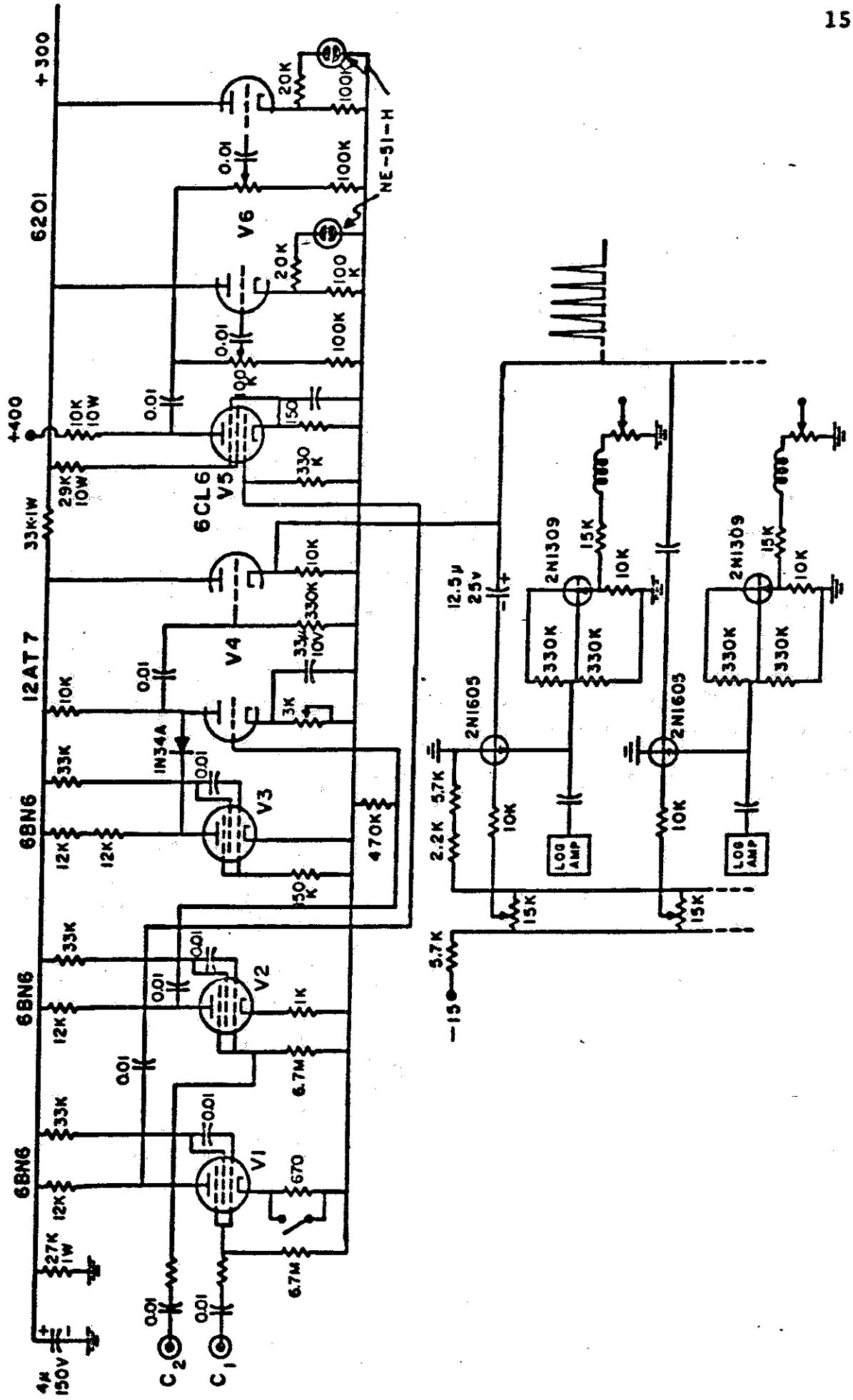

Figure 4.22 Calibration Flash and Time Marker Generator Circuits

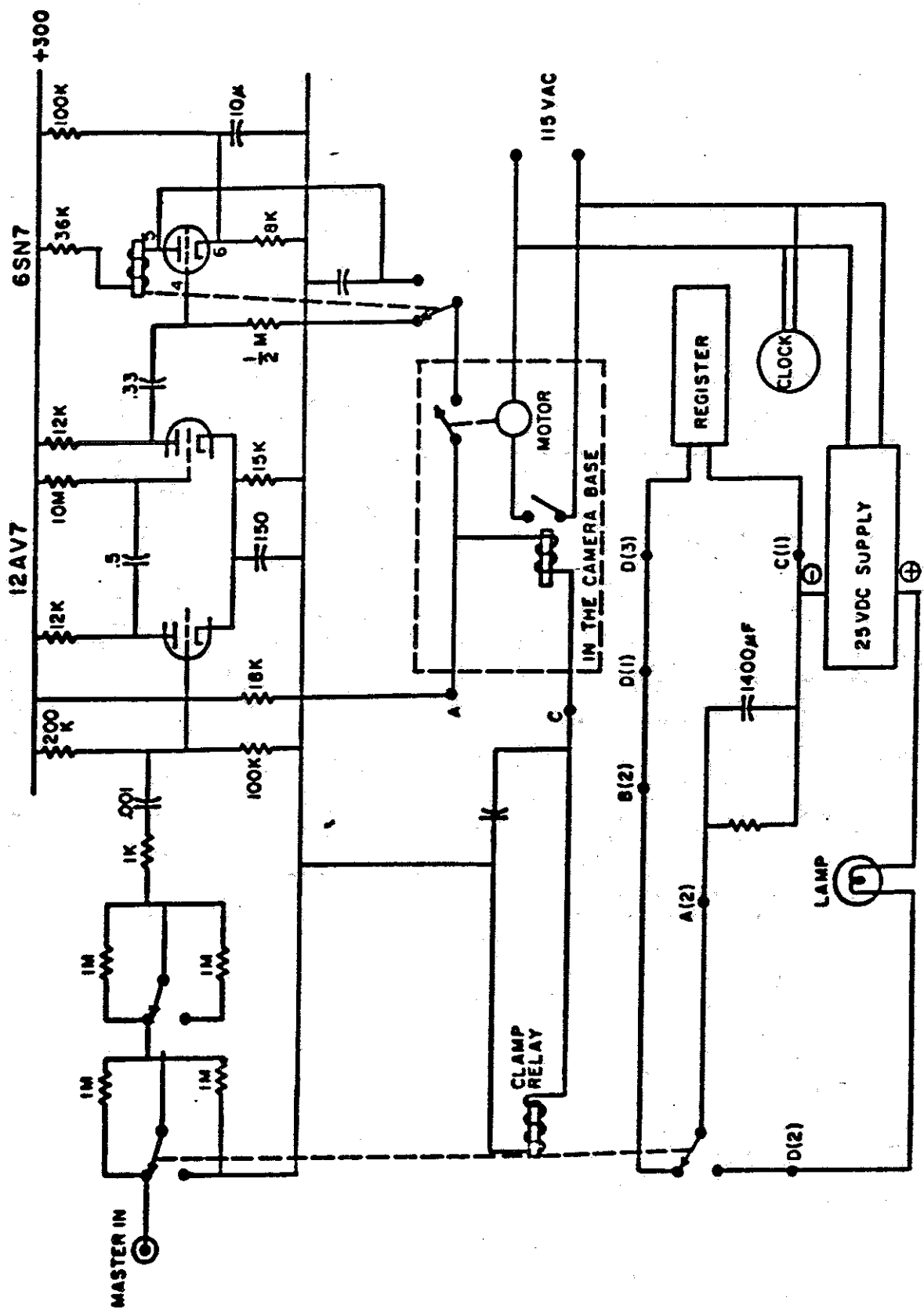

Figure 4.23 Camera Driver Circuit

ray sweeps are fired again to record most of the calibration pulse.

At 200 microseconds, a 100 μsec gate is activated which applies a large positive voltage, the opposite of normal signal polarity, to the emitter followers after the logarithmic amplifiers but before the delay lines in all channels. This gate also allows the narrow time marker pulses generated by the oscillator V_3 to be fed to the amplifiers. After a further 20 μsec delay to allow this baseline pulse to pass through the delay lines, the third cathode ray sweep is triggered.

At an elapsed time of about 1 second after the master trigger a pulse is applied to the camera circuits which, in succession, flashes a lamp within the camera box to illuminate the clock and counting register, advances the film by one frame, and advances the counter by one.

During this sequence of events a 5 second gate, generated by the master trigger, prevents other pulses from entering the univibrator circuits.. Thus the recording system has a dead time of 5 seconds.

Accessory Equipment -

In view of the large distance (24 cm) in the K1328 photomultiplier tube between the photocathode and the first dynode the question arose whether the collection efficiency for photoelectrons would be decreased by the deflecting effect of the earth's magnetic field. Tests carried out in the laboratory

indicated that an improvement in signal of up to 50% might be gained by the application of external magnetic fields. The most straightforward solution to this problem is to apply a field so as to cancel as well as possible the earth's field. For this reason, a pair of Helmholtz coils with a separation of one meter were constructed at the first detector station, surrounding the five phototubes as shown in Figure 4.1, each consisting of a single square turn carrying a direct current of 60 amperes, thus producing a field approximately equal and opposite to the earth's field at the center of the geometry.

In practice the effect of the Helmholtz coils was inconsistent, raising the gain of some units while decreasing the gain of others. At least part of this effect may have been due to the fact that the phototube containers were made of galvanized iron and thus allowed the possibility of eddy currents and remnant magnetic fields disturbing the collection of photoelectrons. Furthermore, when it was found that even a 4% (0.2 volts) 60-cycle ripple in the coil current induced a sizeable 60-cycle signal in the amplifiers, the use of the Helmholtz coil was abandoned.

For the protection of the photomultipliers against damage due to an unexpected flood of light, two safety devices were incorporated into the automatic switching controls for the phototube high voltage, a photoresistor switch and a pulse integrator switch. These circuits are shown in Figures 4.24 and 4.25. The pulse integrator circuit uses a univibrator to feed a standard 17 volt, 400 microsecond square pulse to a

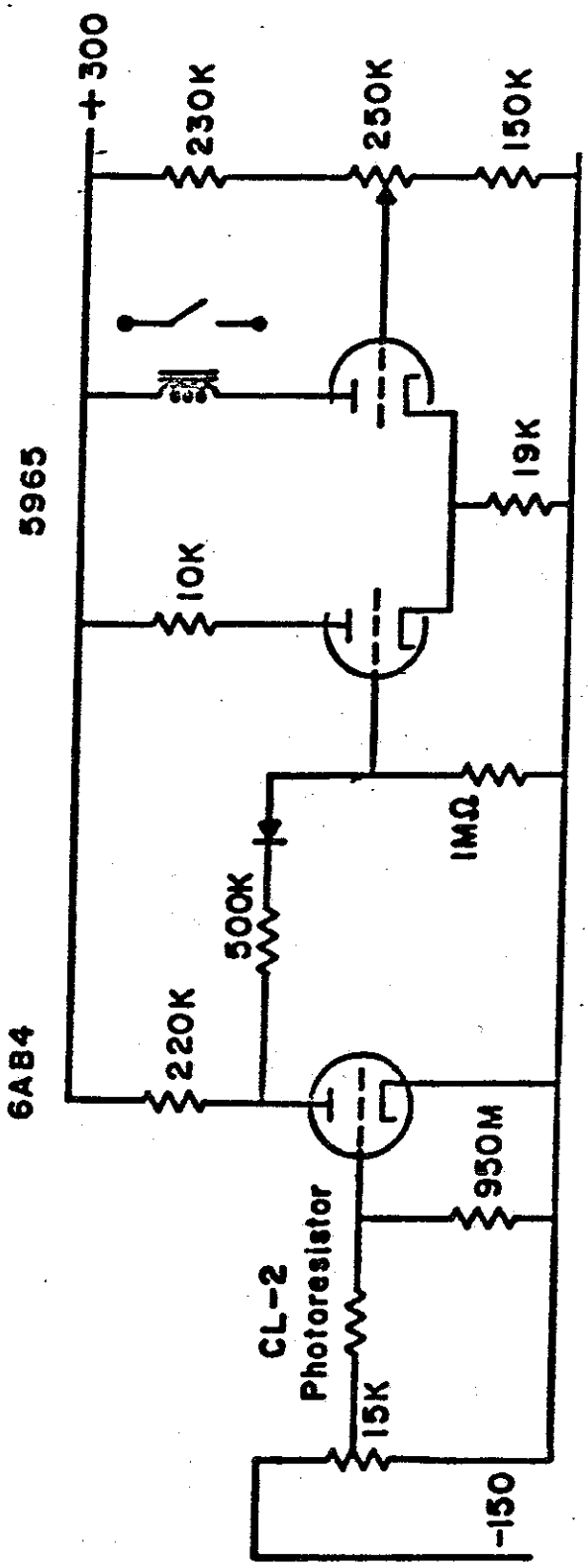

Figure 4.24 Photoresistor High Voltage Switch

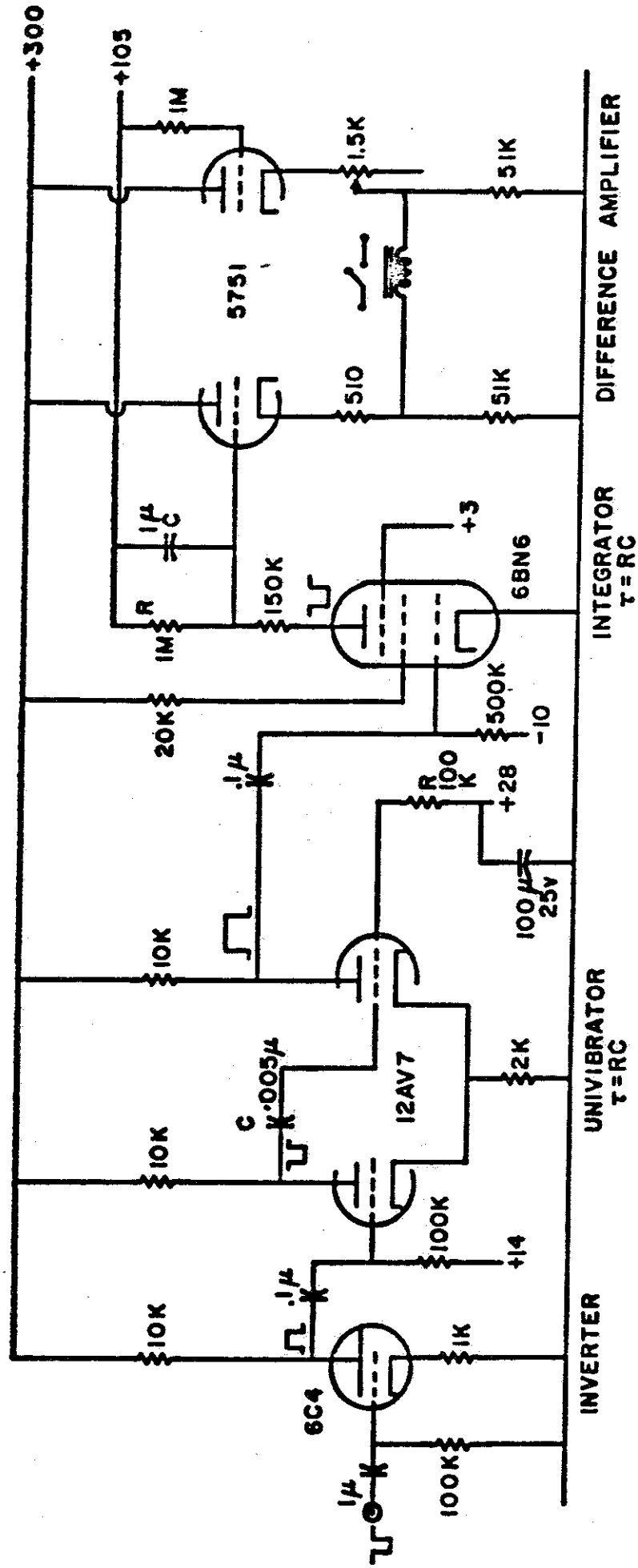

PULSE INTEGRATING CIRCUIT

Figure 4.25

charging circuit whenever a "High" output pulse is produced in the discriminator logic of any of the five channels. A difference amplifier then senses the charge on a 1 microfarad capacitor and switches the high voltage off the photomultipliers whenever the total "High" trigger rate in the five channels rises above 300 counts per second. A thermal delay relay holds the high voltage off for 45 seconds, after which time the voltage switches on again.

The photomultiplier supply itself (Figure 4.26) remains on permanently in order to avoid transient warm-up effects and thus a variability in photomultiplier gain, while high voltage relays perform the switching between the phototubes and a set of 5-megohm dummy loads. In parallel with these relays is an additional switching relay which disconnects the master pulse from the univibrator circuits, thus allowing master triggers to occur only when the photomultiplier high voltages are on and further reducing the number of spurious events recorded.

The photocathodes are protected from direct sunlight during the daytime by opaque mylar shutters which are clock-controlled to be drawn open at sunset and closed again before dawn. A second 24-hour clock turns on and off the phototube high voltages at times consistent with a twilight period and the rising or setting time of the moon. It has been found that approximately 80 minutes of twilight must be allowed before the night sky reaches near minimum brightness, and similarly 10 minutes of lunar twilight must be allowed during

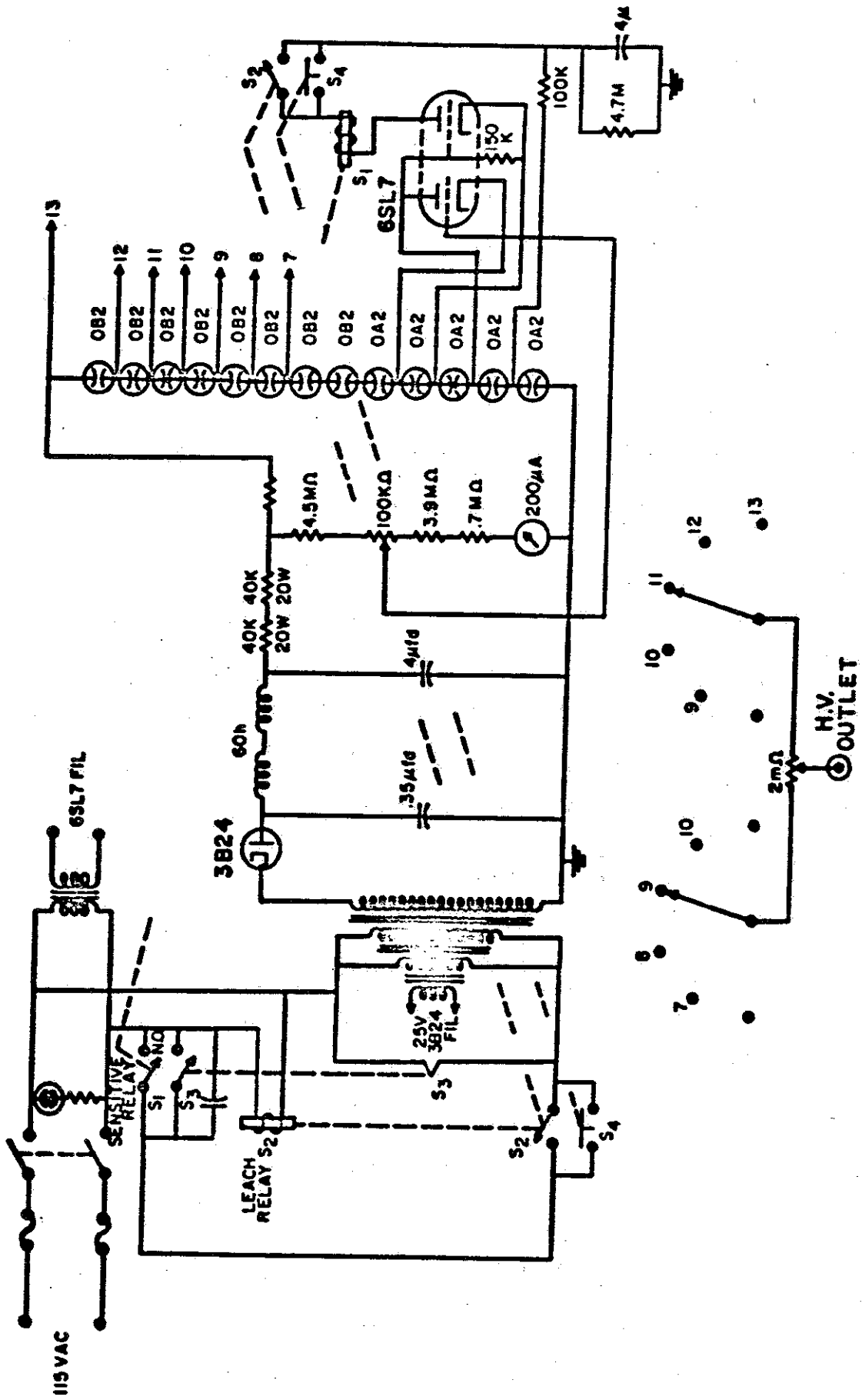

Figure 4.26 Photomultiplier Tube High Voltage Power Supply

most of the lunar cycle.

The photoresistor switch provides additional security against mishaps by switching off the photomultiplier high voltages whenever the background light approaches twilight intensity and holding the high voltages off for as long as the brightness remains. This feature is particularly designed against headlights of automobiles which may park near the station, and power failures which may disable the clock switches.

In order to provide a permanent record of the periods in which the photomultipliers are operating, and also to provide an hour-by-hour record of the background night sky brightness, a linear amplifier circuit with a time constant of about 10 milliseconds, shown in Figure 4.27, drives a graphical recorder with a signal proportional to the average RMS anode current (and thus proportional to the square root of the sky brightness) in one chosen phototube channel.

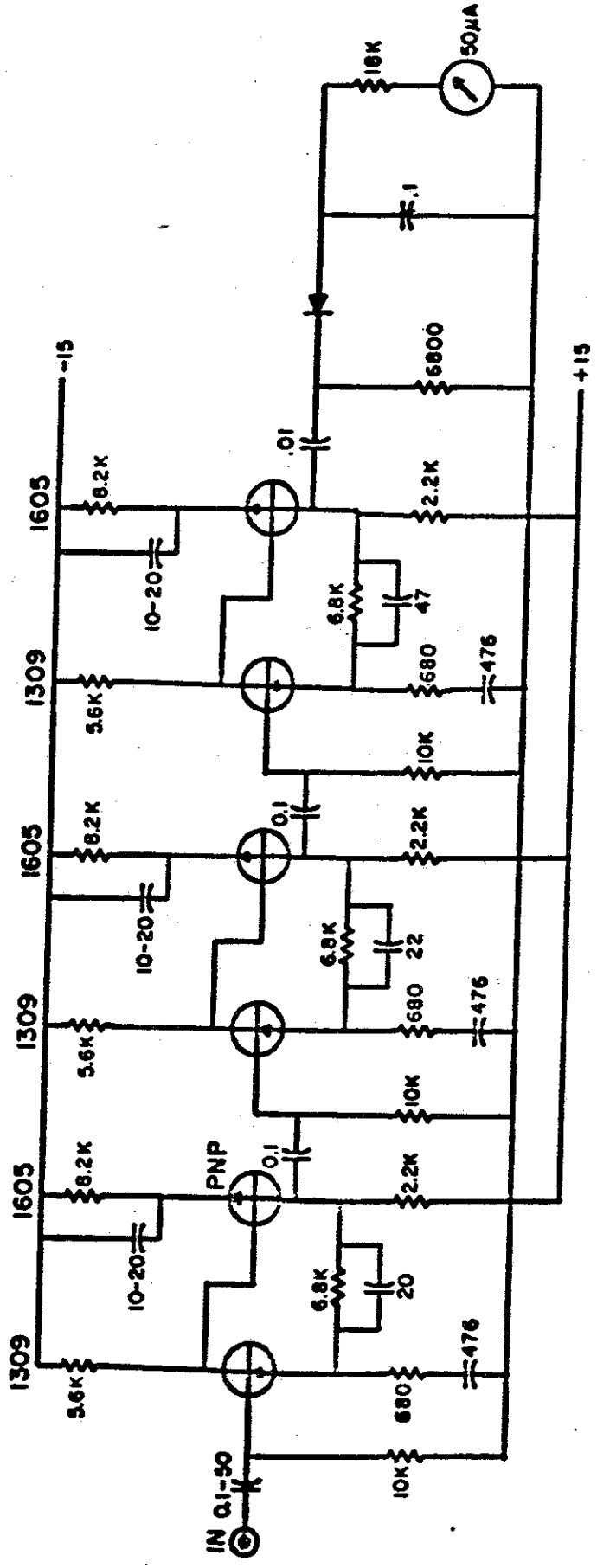

Figure 4.27 Anode Current Recorder

Chapter 5

THEORY OF ANALYSIS

The observation of the fluorescence signal in principle allows the determination of 6 independent parameters plus two functions for an air shower event. Four of these parameters describe the geometrical position of the shower axis, one describes the time of the event, one gives the total energy dissipated, and two functions describe the lateral and longitudinal development of the shower. The fluorescence technique appears to be incapable of measuring the proportion of muons or the nucleon component, since the signal is essentially all due to secondary electrons. Also, since the relatively rare very high energy events that this technique is suited to detect will occur at distances typically several kilometers from a detector, there is little hope, or indeed little advantage, in attempting to resolve the lateral structure of the showers. As we shall see in this chapter, the presence of an obscuring noise with the signals limits the effective angular resolution in the preliminary experiment described here to about 10 to 20 degrees at best, and we shall henceforth consider the lateral distribution function unmeasurable, approximating the shower path by a straight line.

The determination of the geometrical position of the shower is important for two distinct reasons: First of all, knowledge of the geometry is essential for calculation of the total energy of the shower and for calculation of the frequency of

events per unit area, after a number of showers have been recorded. Secondly, the azimuth and altitude of the "vanishing point" of the shower axis, along with the time at which the event occurs, give the direction of the primary particle in celestial co-ordinates, which is important in answering questions concerning isotropy.

The four geometrical parameters necessary to fix the position of the shower axis may be chosen in different ways. For example, the shower-detector plane may be described by two direction cosines of a vector orthogonal to the plane (see Figure 2.15) and the position of the shower axis in the plane by the "impact parameter" R and the angle ψ in the shower-detector plane made by the shower axis with a horizontal plane through the detector (see Figure 5.1).

Analysis of Noiseless Signals -

Consider now the reception of a perfectly noiseless air shower fluorescence signal by the 5-channel detector described in Chapter 4. Let us assume that at any instant the light source is seen by 3 adjacent channels, one of which is the up-pointing channel. From equation (4.11), the angles of incidence can be calculated from the calibrated signal amplitudes S_1, S_2, S_u, by

$$\left.\begin{aligned} \cos\theta_1 &\propto (S_1)^{1/p} \\ \cos\theta_2 &\propto (S_2)^{1/p} \\ \cos\theta_u &\propto (S_u)^{1/p} \end{aligned}\right\} \qquad (5.1)$$

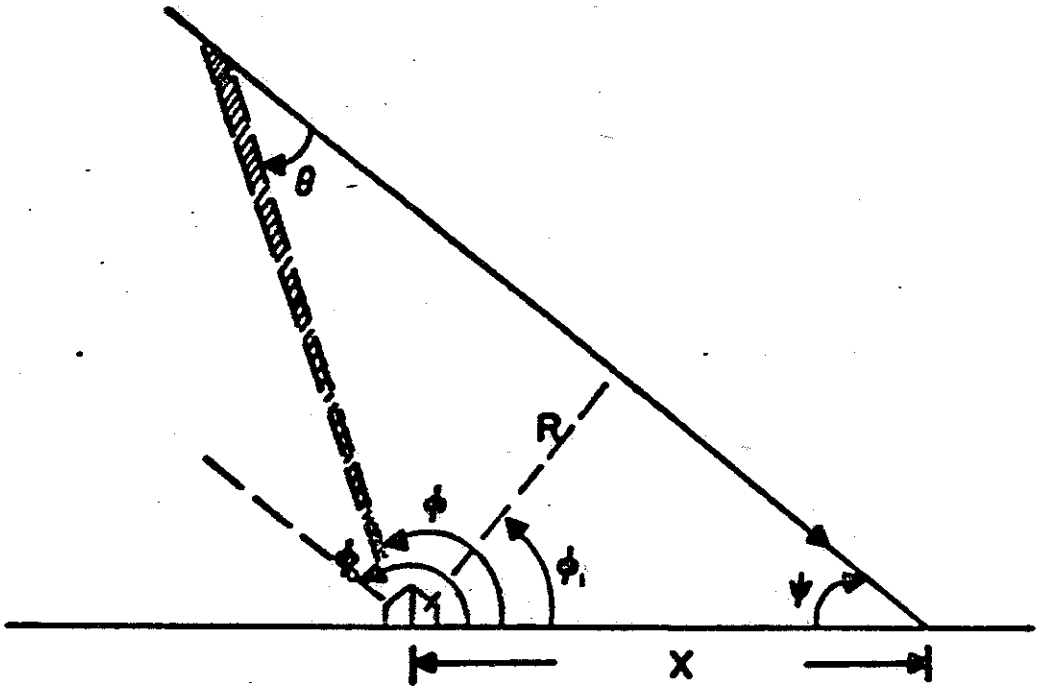

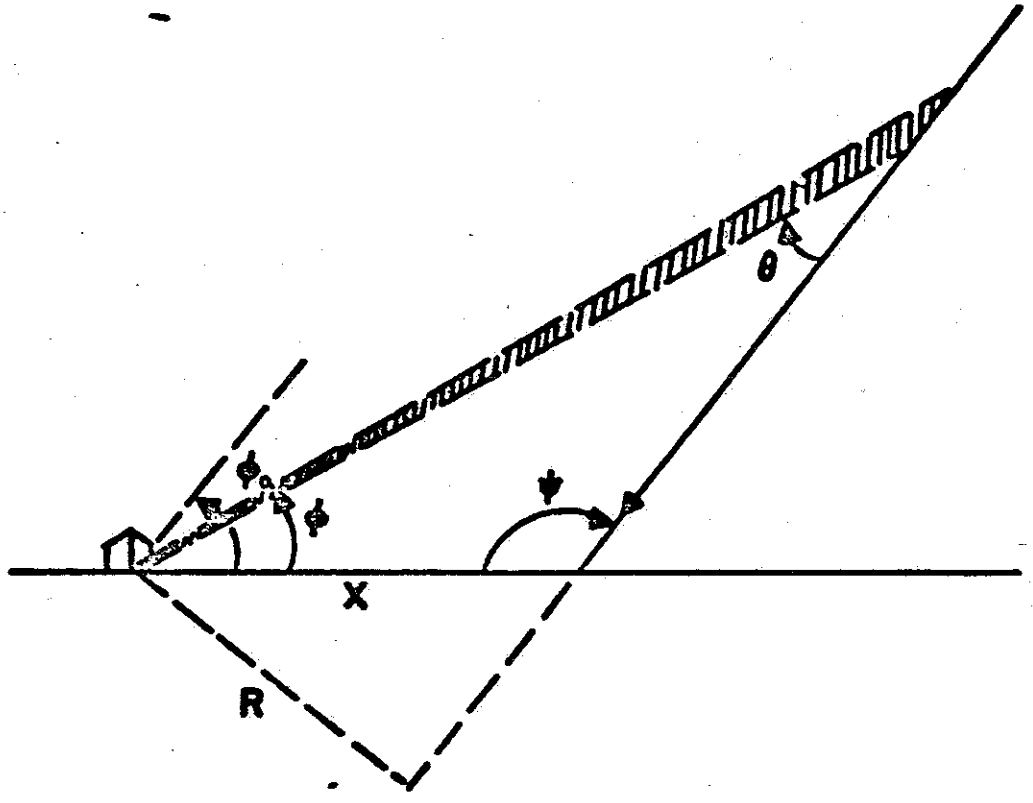

Figure 5.1

where the subscript u refers to the up-pointing channel.

The altitude angle a and azimuth m within the appropriate quadrant of the light source at any instant can then be found by application of spherical trigonometry:

$$\cos \theta_u = \sin a \qquad (5.2)$$

$$\cos \theta_1 = \sin m \cdot \cos (a-30) \qquad (5.3)$$

$$\cos \theta_2 = \cos m \cdot \cos (a-30) \qquad (5.4)$$

where 30^o is the angle of elevation of the horizontal tubes. Therefore

$$\tan m = \frac{\cos \theta_1}{\cos \theta_2} = \left(\frac{S_1}{S_2}\right)^{1/p}, \qquad (5.5)$$

and

$$\frac{\cos(a-30)}{\sin a} = \left[\left(\frac{\cos \theta_1}{\cos \theta_u}\right)^2 + \left(\frac{\cos \theta_2}{\cos \theta_u}\right)^2\right]^{1/2}$$

$$= \left[\left(\frac{S_1}{S_u}\right)^{2/p} + \left(\frac{S_2}{S_u}\right)^{2/p}\right]^{1/2}, \qquad (5.6)$$

which can be solved for the altitude a.

If more than 3 channels view the light source, the position is over-determined and different combinations of 3 signals can be considered for independent determinations of a and m.

To an observer, the linear shower axis appears as a section of a great circle. Thus the collection of source position determinations map out the shower-detector plane directly. This plane may be described by the azimuth m_o and altitude a_o of the orthogonal vector, which can be found from

any pair of source position determinations (m_1, a_1) and (m_2, a_2) by means of the equations

$$\tan m_o = \frac{\cos m_2 \tan a_1 - \cos m_1 \tan a_2}{\sin m_1 \tan a_2 - \sin m_2 \tan a_1} \tag{5.7}$$

and

$$\tan a_o = -\frac{\cos(m_o - m_1)}{\tan a_1} = -\frac{\cos(m_o - m_2)}{\tan a_2} \quad . \tag{5.8}$$

Continuing our noiseless signal analysis, we may consider the measurements as a series of determinations of the angle ϕ in the shower-detector plane between the horizon and the light source, measured from the direction of the impact point, as a function of time (see Figure 5.1).

The angle ϕ from which the first photon is received, call it ϕ_o, gives the parameter ψ directly, if we can ignore the finite thickness of the atmosphere, since

$$\psi = 180^o - \phi_o \tag{5.9}$$

(In practice the air shower is not initiated for a depth of typically 50 gm/cm^2, which may correspond to an altitude as low as 20 km, so that this determination of ψ, even with perfect detection capabilities, could be gravely in error.)

In order to determine the impact parameter R, we make use of equation (2.79) and note that

$$\theta + \phi = 180 - \psi = \text{constant.} \tag{5.10}$$

Therefore

$$\frac{d\phi}{dt} = \frac{-d\theta}{dt} \quad , \tag{5.11}$$

and

$$\frac{d\phi}{dt} = \frac{-c}{R}(1 + \cos\theta), \tag{5.12}$$

from which

$$\frac{d^2\phi}{dt^2} = \frac{-c}{R}\sin\theta\,\frac{d\phi}{dt} = \frac{c^2}{R^2}\sin\theta\,(1+\cos\theta), \tag{5.13}$$

leading to

$$R = -2c\left[\frac{\left(\frac{d\phi}{dt}\right)^3}{\left(\frac{d\phi}{dt}\right)^4 + \left(\frac{d^2\phi}{dt^2}\right)^2}\right], \tag{5.14}$$

a quantity which can be determined in principle from each set of three successive measurements of ϕ.

It should be noted also that the parameter R can be found more accurately by measurement of the initial value of $\frac{d\phi}{dt}$, since

$$\lim_{t\to 0}\ \frac{d\phi}{dt} = \frac{-2c}{R}\ . \tag{5.15}$$

Furthermore, this represents a maximum value for $\left|\frac{d\phi}{dt}\right|$ and the latter does not change rapidly with time near t = 0. In practice this derivative may be evaluated at the earliest time in the shower when the signals are large enough to permit some precision.

The parameter ψ can be found, knowing the value of R, from every determination of $\frac{d\phi}{dt}$, since by inverting equation (5.12), we have

$$\psi = \cos^{-1}\left(1 + \frac{R}{c}\frac{d\phi}{dt}\right) - \phi \tag{5.16}$$

Note that for "receding" showers, ψ must fall in the range $0 \le \psi < 90^\circ$, whereas for "approaching" showers we have $90^\circ \le \psi < 180^\circ$. These two cases are defined by whether or not

the shower reaches closest approach before striking the ground (see page 78), and can be distinguished observationally simply by observing whether the full range of values of ϕ ($=\phi_o$) is greater or less than 90^o.

The variation of $\frac{-d\phi}{dt}$ with the observed angle ϕ is shown in Figure 5.2, where $\frac{-d\phi}{dt}$ is plotted in units of c/R. It may be noted that ψ is equal to $180^o - \phi_o$, where ϕ_o is the value of ϕ for which $\frac{-d\phi}{dt} = 2\frac{c}{R}$.

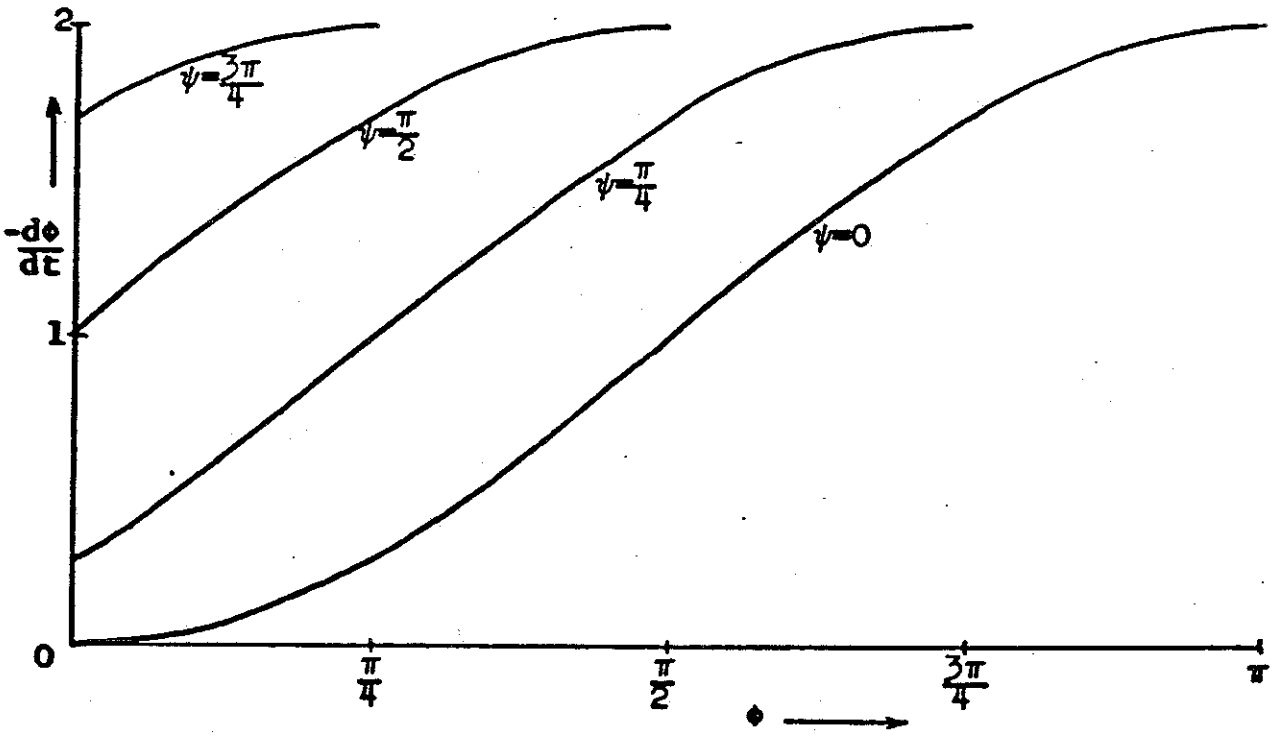

Figure 5.2

In practice, the determination of ψ is most difficult for approaching showers because of the limited range of values of ϕ for which measurements can be made. An approximation can be considered which makes use of the fact that the time

compression of the signal from an approaching shower allows little error to enter from the finite thickness of the atmosphere. From Equation (2.83), the total pulse width Δt in this case is given by

$$c\ \Delta t = x - \sqrt{x^2 - R^2} \tag{5.17}$$

where

$$x = \frac{R}{\sin\psi} \tag{5.18}$$

so that if the signal pulse width Δt is measured, we have

$$\frac{1 + \cos\psi}{\sin\psi} = \cot\frac{\psi}{2} = \frac{c\ \Delta t}{R} \quad , \tag{5.19}$$

which can be solved for ψ. (The above equation is also true for receding showers.)

Once the values of R and ψ and the angles defining the shower-detector plane are known, the longitudinal shower function can be determined from the recorded signal amplitude function. As in Equations (2.84) to (2.86), let $F(\phi)$ be the signal amplitude at the detector in photons/cm^2-sec, as a function of the measured angle ϕ. Then the following relations hold:

$$\cos\theta = -\cos(\psi + \phi) \tag{5.20}$$

$$\sin\theta = \sin(\psi + \phi) \tag{5.21}$$

$$\text{altitude } z = \frac{R \sin\phi \cos\beta}{\sin(\psi+\phi)} \tag{5.22}$$

where β is the angle made by the shower-detector plane with the zenith (equals the altitude angle of the orthogonal vector).

Then, from equation (2.86), the fluorescent yield $Y(z)$ in photons per cm is given by

$$Y\left(\frac{R \sin\phi \cos\beta}{\sin(\psi+\phi)}\right) = \frac{4\pi R^2 F(\phi)}{\left[1 - \cos(\psi+\phi)\right] e^{\frac{-kR}{\sin(\psi+\phi)}}} \qquad (5.23)$$

and the number of secondary particles $N(E_o,t)$ at a depth

$$t = \frac{1}{\cos\zeta} \int_z^\infty \rho(z)dz \qquad gm/cm^2 \qquad (5.24)$$

is found from Equation (2.75):

$$N(E_o,t) = \frac{RT_o \left(1 - \frac{az}{T_o}\right)^{1/2} Y(z)}{qM \sum_i \left(\frac{\lambda_i}{.0124}\right) P_i'(T_o)\, E(\lambda_i)} \quad , \qquad (5.25)$$

where the R in this equation is the gas constant.

The zenith angle ζ of the shower axis can be expressed in terms of parameters above and is given by

$$\cos\zeta = \sin\psi \cos\beta \quad . \qquad (5.26)$$

The determination of the initial energy E_o of the primary particle follows from the secondary particle function $N(E_o,t)$ through an approximate relationship between E_o and the number of secondary particles at shower maximum found from theoretical electronuclear cascade calculations (2,79,106,107), namely

$$E_o(ev) \approx 2 \times 10^9 \left[N(E_o,t)\right]_{max} \qquad (5.27)$$

or, more directly, from an extrapolated integral along the entire shower path

$$E_o = \int_o^\infty \frac{Y(z)}{E(z)}\, ds \quad , \qquad (5.28)$$

where $E(z)$ is the conversion efficiency of the fluorescence process (equation 2.68), and the extrapolation is made to

include the energy dissipated after the shower strikes the ground, as well as correcting for the energy given to neutrinos and high energy muons.

Equation (5.28) is particularly to be preferred over semi-empirical relationships such as (5.27) since the validity of conventional cascade theory is not well established. Indeed, as we have pointed out earlier, the air fluorescence technique in principle offers a test of theories for very high energy longitudinal shower development.

Analysis of Signals with Noise -

The inevitable presence of noise due to photoelectron statistics seriously affects the foregoing analysis. E. Jenkins, in his thesis (90), has studied in detail the way in which the background limits the accurate determination of the parameters of an event. We shall briefly mention some of the conclusions of this study, as well as touching on Jenkins' method of maximum data extraction.

Figure 5.3 shows four of Jenkins' computer-simulated air shower events, as they would be recorded with this 5-channel detector, to illustrate the expected pulse shapes. The parameters of these events are as follows:

(a) $R = 3$ km, $E_o = 5 \times 10^{19}$ ev, $\psi = 56^\circ$, $\beta = 25^\circ$

(b) $R = 3$ km, $E_o = 5 \times 10^{19}$ ev, $\psi = 30^\circ$, $\beta = 0^\circ$

(c) $R = 3$ km, $E_o = 5 \times 10^{19}$ ev, $\psi = 90^\circ$, $\beta = 0^\circ$

(d) $R = 7$ km, $E_o = 2 \times 10^{20}$ ev, $\psi = 27^\circ$, $\beta = 14^\circ$

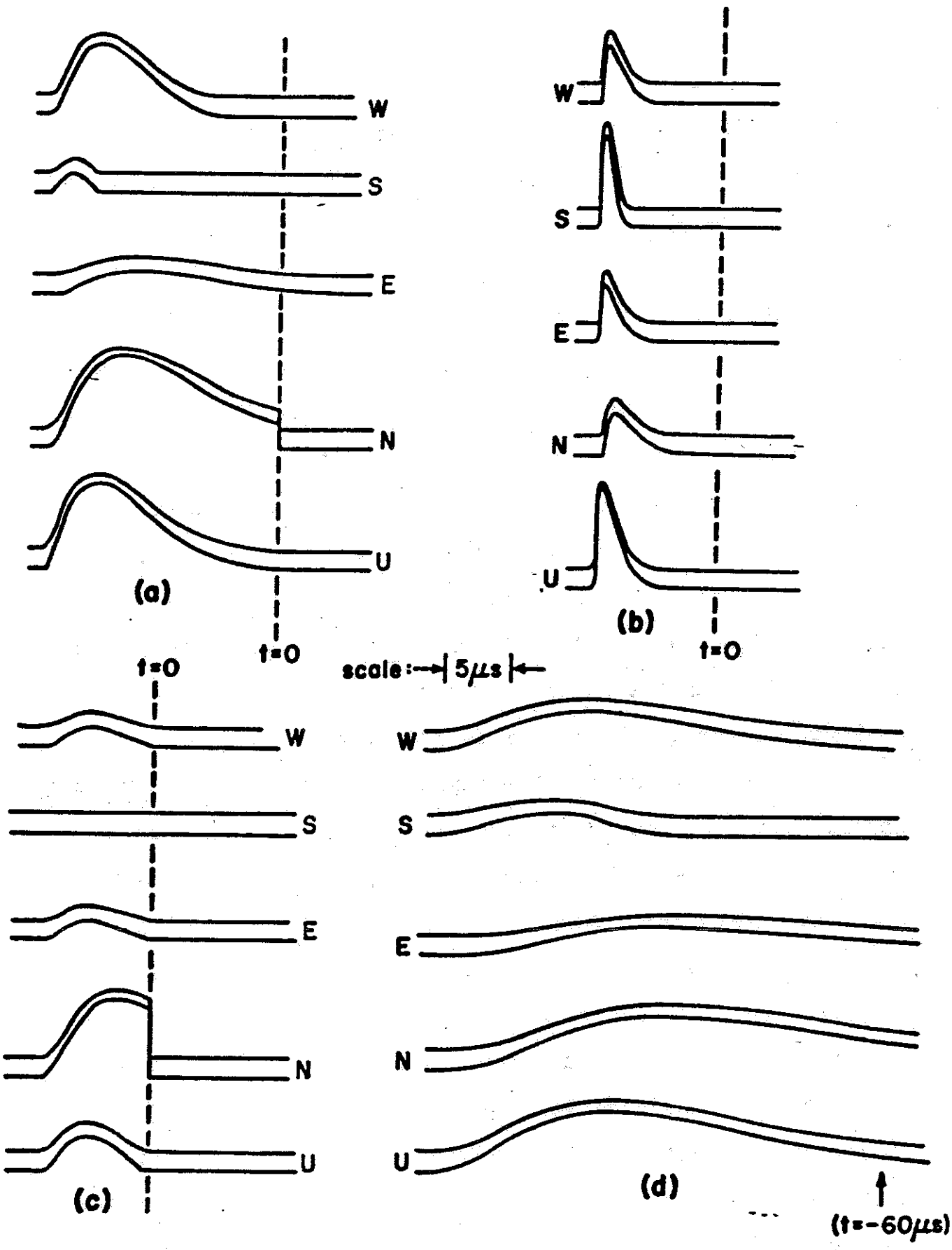

Figure 5.3 Four Simulated Air Shower Events

Events (a), (b) and (d) are "receding" showers, while event (c) is a vertical shower striking the ground at closest approach. The double lines indicate the envelope of the signal plus and minus one standard deviation of noise. The dotted lines show the time of reception of the signal from the point of impact with the ground. For event (d) this time occurs ~60 micro-seconds after the point marked.

One of the first consequences of the desire to deal with signal-to-noise ratios (as defined in Chapter 3) in the range from one to ten is the need for a finite electrical bandwidth in the recording apparatus, and hence a limited number of possible independent signal amplitude measurements. This requirement, together with the additional complication of a Cerenkov light contribution at small impact parameters, sets a lower limit to the distance at which showers can be accurately analyzed of about 1 kilometer in this experiment.

At larger distances, the signal pulse widths are generally longer, and the more independent measurements of the angle ϕ in excess of three, the more accurately the shower-detector plane is determined. Jenkins makes use of the known RMS amplitude of the background noise (derived in Chapter 3) to calculate the probable error in the signal amplitude for each channel, which leads to a two-dimensional probability distribution for the azimuth-altitude co-ordinates of the light source at any instant. The probable error in each source position is inversely dependent on the signal-to-noise ratio in the channel with the strongest signal, and is about 10^{o}

for S/N = 10, but is 90° (completely indeterminate) for S/N < 5.

However, the position of the shower-detector plane may be determined by a calculation analogous to a least squares fit among the individual source position determinations, leading to a probable error in the orthogonal vector which is roughly inversely proportional to the quality factor Q (discussed in Chapter 3) and is about 5° for Q = 30.

Therefore the presence of noise still allows the shower-detector plane to be fixed without serious error provided the quality factor Q is greater than about 15. On the other hand, determination of the position of the shower axis within the plane depends on effectively calculating the quantities $\frac{d\phi}{dt}$ and $\frac{d^2\phi}{dt^2}$ for which the probable error due to the presence of noise is significantly greater, not only because more determinations of ϕ are required to compute quantities depending on the higher derivatives, but also because the finite resolving time of the detector makes the higher derivatives become less independent between successive readings. Jenkins has applied the technique of probability analysis to two simulated air shower events, shown in Figures 5.4 and 5.5, both of the "receding" class, generated with the addition of random noise, to find the following standard errors in the determination of R and ψ:

Table 5.1

Event	Q-value	Standard Error in ψ	Relative Standard Error in R
(a)	27	34°	40%
(g)	22	20°	100%

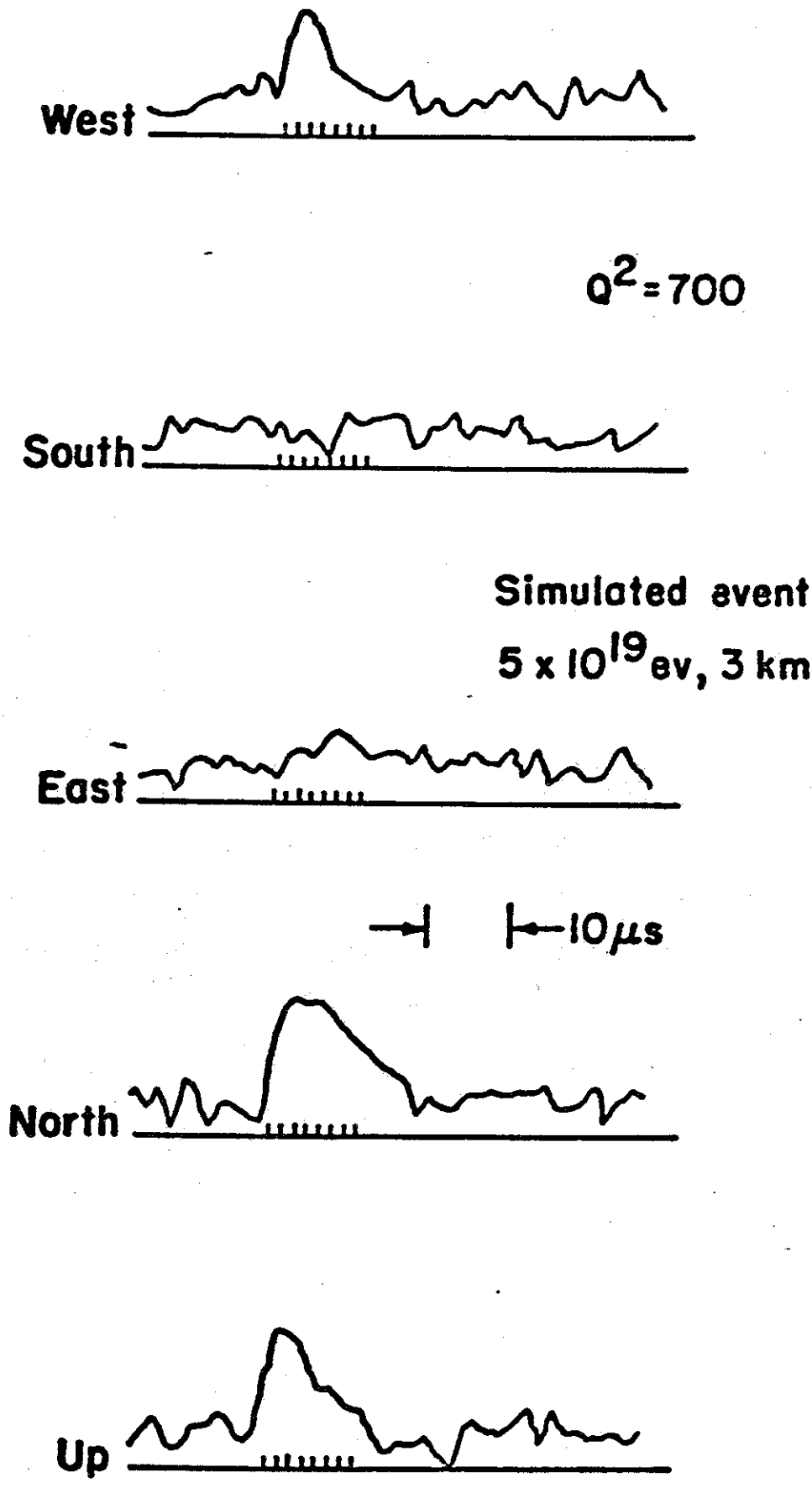
West
$Q^2 = 700$
South
Simulated event
5×10^{19} ev, 3 km
East
10 μs
North
Up

Figure 5.4

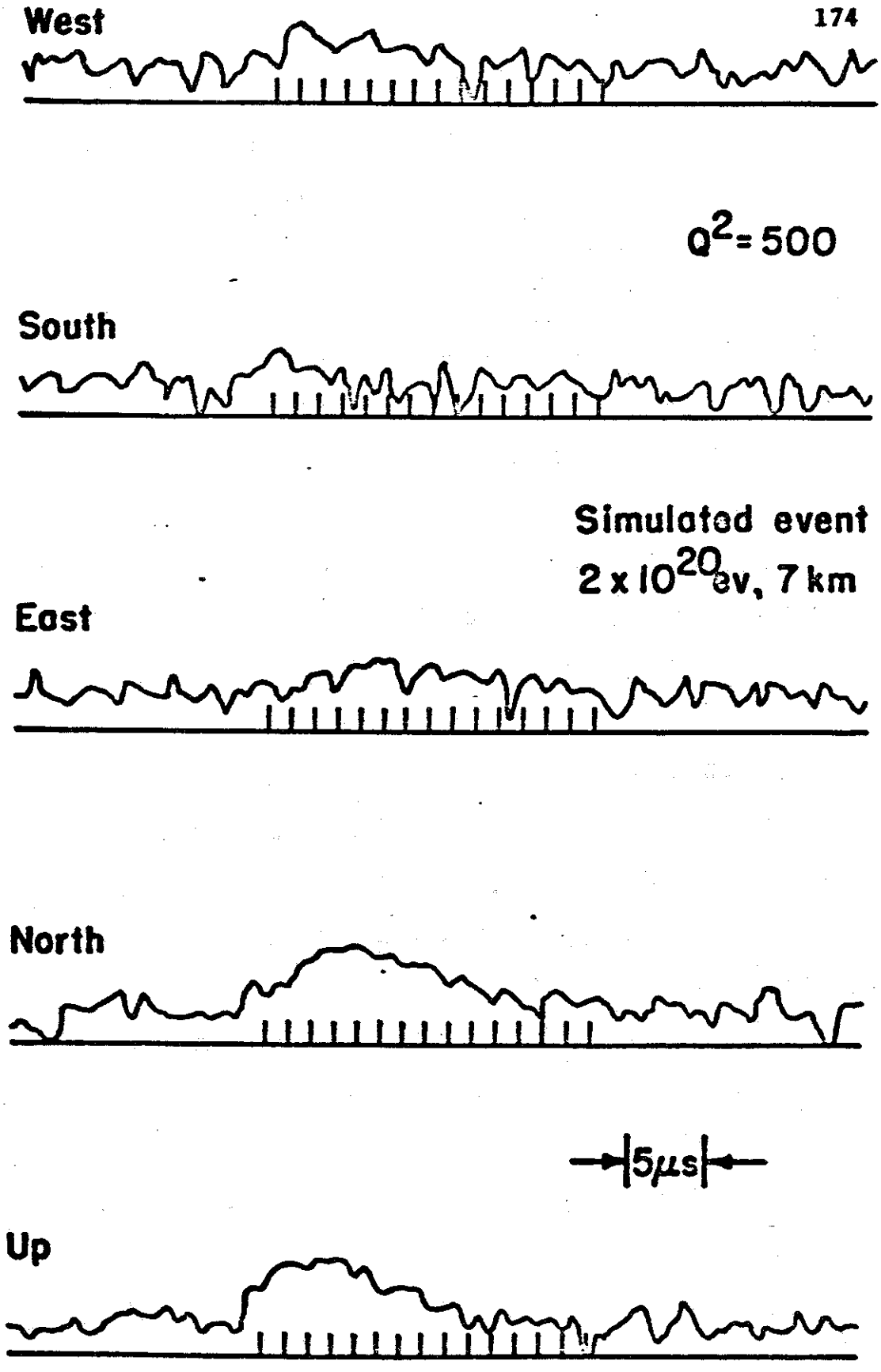
West
$Q^2 = 500$
South
Simulated event
2×10^{20} ev, 7 km
East
North
5μs
Up

Figure 5.5

The probability distribution for R and ψ is highly non-Gaussian. There is a strong correlation between R and ψ because knowledge of $\frac{d^2\phi}{dt^2}$ is in principle required to determine either parameter, whereas once one parameter is determined, knowledge of $\frac{d\phi}{dt}$ is sufficient to determine the other. Accuracy in the determination of R is required for estimation of the total energy of the shower and for estimation of the frequency of events within a given area. Accuracy in the value of ψ is important for the reconstruction of the shower curve, since the path travelled by the shower in reaching ground level depends strongly on the zenith angle.

Therefore the accuracy of the determination of the shower curve, the total energy, or the counting rate at a given energy, from data recorded at a single station, can be no better than the accuracy to which R and ψ are determined. (In practice the uncertainty in these quantities is further increased by the $\pm 30\%$ uncertainty in the fluorescent efficiency.)

If two detector stations view the same shower, however, the advantages of this stereoscopic viewing are enormous. Even with no time information whatsoever, the determinations of two shower-detector planes define a line of intersection which provides all four parameters of the shower axis itself, provided these planes do not intersect at a very small angle. Accurate relative timing between stations then allows calculation of the light yield as a function of position along the shower axis with little possible error, and thus

reconstruction of the development of the shower.

For a more thorough discussion on questions of analysis in the presence of noise the reader is referred to Jenkins' thesis (90).

Analysis of Nearby Showers -

When the impact parameter R for a shower is less than about 2 kilometers, two of the approximations made earlier are no longer valid; namely, we can no longer ignore either the lateral spread of the shower or the Cerenkov contribution to the light intensity.

The lateral distribution of secondary particles may be approximated by the function

$$\rho(N,r) = \frac{aNe^{-r/b}}{r} \quad \text{particle/m}^2 \qquad (5.29)$$

with $a \approx 2\times10^{-3}$ and $b \approx 74$ meters at sea level (2). From this we see that the density falls off by a factor of 100 between $r = 1$ meter and $r = 80$ meters, and the apparent brightness of the fluorescence falls off correspondingly rapidly. Clearly this can have little effect upon the interpretation of shower signals unless the shower comes within 500 meters at closest approach. Even in this case, however, little error is introduced into the shower analysis, since the measurement of the angle ϕ by the ratio of signal amplitudes in different channels effectively averages over the light source and still yields, to a first approximation, the position of the shower core.

The presence of the Cerenkov emission, on the other hand, requires significant modifications of the foregoing analysis for the interpretation of nearby showers and especially for nearby approaching showers. Considering the Cerenkov light alone, the geometrical analysis presented earlier in this chapter also applies to the Cerenkov light, with the single exception that the emission is anisotropic, being concentrated strongly along the direction of the particles' motion. Also, whereas the fluorescence intensity indicates the number of particles with energies over about 20 electron volts, the intensity of the Cerenkov light reflects the number of shower particles with energies above about E_T = 40 Mev. (The average threshold for the Cerenkov effect through the lower atmosphere is about 30 Mev, but the Cerenkov yield is small near the threshold, as is shown in equation 3.26.) The fraction of shower electrons with energies above 40 Mev, according to cascade theory, is about 40% (79).

The angle ξ that the emission makes with a particle trajectory is given by (27)

$$\cos \xi = \frac{1}{\beta n} \qquad (5.30)$$

where n = the index of refraction of air. The maximum value for ξ at sea level is 1.3°, and we neglect it in comparison to the angular distribution of the shower particles themselves due to multiple scattering.

Let the fraction of shower particles (of energy E) which scatter into unit solid angle at an angle θ be $N(E,\theta)$.

Assuming that all such angles are small, we may normalize

$$\int_0^\infty N(E,\theta)\, 2\pi\theta\, d\theta = 1 . \qquad (5.31)$$

Let the fraction of shower particles in the energy range (E,E+dE) be f(E)dE. Referring to equation (3.24) and noting that the threshold velocity for Cerenkov radiation is given by

$$\beta_T = \frac{1}{n} , \qquad (5.32)$$

we may write the Cerenkov yield per particle per meter as proportional to

$$1 - \left(\frac{E_T}{E}\right)^2 .$$

Then the number of Cerenkov photons emitted into unit solid angle per shower particle is

$$F_c(\theta)d\Omega = Y_c \int_{E_T}^\infty \left[1 - \left(\frac{E_T}{E}\right)^2\right] N(E,\theta) f(E) dE \ \frac{\text{photons}}{\text{ster. meter}} , \qquad (5.33)$$

where Y_c is the total Cerenkov yield per particle per meter in the wavelength region 3400 Å to 4500 Å for $\beta = 1$.

Correspondingly, the number of scintillation photons in the same wavelength range emitted into unit solid angle per shower particle per meter is

$$F_s d\Omega = \frac{1}{4\pi} Y_s \quad \frac{\text{photons}}{\text{ster. meter}} . \qquad (5.34)$$

At about 5 kilometers altitude, $Y_c \approx 5$ photons/meter and

$$Y_s \approx 3 \text{ photons/meter} , \qquad (5.35)$$

and therefore the ratio of the Cerenkov flux to the scintillation flux is simply

$$\frac{F_c}{F_s} = \frac{5}{3} \times 4\pi \int_{E_T}^{\infty} \left[1 - \left(\frac{E_T}{E}\right)^2\right] N(E,\theta) f(E)\, dE \quad . \qquad (5.36)$$

The distributions $N(E,\theta)$ and $f(E)$ may be found in reference 79. Numerical integration of the quantity (5.36), using $E_T = 30$ Mev for 5 kilometers, then shows that

$$F_c > F_s \qquad \text{for } \theta < 23^\circ \ . \qquad (5.37)$$

In other words, because of the multiple scattering, the Cerenkov radiation dominates over the fluoresence radiation for $\theta < 23^\circ$, which corresponds to a time

$$(\Delta t)_{Cer} = 0.20 \ R/c \qquad (5.38)$$

in the frame of reference of an observer, independent of ψ and β . Since the full width of the observed fluorescence pulse, from (5.19), is

$$(\Delta t)_{Fluor} = \frac{R}{c} \cot \frac{\psi}{2} \qquad (5.39)$$

this implies that the Cerenkov emission dominates the entire pulse for showers having $\psi > 157^\circ$, which of course are the strongly approaching showers; and in general the Cerenkov emission dominates for a fraction 0.20 tan $\frac{\psi}{2}$ of the duration of the pulse.

The Cerenkov contribution actually aids in the determination of the shower parameters, if the time resolution of the detector allows it, since at every instant the signal amplitude is enhanced without affecting the values of ϕ, $\frac{d\phi}{dt}$, and $\frac{d^2\phi}{dt^2}$. However, the determination of the shower curve $N(E_o,t)$, and hence the energy E_o, requires knowing the relative contributions of the two radiation mechanisms at each

measurement, since we now have a linear combination

$$N(E_o,t) = aF(z,t) + bF_c(z,t) \quad . \tag{5.40}$$

The time dependence of the Cerenkov signal may be derived by assuming a form for the function $N(E,\theta)$. For example, if we approximate

$$N(E,\theta) \propto \frac{1}{\theta(\theta + \theta_o)^3} \quad , \tag{5.41}$$

independent of E, we find close agreement with the cascade theory function with $\theta_o = 14^o$. Then, modifying equation (2.92), the time variation of the Cerenkov signal is

$$F_c(z,t) \propto \frac{N(E_o,t)}{Rt(\theta_o + \frac{2ct}{R})^3} \exp\left[-\frac{kR^2}{2ct}\left(1 + \frac{c^2t^2}{R^2}\right)\right], \tag{5.42}$$

where the exponential factor is included to account for atmospheric absorption. The Cerenkov signal falls off as $1/t$ for $t \ll R\theta_o/2c$ but then falls off as $1/t^4$, much more rapidly than the fluorescence signal, for $t \gg R\theta_o/2c$.

Capabilities of this Experiment -

To summarize the efficiency of this detection system for air showers of various energies and at various distances, we refer back to equations (3.18) to (3.23), which derive the readability of an event as a function of shower size N and impact parameter R.

$$Q = \frac{1 + \cos\theta}{4\pi R^{3/2}} e^{-kR} \Lambda_s Y(\lambda_o) \sqrt{\frac{A\, s(\lambda_o)}{c\Lambda_b B(\lambda_o)\Delta\omega}} \quad . \tag{5.43}$$

This expression of course is only approximate, as it ignores

(a) the variation of the readability with angle ψ (Figure 5.1), (b) the variation of the shower development with zenith angle ζ, and (c) the contribution of Cerenkov light. However, with these reservations in mind, we may apply (5.43) to find the approximate average counting rate for events of a given minimum Q-value.

Filling in the parameters for the 5-tube detector, we have

A = phototube area = $0.1\ m^2$

Δt = amplifier resolving time = 1.5×10^{-6} sec.

$\Delta\omega$ = 3 steradians

$s(\lambda_o)$ = 0.10 photoelectrons/incident photon

$Y(\lambda_o)\Lambda_s$ = 3 photons/meter-particle

$B(\lambda_o)\Lambda_b$ = 1.45×10^{11} photons/m^2 sec ster

Then a shower of N particles with impact parameter R meters produces a maximum signal of

$$\frac{0.43\ N\ e^{-kR}}{R^2} \text{ photoelectrons in 1.5 microseconds.} \qquad (5.44)$$

The background from the night sky in this time is 4000 photoelectrons, which corresponds to a noise level of 60 photoelectrons in 1.5 microseconds. Therefore the peak signal-to-noise ratio is

$$S/N = 7.2 \times 10^{-3}\ \frac{N}{R^2}\ e^{-kR}\ . \qquad (5.45)$$

The number of possible independent signal measurements is on the order of 2.2×10^{-3} R, which leaves

$$Q \approx 3.5 \times 10^{-4}\ \frac{N e^{-kR}}{R^{3/2}} \qquad (5.46)$$

with R in meters.

Let dI(N) be the rate of air showers in the size range (N,N+dN). Letting N represent the number of secondaries at maximum, we know approximately (24)

$$dI(N) \approx 80 \frac{dN}{N^{2.6}} \quad \text{events/m}^2 \text{ sec ster} \qquad (5.47)$$

or

$$\frac{dI(N)}{d(\ln N)} = \frac{N\, dI(N)}{dN} \approx \frac{80}{N^{1.6}} \quad \text{events/m}^2 \text{ sec ster .} \qquad (5.48)$$

Then the rate of showers of size greater than N is given by

$$I(> N) \approx \frac{50}{N^{1.6}} \quad \text{events/m}^2 \text{ sec ster .} \qquad (5.49)$$

Now assume that Q = 0 unless the pulse width is larger than 4.5 microseconds, a value set by the requirement that at least 3 independent pulse amplitude measurements be made for a recorded pulse to be considered as a potential air shower event. Although the total pulse duration is

$$\Delta t = \frac{R}{c} \cot \frac{\psi}{2} \quad , \qquad (5.50)$$

in practice, for receding events, the time dilation of the receding part of the event reduces the signal amplitude so much that the readable pulse duration is on the average only $\Delta t = R/c$. We therefore must conclude that no events are measurable for $R < c(\Delta t)_{min} = 1.35$ kilometers.

Therefore the number of events expected with $Q > Q_o$ and having a shower size N in the logarithmic range $d(\ln N) = dN/N$ is

$$I(Q > Q_o) = \frac{80\ d(\ln N)}{N^{1.6}} \int_{R_{min}}^{R(N,Q_o)} 2\pi R\ dR \qquad (5.51)$$

$$= \frac{80\pi\ d(\ln N)}{N^{1.6}} \left[R(N,Q_o)^2 - R_{min}^2 \right] \frac{\text{events}}{\text{ster. sec}} \qquad (5.52)$$

where $R(N,Q_o)$ is the solution of equation (5.46) in meters, and is

$$R(N,Q_o) = 5.0\times10^{-3} \left(\frac{N}{Q_o}\right)^{2/3} \text{ meters} \qquad (5.53)$$

in the absence of atmospheric absorption.

The function (5.52) has been evaluated numerically using an atmospheric absorption coefficient $k = 0.1\ km^{-1}$, corresponding to very clear visibility, and a minimum Q-value of $Q_o = 25$. The distribution is shown in Figure 5.6. The detector is most efficient for seeing air showers of about 10^{10} particles, or an energy of 2×10^{19} ev. Above $N = 4\times10^{10}$ the cosmic ray spectrum may undergo a cut-off, in which case this distribution of course over-estimates the counting rate.

We can also derive the distribution of readable events as a function of distance of closest approach R. Combining equations (5.46) and (5.49), the number of events having $Q > Q_o$ which fall in the range (R,R+dR) is given by

$$I(Q > Q_o) \approx \frac{50}{N_o^{1.6}}\ 2\pi R\ dR, \quad R > R_{min} \qquad (5.54)$$

$$= 3.3\times10^{-10}\ \frac{e^{-1.6kR}dR}{R^{1.4}} \quad \text{for } Q_o = 25\ , \qquad (5.55)$$

where this time R is in units of kilometers. This distribution is illustrated in Figure 5.7, again using $k = 0.1\ km^{-1}$. Both

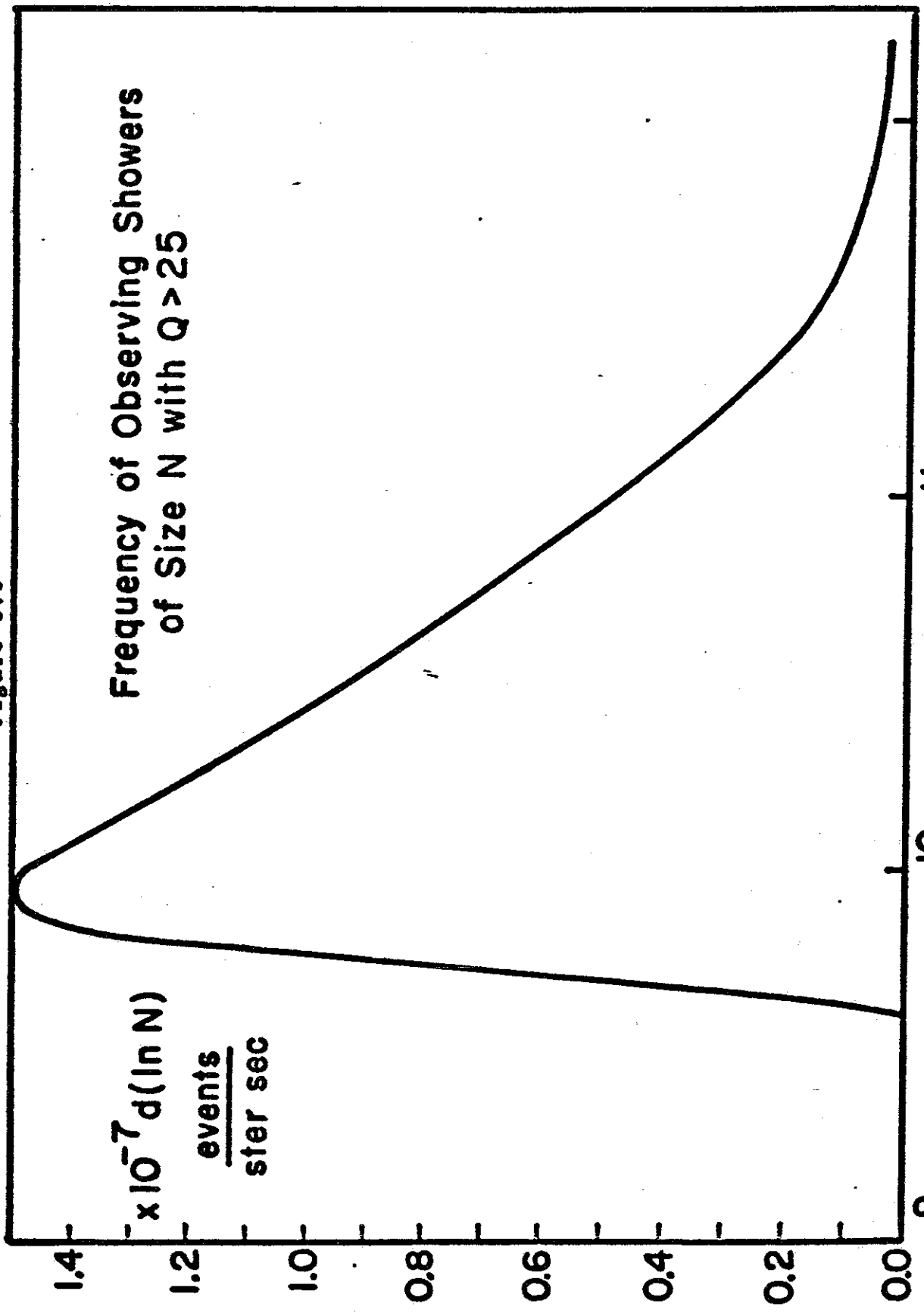
Frequency of Observing Showers
of Size N with Q>25
$\times 10^{-7} d(\ln N)$
events / ster sec
1.4
1.2
1.0
0.8
0.6
0.4
0.2
0.0
10^9
10^{10}
10^{11}
10^{12}
Shower Size, N

Figure 5.6

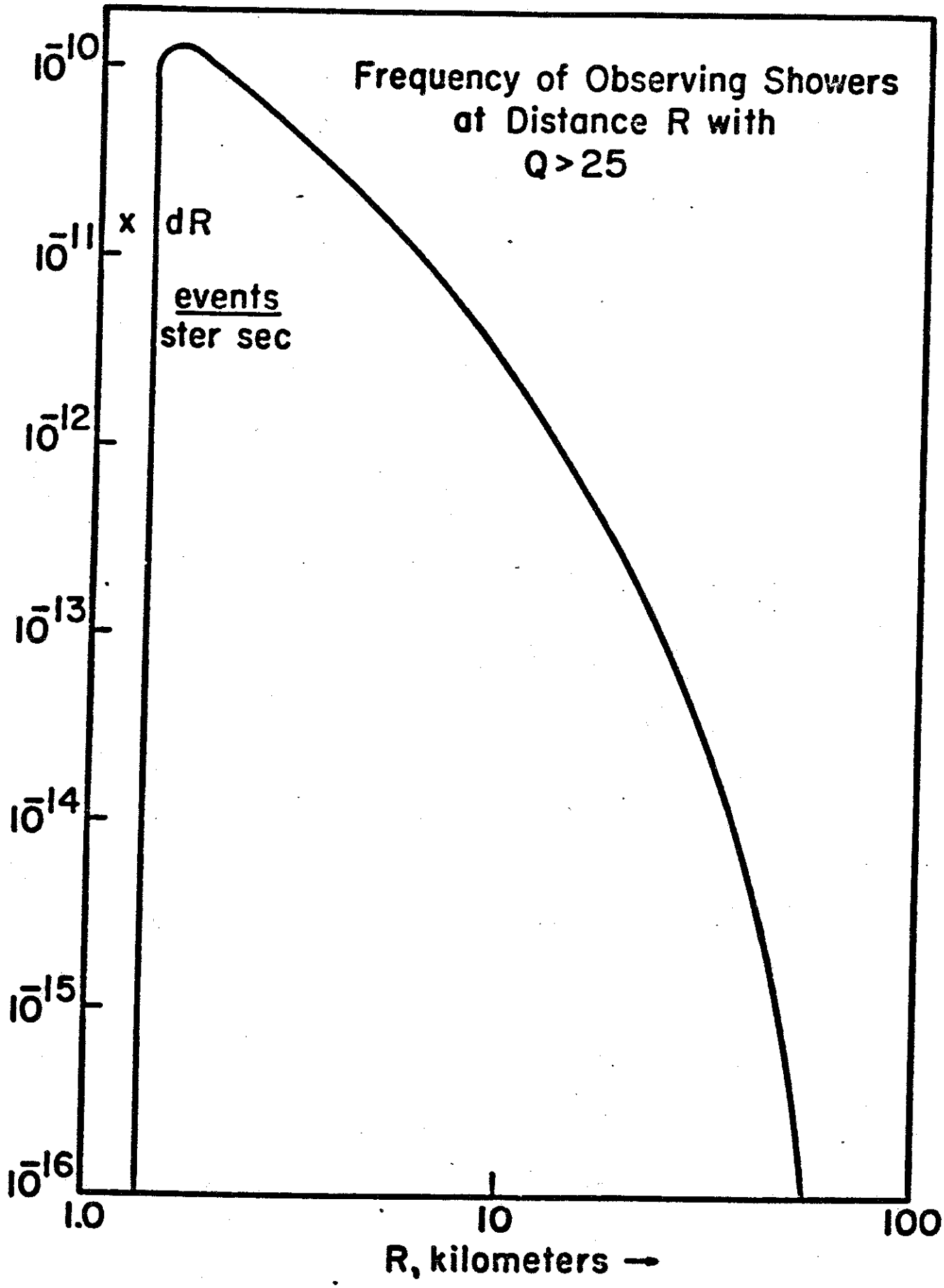
Frequency of Observing Showers
at Distance R with
Q>25
10^{-10}
10^{-11}
10^{-12}
10^{-13}
10^{-14}
10^{-15}
10^{-16}
x dR
events
ster sec
1.0
10
100
R, kilometers →

Figure 5.7

atmospheric absorption and the inverse square law combine to prevent the detection of many measurable events from beyond 10 kilometers.

The total predicted counting rate is given by the integral of equation (5.55) over all R, and is

$$I(Q > Q_o) = 3.3\times10^{-10} \left(\frac{25}{Q_o}\right)^{1.6} \int_{R_{min}}^{\infty} R^{-1.4} e^{-1.6kR} dR \qquad (5.56)$$

$$\approx 3\times10^{-7} \left(\frac{25}{Q_o}\right)^{1.6} \text{ events/ster. sec .} \qquad (5.57)$$

Taking the effective solid angle of the detector to be 4 steradians,

$$I(Q > Q_o) \approx 1.2\times10^{-6} \left(\frac{25}{Q_o}\right)^{1.6} \text{ events/sec}$$

$$= 4.3\times10^{-3} \left(\frac{25}{Q_o}\right)^{1.6} \text{ events/hour .} \qquad (5.58)$$

This result is shown in Figure 5.8. For $Q \geq 30$, which represents events that could be analyzed with some accuracy, we may expect approximately one event every 300 hours of good running time. The expected frequency of coincidences between two stations situated 10 kilometers apart is of course much lower. However, any event that is viewed by two stations, provided a coincidence is substantiated, for example by means of a signal between stations, then provides many times as much information and thus may be considered as an event of much higher Q than that indicated by an individual station.

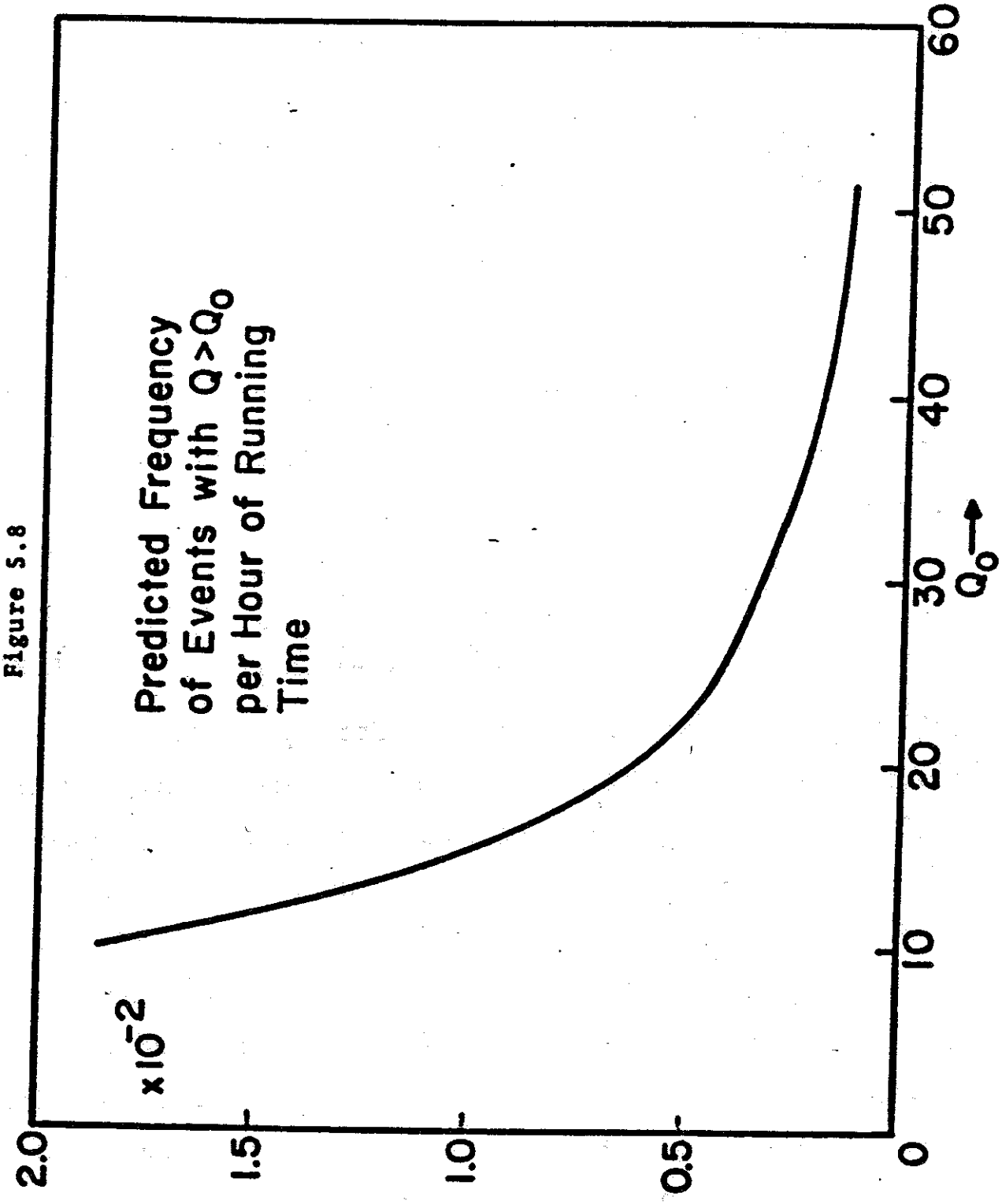
Predicted Frequency
of Events with Q>Q₀
per Hour of Running
Time
x10⁻²
2.0
1.5
1.0
0.5
0
10
20
30
40
50
60
Q₀

Figure 5.8

Chapter 6

RESULTS AND CONCLUSIONS

Three practically identical experimental stations of the type described in Chapter 4 were constructed and put into operation in the interval 1964-1966. These stations recorded data for a combined total effective running time of 1000 hours. This number represents the sum of the number of hours each night during which the equipment in any one 5-tube station was operating correctly, multiplied by a factor indicating the fraction of the sky that was obscured by clouds or haze. The actual time that the equipment was turned on totals approximately 2000 hours.

The 1000 hours corresponds to an effective duty cycle factor of 3.9%. This low percentage is the result of several causes, listed below in order of decreasing importance:

(a) Sunlight and twilight

(b) Moonlight and moon twilight

(c) Haze, clouds and rain

(d) Atmospheric electrical storms

(e) Proper functioning of equipment.

With the exception of the rising and setting times of the moon, which advance from 20 to 90 minutes per day, the stations were automatic in turning on and off and in recording data. Consequently the equipment was frequently operating in cloudy or even stormy weather when no possibility of recording a true cosmic ray event existed. Pictures taken during rain,

fog or snow conditions were frequently rejected *a priori* from the scanning procedure.

A grand total of 110,000 pictures were recorded during this experiment. Approximately 10,000 pictures occurred at times of instrumental failure and another 10,000 during extreme weather conditions such as lightning storms. The remaining 90,000 pictures were scanned carefully for sets of pulses bearing at least some of the following characteristics:

1. An easily distinguished pulse in at least one channel,
2. Some semblance of pulses in at least one other channel,
3. The pulse height in the UP channel should be roughly as large as that in other channels,
4. Pulses should be single--that is, no long absence of signal between sizeable pulses in a single channel is desired,
5. Some difference in the time scale of pulses in different channels,
6. Some differences in the amplitudes of pulses among the 5 channels,
7. Pulse duration at least 3 microseconds,
8. No sizeable pulse in the Control ("Spare") channel,
9. No rapid series of cathode ray sweeps close together, indicating a lengthy rise in light level, such as is produced by lightning events,
10. No linearly rising pulse which continues longer than the cathode ray sweep, (also typical of lightning flashes).

The initial film scanning for all three stations produced a total of 263 pictures with some recognizable pulses occurring at times when the apparatus was apparently operating normally. These events were re-scanned with the above criteria in mind, and after rejecting 139, mainly for failure to meet criteria 4, 7, 8 or 9, the reamining 124 events were judged to have some remote possibility of having resulted from cosmic ray showers. An example of one of these events is sketched in Figure 6.1. A further 96 pictures were rejected on the bases of criteria 2, 3, 4 and 7, leaving 28 events which strongly suggested the presence of air showers but lacked sufficient signal-to-noise ratios and/or durations for reasonable analysis. Analysis was indeed attempted on several of these events with no success in even establishing a shower plane.

Only 10 events from this last selection were of a quality high enough to warrant careful analysis. A photograph of one of these events is inserted on page 192. These pictures were studied carefully, and most were subjected to analysis either by the maximum likelihood computer program developed by E. Jenkins and mentioned in Chapter 5, or by a graphical technique devised by G. Tanahashi equivalent to the description following equation (5.1) of this thesis. All of these 10 events failed to satisfy the requirement that the apparent source of light move in some general direction in the sky to yield a self-consistent determination of the orientation of the shower-detector plane, and none of these events yielded credible information on the other shower parameters.

Sketch of One Event as Recorded on Film

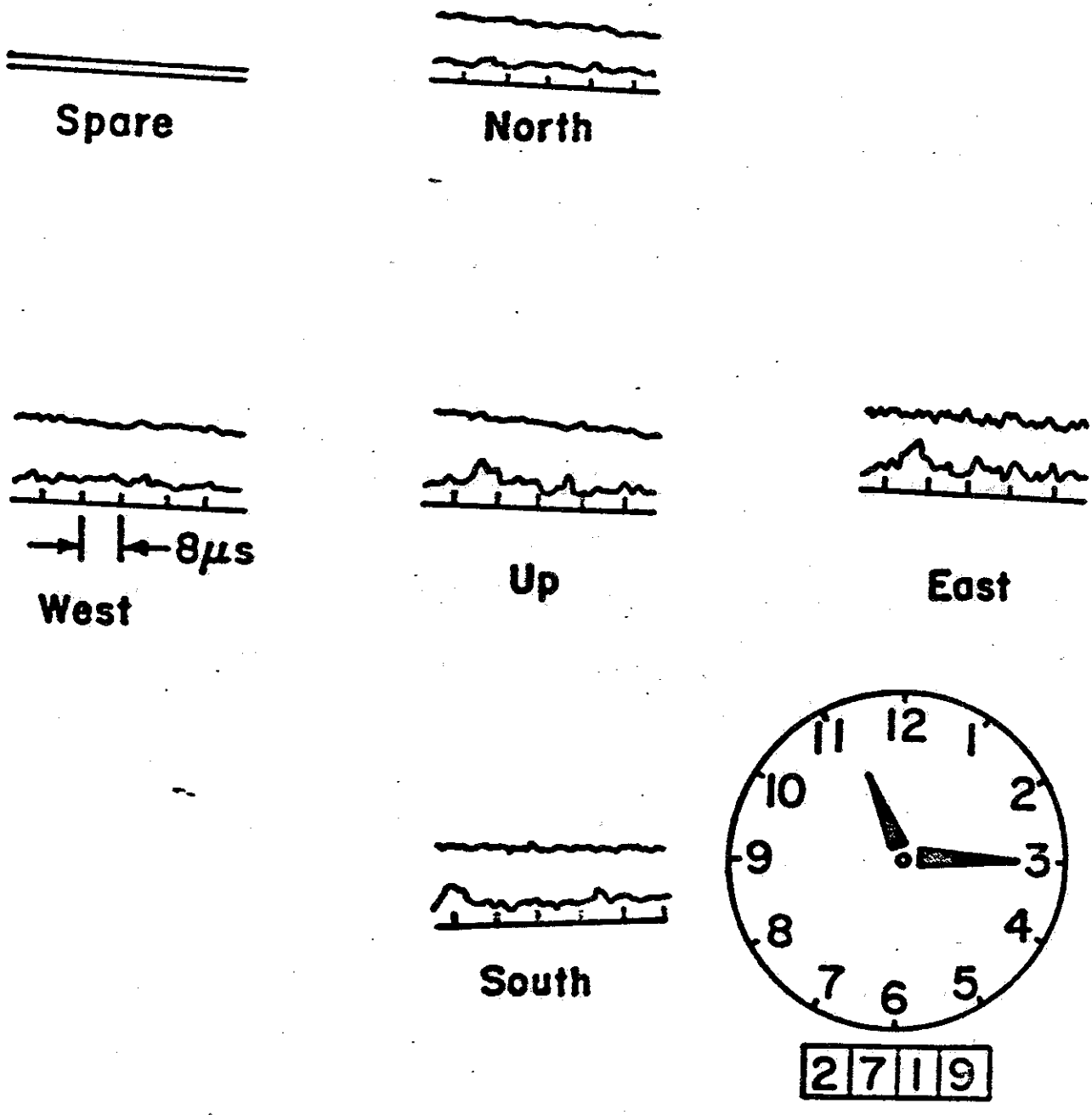

Figure 6.1

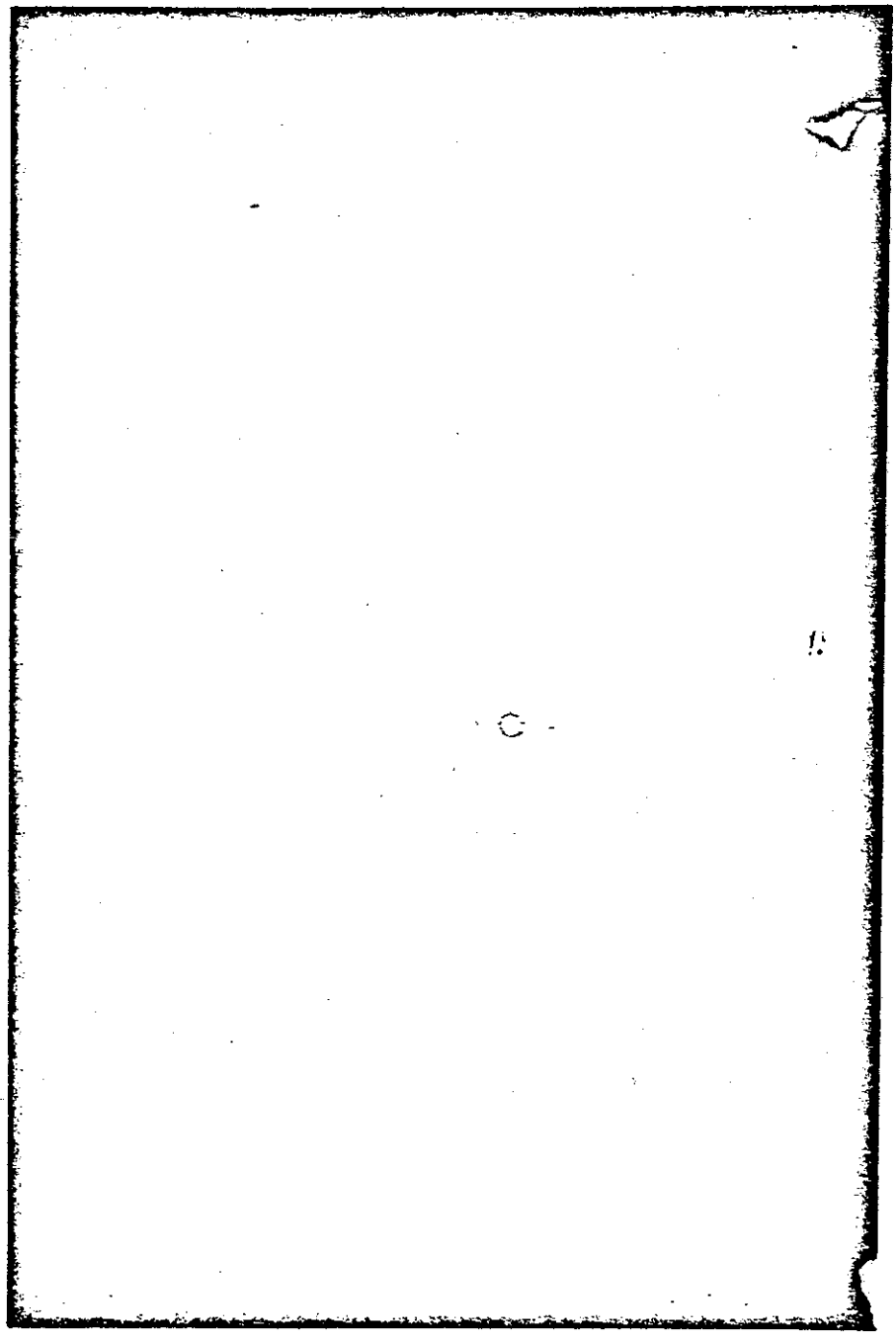

Figure 6.2 Oscilloscope Display of One Event

None of the events recorded in the 1000 hours have a quality $Q > 30$. This may be compared with Figure 5.8, which indicates that about 3 such events were expected. We feel that it is unlikely that our procedure of estimating the expected counting rate results in an error of more than a factor of 3. The most serious sources of error are (1) the inclusion in the running time of periods when the atmospheric transparency was substantially reduced, and (2) possible errors in the prior information on the frequency of very high energy primaries. As Figure 5.6 shows, the best recorded events should be representative of shower sizes greater than 10^{10} particles, where the primary spectrum is not yet well-established. Although this experiment so far does not have the sensitivity to challenge the estimated primary spectrum in this region (24,97), we at least believe that the true flux can be no greater than that shown in Figure 1.1.

We may note that if the 10 marginal events selected above are assumed to have been due to air showers, this number in 1000 hours would correspond well to Figure 5.8 for $Q_o = 15$.

Narrow Pulses -

We have mentioned in Chapter 4 that pulses of sizable amplitude and unresolvable width were frequently recorded by this apparatus. Attempts to determine the source of these pulses were not wholly successful, but it appears likely that at least some of them originated from radiation in the

atmosphere. Evidence in favor of this point was provided by operating two independent detector stations at a separation of 50 meters for about 30 hours, during which time many coincidences of very narrow pulses were recorded. No coincidences were otherwise seen. Although the frequency of these fast pulses was not measured carefully, and in fact the coincidence logic discriminated against them, they occurred roughly once per 8 hours of running time. This rate is not unreasonable for that expected from air showers. The majority of optical pulses satisfying a given minimum signal-to-noise ratio independent of duration, are those due to the many low energy showers which occur near the detector. Moreover, the maximum amplitude for the pulse of Cerenkov light from nearby air showers, from equation (5.37), is always greater than the fluorescence pulse amplitude. Hence the frequently recorded narrow pulses may well reflect the Cerenkov signals from air showers having energies on the order of 10^{17} ev or less.

Future Plans -

Several reasons exist for the low sensitivity of the wide angle detector described here. Chief among these is the fact that background light is collected by each photomultiplier from a wide solid angle--about 4 steradians. Also, the sensitivity of each photomultiplier drops off rapidly with increasing angle of incidence. Thirdly, the dependence on

relative pulse amplitudes for the determination of the light source position demands accurate calibrations and large signal-to-noise ratios to avoid error.

It is clear that this sensitivity must be greatly increased to take advantage of the special properties of the fluorescence radiation for the detection of high energy air showers at large distances. A design which greatly alleviates the above limitations is currently being developed by the Cornell University Cosmic Ray Group and is described below.

The sky is to be divided into 500 sectors, each of solid angle 0.01 steradian, by a network of 500 two-inch photomultipliers placed in the focal surfaces of 0.1 meter^2 Fresnel lenses. Optical filters will reduce the night sky background to a negligible level as well as eliminating the light from filament lamps visible near the horizon. A cross section of one lens unit is shown in Figure 6.3. Triggering will be accomplished by seeking a delayed coincidence between any two adjacent channels. The pulses are then to be displayed on a large bank of 3-inch cathode ray tubes and photographed on 70-mm film.

The improvement in signal-to-noise ratio by this design over the five-channel system is impressive: The background light is reduced by a factor of $4/.01 = 400$. The two-inch phototubes have cathode efficiencies typically 70% higher than the 15-inch tubes. The effective area remains the same ($0.1\ m^2$) while all angles of incidence are reduced to near zero. The determination of the shower-detector plane follows

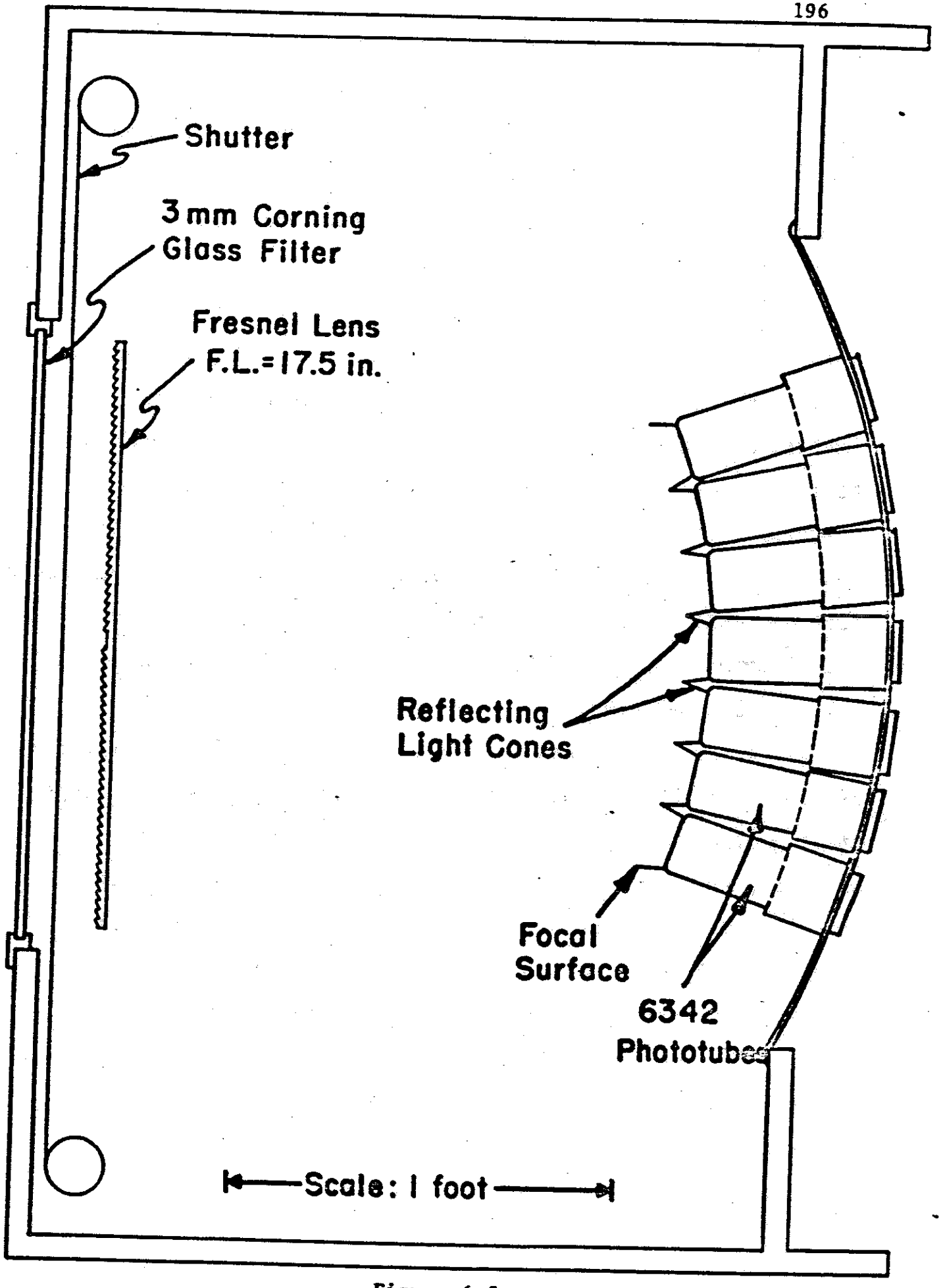
Shutter
3 mm Corning
Glass Filter
Fresnel Lens
F.L.=17.5 in.
Reflecting
Light Cones
Focal
Surface
6342
Phototube
Scale: 1 foot

Figure 6.3

from the identification of the channels bearing pulses, with no amplitude measurements necessary. Even $\phi(t)$ and its derivatives are found without reference to pulse amplitudes and hence without reference to photomultiplier and amplifier calibrations. (These latter are of course necessary for reconstruction of the shower curve.)

The net improvement in signal-to-noise ratio in each channel, from equation (3.21), is a factor of 50 (with only a factor of 4 increase in cost). Moreover, events may be analyzable with signal-to-noise ratios a factor of 2 lower than for the five-channel detector, so that the frequency of analyzable events may be expected to rise by a factor of 1000. Again, viewing an event simultaneously with two or more detector stations will fix the position of the shower axis with a minimum of error, but this will only be possible for a fraction of all the recorded events.

It is hoped ultimately to combine the long-distance vision of the fluorescence technique with the dependability of a large-scale ground-based particle sampling technique in the same location, to provide detailed information on the source direction and shower structure of every very high energy primary particle falling in the vicinity. Indeed, these two techniques for air shower study are complementary in several ways: for example, the ratio of the fluorescence yield to the muon density at sea level may indicate the charge of the primary cosmic ray. It is clear that such an amalgamation will

contribute much more information concerning the highest energy cosmic rays than either technique alone. The locale in which it is anticipated that these experiments will be joined is a large area in the Pilliga state forest in Australia, near the location of the Siding Springs Observatory and the Brown-Twiss intensity interferometer. Extensive information on climate and observing conditions in that vicinity indicates promise that another important gain will be a factor of 3 or 4 in useful observing time.

REFERENCES

1. B. Rossi, High Energy Particles, (1952)
2. K. Greisen, Cosmic Ray Showers, Ann. Rev. Nuc. Sci. 10 (1960)
3. Ginzburg and Syrovatskii, The Origin of Cosmic Rays (1964)
4. A.E. Sandstrom, Cosmic Ray Physics (1965)
5. P. Morrison, The Origin of Cosmic Rays, Handbuch der Physik 46, (1961)
6. Proc. Int. Conf. on Cosmic Rays and Earth Storms, III, Kyoto (1961)
7. Proc. Fifth Interamerican Sem. on Cosmic Rays, II, Bolivia (1962)
8. Proc. Int. Conf. on Cosmic Rays, III and IV, India, (1963)
9. Proc. Ninth Int. Conf. on Cosmic Rays, London (1965)
10. C.W. Allen, Astrophysical Quantities (1964)
11. P. Morrison, Rev. Mod. Phys. 29, 235 (1957)
12. G.T.Zatsepin et al, Int. Conf. on Cosmic Rays, India (1963)
13. J. Linsley, Phys. Rev. Letters 9, 123, 126 (1962)
14. Rosenthal, Goryunov et al, Proc. Int. Conf. on Cosmic Rays, Kyoto (1961)
15. F.B. McDonald, unpublished
16. B. Peters, Nuovo Cimento, 22, 800 (1961)
17. J. Linsley, Phys. Rev. Letters, 10, 146, (1963)
18. S. Hayakawa, Proc. Int. Conf. on Cosmic Rays, III, Kyoto, (1961) Page 181
19. S.A. Korff, Proc. Fifth Inter. Seminar on Cosmic Rays, II Bolivia (1962) p. LI-1
20. S. Colgate, Proc. Ninth Int. Conf. on Cosmic Rays, London (1965)
21. Hasegawa and Ito, Proc. Int. Conf. on Cosmic Rays, III, Kyoto (1961) p. 53

22. E. Fermi, Ap. J. 119, 1 (1954)

23. S.I. Syrovatskii, JETP 13, 1257 (1961)

24. K. Greisen, Proc. Ninth Int. Conf. on Cosmic Rays, London (1965) p. 609

25. G.T. Zatsepin, Dokl. Akad. SSSR, 80, 577 (1951)

26. J.B.Birks, The Theory And Practice of Scintillation Counting (1964)

27. J.V. Jelley, Cerenkov Radiation and Its Applications (1959)

28. B. Rossi and K. Greisen, Cosmic Ray Theory, Rev. Mod. Phys. 13, 240 (1941)

29. D.M. Ritson, Techniques of High Energy Physics (1961)

30. A. Bunner, The Atmosphere as a Cosmic Ray Scintillator, Thesis, Cornell University (1964)

31. P. Hartman, Luminescence Efficiency of Air on Electron Bombardment, Los Alamos report (1963)

32. G. Davidson and R. O'Neil, J. Chem. Phys. 41, 3946 (1964)

33. A.E. Grun, Can. Jour. Phys. 36, 858 (1958)

34. G. Herzberg, Molecular Spectra and Molecular Structure: Diatomic Molecules (1950) vol 1

35. Pearse and Gaydon, The Identification of-Molecular Spectra (1962)

36. R.W. Nicholls, E.M. Reeves, D.A. Bromley, Proc. Phys. Soc. 74, 87 (1959)

37. R.H. Hughes, J.L. Philpot, C.Y. Fan,Phys. Rev. 123, 2084 (1961)

38. Massey and Burhop, Electronic and Ionic Impact Phenomena, (1952)

39. D.T. Stewart and E. Gabathuler, Proc. Phys. Soc. 72, 287 (1958)

40. C.Y. Fan, Phys. Rev. 103, 1740 (1956)

41. K. Schmidt, Z. Naturforsch. 11a, 1023 (1956)

42. R.W. Nicholls and D. Pleiter, Nature 178, 1456, (1956)

43. Hughes, Philpot, Dodd, Lin, University of Arkansas report, Sept. (1962)

44. F. Sears, Thermodynamics and Kinetic Theory (1956)

45. A.E. Grun and E. Schopper, Z. Naturforsch. 9a, 134 (1954)

46. Keck, Camm, Kivel, Wentink, Ann. Physics 7, 1 (1960)

47. Lunt, Corrigan et al, in Atomic Collision Processes (1964)

48. H. Hoerlin, private communication

49. Evans, The Atomic Nucleus,(1955)

50. B. Brocklehurst, Trans. Faraday Soc. 60, 2151 (1964)

51. R.W. Nicholls, J. Atmos. Terr. Physics, 25, 218 (1963)

52. D.R. Bates, Proc. Roy. Soc. A196, 217 (1949)

53. J.B. Hasted, Physics of Atomic Collisions, (1964)

54. W.F. Sheridan, O. Oldenberg, N.P. Carleton, Second Conf. on Physics of Electronic and Atomic Collisions (1961)

55. J.W. McConkey and I.D. Latimer, Proc. Phys.Soc. 86, 463 (1965)

56. H.D. Smyth and E.G.F. Arnott, Phys. Rev. 36, 1023 (1930)

57. D.C. Tyte, Proc. Phys. Soc. 80, 1347 (1962)

58. C.Y. Fan and A.B. Meinel, Ap. J. 118, 205 (1953)

59. E.M. Reeves, R.W. Nicholls, D.A. Bromley, Proc. Phys. Soc. 76, 217 (1960)

60. P.L. Hartman and H. Hoerlin, Bull. Am. Phys. Soc. 7, 69 (1962)

61. Frankenthal, Manley, Treve, J. Chem. Phys. 44, 257 (1966)

62. D.R. Westevelt, Los Alamos Report (1963)

63. R.G. Bennett and F.W. Dalby, J. Chem. Phys. 31, 434 (1959)

64. L.O. Brown and N. Miller, Trans. Faraday Soc. 53, 748 (1957)

65. A.E.S. Green and C.A. Barth, J. Geophys. Research 70, 1083 (1965)

67. A. Dalgarno, I.D. Latimer, J.W. McConkey, Planet. Space Science 13, 1008 (1965)

66. A. Dalgarno, Annales de Geophysique, 20, 65 (1965)

68. M. Jeunehomme and A.B.F. Duncan, J. Chem. Phys. 41, 1692 (1964)

69. W. Lichten, J. Chem. Phys. 26, 306 (1957)

70. W.F. Sheridan, O. Oldenberg, N.P. Carleton, Atomic Collision Processes (1964) p. 440

71. J. Janin, Annales de Physique 12, 1, p. 538 (1946)

72. J.W. Chamberlain, Physics of the Aurora and Airglow (1961)

73. Fehsenfeld, Schmeltekopf, Ferguson, Planet. Space Science 13, 919 (1965)

74. L. Koch, L'Electronique Nucleaire (1958)

75. C. Eggler and C.M. Huddleston, Nucleonics 14, 34 (1956)

76. W.A. Baum and L. Dunkelman, J. Opt. Soc. America 45, 166, (1955)

77. H. Hoerlin, Los Alamos Report LA-3417-MS (1965)

78. A.E.S. Green and P.J. Wyatt, Atomic and Space Physics (1965)

79. K. Greisen, in Prog. in Cosmic Ray Physics III (1956)

80. J. Sharpe, Photoelectric Cells and Photomultipliers, EMI (1961)

81. J.L. Lawson and G.E. Uhlenbeck, Threshold Signals (1950)

82. H. Anton, Ann. der Physik 7, 17 (1965)

83. H. Anton, Ann. der Physik, in press, (1966)

84. M. Jeunehomme, J. Chem. Phys. 44, 2672 (1966)

85. W. Galbraith and J.V. Jelley, J. Atmos. Terr. Phys. 6, 250, 304 (1955)

86. A.E. Chudakov and N.M. Nesterova, Proc. Fifth Seminar on Cosmic Rays, Bolivia (1962)

87. H. Kasha and Y. Ören, Proc. Fifth Seminar on Cosmic Rays Bolivia (1962)

88. D.A. Hill et al, Proc. Fifth Seminar on Cosmic Rays, Bolivia (1962)

89. F.A. Jenkins and H.E. White, Fundamentals of Optics 1957

90. E.B. Jenkins, The Interpretation of Atmospheric Fluorescence Signals from Multijoule Cosmic Ray Air Showers Thesis, Cornell University (1966)

91. D. Ophir and U. Galil, Electronics 34, No. 28, 68 (1961)

92. E. Fink and K.H. Welge, Z. Naturforsch. 19A, 1193 (1964)

93. W. Wegler, Zeit. fur Physik 173, 169 (1963)

94. A.G. Gaydon, Proc. Phys. Soc. 56, 85 (1944)

95. P.K. Carroll and N.D. Sayers, Proc. Phys. Soc. A66, 1138 (1953)

96. G. Clark et al. Proc Int. Conf. on Cosmic Rays, Jaipur (1963)

97. H. Bradt et al. Proc. Int. Conf. on Cosmic Rays, London (1965)

98. P.L. Jain et al. Phys. Rev. 115, 654 (1959)

99. M.F. Kaplon and D.M. Ritson, Phys. Rev. 88, 386 (1952)

100. Y. Toyoda et al. Proc. Int. Conf. on Cosmic Rays, London (1965)

101. W.N. Hess, Introduction to Space Sciences (1965)

102. A.A. Penzias and R.W. Wilson, Ap. J. 142, 419 (1965)

103. K. Greisen, Phys. Rev. Letters 16, 748 (1966)

104. J.V. Jelley, Phys. Rev. Letters 16, 479 (1966)

105. R.J. Gould and G. Schreder, Phys. Rev. Letters 16, 252 (1966)

106. B. Rossi and K. Greisen, Rev. Mod. Phys. 13, 240 (1941)

107. W. Galbraith, Extensive Air Showers (1958)

108. B. Peters, Proc. Int. Conf. on Cosmic Rays, Moscow, (1960)